Università Ca'Foscari Venezia

The University of Sydney

Ca' Foscari University of Venice, Italy

The University of Sydney, Australia

Doctoral Thesis

Unconventional Liquid Crystal Phases of Helical Particles

Author:
Hima Bindu Kolli

Supervisors:
Prof. Achille Giacometti
Dr. Toby Hudson

A thesis submitted in fulfilment of the requirements for the degree of Doctor of Philosophy

in

Department of Molecular and Nano Systems, Ca' Foscari University of Venice, Italy

and

School of Chemistry, The University of Sydney, Australia

December 2014

Declaration of Authorship

I, Hima Bindu Kolli, declare that this thesis titled, 'Unconventional Liquid crystal Phases of Helical Particles' and the work presented in it are my own. I confirm that:

- This work was done wholly or mainly while in candidature for a research degree at Ca' Foscari University of Venice and The University of Sydney.
- Where any part of this thesis has previously been submitted for a degree or any other qualification at this University or any other institution, this has been clearly stated.
- Where I have consulted the published work of others, this is always clearly attributed.
- Where I have quoted from the work of others, the source is always given. With the exception of such quotations, this thesis is entirely my own work.
- I have acknowledged all main sources of help.
- Where the thesis is based on work done by myself jointly with others, I have made clear exactly what was done by others and what I have contributed myself.

Signed: _____

Date: _____

Abstract

Helical particles are ubiquitous in nature. Many natural and synthetic biomolecules like polynucleotides and polypeptides; colloidal suspensions like filamentous (fd) virus and helical flagella and certain organic molecules are found in helical shape. Despite their abundance in nature, understanding of the phase behaviour of helical particles is poor. These helical molecules have a well known propensity to form liquid crystal phases. The chirality in the helical shapes influence their liquid crystal organization. Experimental results of the liquid crystal phases shown by these molecules are often compared to those of rods, neglecting the effect of helical shape on phase behaviour. We have undertaken an extensive investigation of the phase diagram of hard helical particles using Monte Carlo simulations. We provide evidence of new chiral phases exhibiting screw-like order. This new chiral phase is different to the cholesteric phase and is characterized by the C_2 symmetry axes of helices spiralling around the nematic director with periodicity equal to the particle pitch. We have used Isobaric Monte Carlo simulations to obtain a full phase diagram of helical particles. A rich polymorphism is observed exhibiting a special screw-like nematic and a number of screw-like smectic phases. The effect of helical shape on the phase diagram is studied by considering different shapes of helix obtained by tuning the helical parameters like radius and pitch. We found a remarkable change in the phase behaviour with the change in the shape of helix. Dense packing structures of different helical shapes are found by implementing Isopointal set Structural Search Method (ISSM). The physical mechanism underlying the liquid crystal order observed in helical flagella is explained.

List of publications

- The isotropic to nematic phase transition in hard helices: Theory and simulation
  Elisa Frezza, Alberta Ferrarini, **Hima Bindu Kolli**, Achille Giacometti, Giogio Cinacchi
  J. Chem. Phys. 138 (16), 164906 (2013) [*Chapter 3*]

- Communication: From rods to helices: Evidence of a screw like nematic phase
  Hima Bindu Kolli, Elisa Frezza, Giorgio Cinacchi, Alberta Ferrarini, Achille Giacometti and Toby S. Hudson
  J. Chem. Phys. 140, 081101 (2014) [*Chapter 5*]

- *Left or right cholesterics? A matter of helix handedness and curliness*
  Elisa Frezza, Alberta Ferrarini, **Hima Bindu Kolli**, Achille Giacometti, Giogio Cinacchi
  Phys. Chem. Chem. Phys., 16(30), 16225-32 (2014)

- *Self assembly of hard helices: a rich and unconventional polymorphism*
  Hima Bindu Kolli, Elisa Frezza, Giorgio Cinacchi, Alberta Ferrarini, Achille Giacometti, Toby S. Hudson, Cristiano De Michele and Francesco Sciortino
  Soft Matter, 10(41), 8171 (2014) [Chapter 4 and Chapter 6]

Contents

Declaration of Authorship i

Abstract ii

Listofpublications iii

Contents iv

List of Figures vii

List of Tables xiv

1 Introduction 1
- 1.1 Liquid crystals . . . 1
- 1.2 Liquid crystal phases formed by anisotropic molecules . . . 2
  - 1.2.1 Liquid crystal phases of chiral molecules . . . 5
- 1.3 Why helices? . . . 7
- 1.4 Phase behaviour of hard rods . . . 10
- 1.5 Thesis outline . . . 12

2 Monte Carlo methods 13
- 2.1 Introduction . . . 13
- 2.2 Importance sampling . . . 14
- 2.3 Metropolis algorithm . . . 15
- 2.4 Monte Carlo in various ensembles . . . 16
  - 2.4.1 Canonical Monte Carlo simulation (NVT MC) . . . 16
  - 2.4.2 Isothermal-isobaric Monte Carlo simulation (NPT MC) . . . 17
- 2.5 Details of the MC simulation of hard helices . . . 19

3 Isotropic to nematic phase transition of hard helical particles 21
- 3.1 Introduction . . . 21
- 3.2 Model of the helix . . . 22
- 3.3 Isotropic to nematic phase transition (IN) . . . 24
  - 3.3.1 Nematic order parameter $\langle P_2 \rangle$ . . . 26
- 3.4 NPT Monte Carlo Simulation details . . . 27
  - 3.4.1 Overlap Check . . . 28

3.5 Results and Discussion . . . 29
3.5.1 Defining an aspect ratio for helix? . . . 31
3.5.2 Conclusions . . . 32

4 Packing of helices by Isopointal set Structural Search Method(ISSM) 34
4.1 Introduction . . . 34
4.2 Isopointal set Structural search Method(ISSM) . . . 35
4.2.1 Two dimensional search space . . . 35
4.2.1.1 Wallpaper groups . . . 35
4.2.1.2 Wyckoff sites . . . 37
4.2.1.3 Isopointal sets . . . 38
4.3 Implementation of ISSM on helical particles in 2D . . . 38
4.3.1 Algorithm . . . 39
4.3.2 Simulated annealing technique . . . 39
4.4 Shapes studied . . . 40
4.5 Overlap detection . . . 40
4.6 Calculating volume fraction . . . 42
4.7 Results and Discussion . . . 43
4.7.1 Maximal packing density as a function of radius and pitch . . . 44
4.8 Conclusions . . . 45

5 Evidence of new screw-like nematic phase 47
5.1 Introduction . . . 47
5.2 Understanding screw-like order . . . 48
5.3 Experimental evidence of the screw nematic phase . . . 50
5.4 Characterization of the screw Nematic(N_S^*) . . . 50
5.5 Results and discussion . . . 52
5.5.1 N - N_S^* transition . . . 53
5.5.2 I - N_S^* transition . . . 58
5.5.3 Phase diagrams showing the effect of radius and pitch on Screw-like order . . . 62
5.6 Conclusions . . . 65

6 Characterization of the smectic phases of hard helices 68
6.1 Introduction . . . 68
6.2 Order parameters and correlation functions to characterize higher density phases . . . 69
6.2.1 smectic order parameter . . . 69
6.2.2 Hexatic order parameter . . . 70
6.2.3 Q_4 and Q_6 bond order parameters . . . 72
6.2.4 Parallel and perpendicular pair correlation functions . . . 74
6.3 Types of smectic phases observed . . . 74
6.3.0.1 smectic A with screw like order ($Sm_{A,S}^*$) . . . 75
6.3.0.2 smectic B with screw like order ($Sm_{B,S}^*$) . . . 75
6.3.0.3 smectic B with polar order ($Sm_{B,P}$) . . . 75
6.4 Results and Discussion . . . 75
6.4.1 Equation of state for r = 0.2, p = 8 . . . 76
6.4.2 Equation of state for r = 0.2, p = 4 . . . 84

6.4.3 Equation of state for r = 0.4, p = 4 91
6.4.4 Phase diagrams showing the effect of radius and pitch on smectic phases 95
6.4.4.1 Phase diagram for r = 0.1 95
6.4.4.2 Phase diagram for r = 0.2 95
6.4.4.3 Phase diagram for r = 0.4 98
6.4.5 Evidence of Columnar phase after smectics? 99
6.5 Conclusions 101

7 Summary 104

A Relation between the length and number of turns of the helix 106

B Checking for the overlap between two rigid helices 108

C Definition of the Frenet frame 109

D Correlation functions of various nature 110
D.1 Parallel and perpendicular correlation functions 110
D.2 Coefficients of rotational invariants 112

Bibliography 115

List of Figures

1.1 System of rod-like particles in (a) isotropic liquid-like state and (b) crystal state . . . 2
1.2 Alignment along director $\hat{\mathbf{n}}$ in nematic phase . . . 3
1.3 Schematic of alignment in smectic A phase in the system of rods . . . 4
1.4 A top view of molecules within a layer of (a) Sm_A showing no hexagonal ordering (b) Sm_B showing short range hexagonal order and (c) crystal like structure with long range hexagonal order . . . 5
1.5 Schematic of the tilted layers in Sm_C phase. θ is the tilt angle with respect to the director $\hat{\mathbf{n}}$. Dashed lines are the guidelines indicating the average layer positions . . . 5
1.6 Schematic structure of a right-handed chiral nematic phase. Black arrows represent the orientation of director, which rotates perpendicularly to **z**-axis in a helical manner. . . . 7
1.7 Nano scale B-DNA approximated to cylinders. The Stacking of DNA is shown by the stacking of cylinders. This picture is taken from the work done by Michi Nakata *etal.* [1] . . . 9
1.8 (a) Coarse-grained model of DNA duplexes used in studying the stacking interaction of DNA. This picture is taken is taken from the work done by Cristiano *etal.* [2]. (b) dsDNA represented by dielectric cylinders with helical strands of point-like negative charges at the surface. This picture is taken from the work done by Alexei A. Kornyshev *etal.* [3] [4] . . . 9
1.9 Left: Helical shape of fd virus. Picture taken from the ref. Right: Length distribution of flagella isolated from strain SJW1103 and florescently labelled flagella showing different shapes. This picture is taken from the work [5]. . . . 10
1.10 Phase diagram of hard spherocylinders . . . 11

3.1 Model helix made up of 15 partially fused hard spheres of diameter D with $\Lambda = z_{15} - z_1$. r_{max} being $2r+D$ and p is the distance along z axis in making one complete turn. . . . 23
3.2 Shapes with different r and p. For comparison a fully extended Linear hard sphere chain(LHSC) is shown . . . 24
3.3 Cartoon of the overlap between the spherocylinders containing a pair of helices . . . 28
3.4 Pressure(P^*) as a function of volume fraction (left) η and $\langle P_2 \rangle$(right) as a function of η (right) for LHSC. Results from MC simulations are shown in closed circles and from Onsager theory with PL(dashed line) or MPL(solid line) approximation. Insets on the right panel are representative snapshots for Isotropic and Nematic phases obtained by using QMGA software . . . 29

3.5 Pressure(P^*) as a function of volume fraction η (left) and $\langle P_2 \rangle$(right) as a function of η (right) for helix with $r = 0.2$, $p = 8$. Results from MC simulations are shown in closed circles and from Onsager theory with PL(dashed line) or MPL(solid line) approximation. 30
3.6 Pressure(P^*) as a function of volume fraction η (left) and $\langle P_2 \rangle$(right) as a function of η (right) for helix with $r = 0.2$, $p = 4$. Results from MC simulations are shown in closed circles and from Onsager theory with PL(dashed line) or MPL(solid line) approximation. 31
3.7 Pressure(P^*) as a function of volume fraction *eta* and $\langle P_2 \rangle$(right) as a function of *eta* (right) for helix with $r = 0.2$, $p = 2$. Results from MC simulations are shown in closed circles and from Onsager theory with PL(dashed line) or MPL(solid line) approximation. 31
3.8 Figure showing $\langle P_2 \rangle$ order parameter for helices with radius 0.3 and different pitches 32
3.9 helices with nearly same aspect ratios with different locations of IN transition 32

4.1 Optimal two-dimensional packing in wallpaper group p1 of helices with radius 0.3 and pitch 3. The perimeter of the red circle represents the helical radius. The perimeter of the black circle represents the maximum extent of the edge of the beads. The small black line represents the orientation of the C_2 axis. 36
4.2 Wallpaper group p2 for helix with radius 0.3 and pitch 3 36
4.3 Wallpaper group p3 for helix with radius 0.3 and pitch 3 36
4.4 Wallpaper group p4 for helix with radius 0.3 and pitch 3 37
4.5 Wallpaper group p6 for helix with radius 0.3 and pitch 3 37
4.6 maximally packed two dimensional structure of helices in the limit case $r = 0$ 38
4.7 3D representation of wall paper groups of helix with radius 0.3 and pitch 3 38
4.8 Helical shapes studied with r ranging from 0.1 to 1.0 and p ranging from 1 to 10 41
4.9 Structures with maximum packing density for helices having $r = 0.9$, $p = 2$ at $\eta = 0.37$; $r = 0.6$, $p = 5$ at $\eta = 0.58$; $r = 0.3$, $p = 7$ at $\eta = 0.76$; . . . 44
4.10 Structures with $N_{occ} = 2$ 44
4.11 Colour map of the maximal volume fraction, η, achievable by a given helix as a function of its radius r and pitch p. The color code is from dark red (high packing) to dark blue(low packing). The value on the side of each helix is its effective aspect ratio,$(\lambda/(2r+D))$. The cartoon on the bottom left of each r, p pair shows the corresponding helix shape 45
4.12 Colour map of the areal number density, A_{den}, achievable by a given helix as a function of its radius r and pitch p. The color code is from dark red (high packing) to dark blue(low packing). 46

5.1 Helix with arrows showing the unit vectors $\hat{\mathbf{u}}$ and $\hat{\mathbf{w}}$ defined in the molecular frame, and the unit vectors $(\hat{\backslash}, \hat{\mathbf{c}})$ defined in the laboratory frame. X,Z are the axes of the laboratory frame, with α the angle between $\hat{\mathbf{w}}$ and the X-axis. 48
5.2 Pair of helices inphase and antiphase 49
5.3 Screw like motion showing translation coupled rotation 49

5.4 Top: Cartoon showing the orientation of the $\hat{\mathbf{u}}$ of helix in cholesteric phase. Middle: Cartoon of the screw-like nematic phase showing the orientation of $\hat{\mathbf{w}}$. Here $\hat{\mathbf{h}}$ is a unit vector parallel to the axis around which $\hat{\mathbf{u}}$ or $\hat{\mathbf{w}}$ rotates. Bottom: Another representation of screw-like nematic showing conical path. Here $\hat{\mathbf{T}}$ is the local tangent of the helix. 50
5.5 Experimental results on flagella SJW1103 [5]. (a) and (b) coexistence and single phage with polarized microscope. (c) fluorescently labelled flagella dissolve in conical medium. (d) phase diagram of flagella (e) schematic showing the excluded volume between two helices. 51
5.6 Equation of state plotted in reduced pressure P^* - volume fraction η plane for helices having r = 0.2 and p = 8. Different colours indicate different phases. Yellow circles(I)-isotropic; Blue circles(N)-nematic; Red circles(N_S^*)-screw nematic; Green circles(Sm)- smectic. 54
5.7 Equation of state plotted in reduced pressure P^* - volume fraction η plane for helices having $r = 0.2$ and $p = 6$. Different colours indicate different phases. Yellow circles(I)-isotropic; Blue circles(N)-nematic; Red circles(N_S^*)-screw nematic; Green circles(Sm)- smectic. 54
5.8 Equation of state plotted in reduced pressure P^* - volume fraction η plane for helices having $r = 0.2$ and $p = 3$. Different colours indicate different phases. Yellow circles(I)-isotropic; Blue circles(N)-nematic; Red circles(N_S^*)-screw nematic; Green circles(Sm)- smectic. 55
5.9 $\langle P_2 \rangle$ plotted as a function of η in the case r = 0.2 and different values of pitch. $p = 3$ (solid circles); $p = 6$ (solid triangles); $p = 8$ (solid squares). . 56
5.10 $\langle P_{1,C} \rangle$ plotted as a function of η in the case r = 0.2 and different values of pitch. $p = 3$ (solid circles); $p = 6$ (solid triangles); $p = 8$ (solid squares). 56
5.11 Correlation functions $g_{1,\parallel}^{\hat{\mathbf{w}}}(R_\parallel)$ showing the emergence of screw-like order with increasing η in case of helices with $r = 0.2$ and $p = 3$. Different colours are used to show correlation at different values of η 57
5.12 Correlation functions $g_{1,\parallel}^{\hat{\mathbf{w}}}(R_\parallel)$ showing the emergence of screw-like order with increasing η in case of helices with $r = 0.2$ and $p = 6$. Different colours are used to show correlation at different values of η 57
5.13 Visual representation of the emergence of screw like order in $N - N_S^*$ transition for the system of helices with $r = 0.2$ and $p = 6$. Snapshots and their corresponding η's are shown. Helices are colour coded according to their local tangent. 58
5.14 Equation of state plotted in reduced pressure P^* - volume fraction η plane for helices having $r = 0.4$ and $p = 8$. Different colours indicate different phases. Yellow circles(I)-isotropic; Blue circles(N)-nematic; Red circles(N_S^*)-screw nematic; Green circles(Sm)- smectic. 59
5.15 Equation of state plotted in reduced pressure P^* - volume fraction η plane for helices having $r = 0.4$ and $p = 6$. Different colours indicate different phases. Yellow circles(I)-isotropic; Red circles(N_S^*)-screw nematic; Green circles(Sm)- smectic. 59
5.16 Equation of state plotted in reduced pressure P^* - volume fraction η plane for helices having r = 0.4 and p = 3. Different colours indicate different phases. Yellow circles(I)-isotropic; Red circles(N_S^*)-screw nematic; Green circles(Sm)- smectic. 60
5.17 $\langle P_2 \rangle$ plotted as a function of η in the case $r = 0.4$ and different values of pitch. $p = 3$ (solid circles); $p = 6$ (solid triangles); $p = 8$ (solid squares). . 60

5.18 $\langle P_{1,c} \rangle$ plotted as a function of η in the case $r = 0.4$ and different values of pitch. $p = 3$ (solid circles); $p = 6$ (solid triangles); $p = 8$ (solid squares) . 61
5.19 Correlation functions $g^{\hat{\mathbf{w}}}_{1,\parallel}(R_\parallel)$ showing the emergence of screw-like order with increasing η in case of helices with r= 0.4 and $p = 3$. Different colours are used to show correlation at different values of η 61
5.20 Correlation functions $g^{\hat{\mathbf{w}}}_{1,\parallel}(R_\parallel)$ showing the emergence of screw-like order with increasing η in case of helices with $r = 0.4$ and $p = 6$. Different colours are used to show correlation at different values of η 61
5.21 Visual representation of $I - N^*_S transition$ for system of helices with $r = 0.4$ and $p = 6$. Snapshots and their corresponding η's are shown. Helices are colour coded according to their local tangent. 62
5.22 Helical shapes with radius ranging from $r = 0.1$ to 0.4 and $p = 2$ to 8. The numbers shown inside the picture are the corresponding aspect ratio values. 63
5.23 Phase digram plotted as η Vs pitch for helices having r = 0.1 and p = 2 to 8. circles indicate isotropic; Squares indicate nematic; triangles indicate smectic and other higher density phases. Shaded regions are rough estimates of the width of the phases. 64
5.24 Phase digram plotted as η Vs pitch for helices having $r = 0.2$ and $p = 2$ to 8. Yellow circles indicate isotropic; Blue squares indicate nematic; Red squares indicate screw nematic; triangles indicate smectic and other higher density phases. 65
5.25 Phase digram plotted as η Vs pitch for helices having $r = 0.3$ and $p = 2$ to 8. Yellow circles indicate isotropic; Blue squares indicate nematic; Red squares indicate screw nematic; triangles indicate smectic and other higher density phases. 66
5.26 Phase digram plotted as η Vs pitch for helices having $r = 0.4$ and $p = 2$ to 8. 66

6.1 The dependence of translational order parameter $\langle \tau_1 \rangle$ on layer spacing for helices having $r = 0.2$, $p = 4$ is shown on either side of $N^*_S - Sm_A$ transition. The maximum value of τ_1 is the smectic order parameter. . . . 71
6.2 Figure showing how the line (dashed line) joining the nearest neighbour helices making an angle θ_{ij} with reference axis(solid line). Helices are projected on to a plane. Red circle denotes the radius of the helix. The short axis inside each circle is the fixed C_2 axis indicating the orientation of helix 71
6.3 Cartoon of the smectic B phases discussed in the text. Circles represent transversal sections through the center of helices and arrows the corresponding $\hat{\mathbf{w}}$ vectors. I, II, III indicate adjacent layers. Left: $Sm^*_{B,S}$ phase, with through-layers positional correlation (AAA strucutre, highlighted by the dashed lines 76
6.4 Equation of state for the system of helices having r = 0.2, p = 8. Different colours indicate different phases. I - isotropic; N - nematic; N^*_S - screw-nematic; $Sm^*_{A,S}$ - screw-smectic A; $Sm_{B,p}$ - polar-smectic B; C - compact phase 77
6.5 Nematic order parameter $\langle P_2 \rangle$ as a function of volume fraction η for helices with r = 0.2 and p = 8. Points are plotted in different colours to indicate different phases. 77

6.6 Screw-like order parameter $\langle P_{1,c} \rangle$ for helices with r = 0.2 and p = 8. Points are plotted in different colours to indicate different phases. 78
6.7 The parallel correlation function $g_{\parallel}(R_{\parallel})$ for helices with r = 0.2 and p = 8, calculated at $\eta = 0.375$, $P^* = 0.9$ in Nematic phase. 78
6.8 The screw-like parallel orientational correlation function $g^{\hat{w}}_{1,\parallel}(R_{\parallel})$ for helices with r = 0.2 and p = 8, calculated at $\eta = 0.379$, $P^* = 0.9$ in Nematic phase, showing no screw like order. 79
6.9 Snapshot of the system of helices having r = 0.2, p = 8 at $\eta = 0.379$ in nematic phase. The colouring is done for each bead of the helix separately according to the local tangent at that bead. 79
6.10 The parallel correlation function $g_{\parallel}(R_{\parallel})$ for helices with r = 0.2 and p = 8, calculated at $\eta = 0.409$, $P^* = 1.0$ in screw-nematic phase. 80
6.11 The screw-like parallel orientational correlation function $g^{\hat{w}}_{1,\parallel}(R_{\parallel})$ for helices with r = 0.2 and p = 8, calculated at $\eta = 0.409$, $P^* = 1.0$ in screw-nematic phase 80
6.12 Snapshot of the system of helices having r = 0.2, p = 8 at $\eta = 0.409$, $P^* = 1.0$ in screw-nematic phase. The colouring is done for each bead of the helix separately according to the local tangent at that bead. Regular colour stripes indicate the phase as special chiral screw-nematic 81
6.13 smectic order parameter $\langle \tau_1 \rangle$ as a function of volume fraction η for helices with r = 0.2 and p = 8. Points are plotted in different colours to indicate different phases. 81
6.14 The parallel correlation function $g_{\parallel}(R_{\parallel})$ for helices with r = 0.2 and p = 8, calculated at $\eta = 0.458$, $P^* = 1.1$, in screw-smectic A. 82
6.15 The screw orientational parallel correlation function $g^{\hat{\mathbf{w}}}_{1,\parallel}(R_{\parallel})$ for helices with r = 0.2 and p = 8, calculated at $\eta = 0.458$, $P^* = 1.1$, in screw-smectic A. 82
6.16 The perpendicular correlation function $g_{\perp}(R_{\perp})$ for helices with r = 0.2 and p = 8, calculated at $\eta = 0.458$, $P^* = 1.1$, in screw-smectic A. 83
6.17 Snapshot of the system of helices having r = 0.2, p = 8 at $\eta = 0.458$ in screw-smectic A phase. The colouring of beads is done according to the local tangent of the helix. 83
6.18 The screw orientational parallel correlation function $g^{\hat{\mathbf{w}}}_{1,\parallel}(R_{\parallel})$ for helices with r = 0.2 and p = 8, calculated at $\eta = 0.515$, $P^* = 1.3$, in polar smectic B. 84
6.19 The perpendicular correlation function $g_{\perp}(R_{\perp})$ for helices with r = 0.2 and p = 8, calculated at $\eta = 0.515$, $P^* = 1.3$, in polar smectic B. 84
6.20 Hexatic order parameter $\langle \psi_6 \rangle$ as a function of volume fraction η for helices with r = 0.2 and p = 8. Points are plotted in different colours to indicate different phases. 85
6.21 Average number of nearest neighbours $\langle n \rangle$ as a function of volume fraction η for helices with r = 0.2 and p = 8. Points are plotted in different colours to indicate different phases. 85
6.22 Snapshot of the system of helices having r = 0.2, p = 8 at $\eta = 0.458$ in screw-smectic A phase. The colouring of beads is done according to the local tangent of the helix. 86
6.23 Snapshot of the system of helices having r = 0.2, p = 8 at $\eta = 0.458$ in polar-smectic B phase. The colouring is done according to the C_2 axes of the helices. 86

6.24 Q4 and Q6 bond order parameters as a function of volume fraction η for helices with r = 0.2 and p = 8. Points are plotted in different colours to indicate different phases. 87
6.25 Figure showing the sequence of phases and their representative snapshots in the case of helices with r = 0.2 and p = 8. 87
6.26 Equation of state for the system of helices having r = 0.2, p = 4. Different colours indicate different phases. I - isotropic; N - nematic; N_S^* - screw-nematic; $Sm_{A,S}^*$ - screw-smectic; $Sm_{B,S}$ - screw-smectic B; C - compact phase 88
6.27 Nematic order parameter $\langle P_2 \rangle$ as a function of volume fraction η for helices with r = 0.2 and p = 4. 89
6.28 Screw-like order parameter $\langle P_{1,c} \rangle$ as a function of volume fraction η for helices with r = 0.2 and p = 4. 89
6.29 Smectic order parameter $\langle \tau_1 \rangle$ as a function of volume fraction η for helices with r = 0.2 and p = 4. 89
6.30 Hexatic order parameter $\langle \psi_6 \rangle$ as a function of volume fraction η for helices with r = 0.2 and p = 4. 90
6.31 Average number of nearest neighbours $\langle n \rangle$ as a function of volume fraction η for helices with r = 0.2 and p = 4. 91
6.32 Average Q4 and Q6 bond order parameters as a function of volume fraction η for helices with r = 0.2 and p = 4. 91
6.33 Figure showing the sequence of phases and their representative snapshots in the case of helices with r = 0.2 and p = 4. 92
6.34 Equation of state for the system of helices having r = 0.4, p = 4. Different colours indicate different phases. I - isotropic; N_S^* - screw-nematic; $Sm_{B,S}$ - screw-smectic B; C - compact phase 92
6.35 Average Q4 and Q6 bond order parameters as a function of volume fraction η for helices with r = 0.4 and p = 4. 93
6.36 The parallel correlation function $g\|(R_\|)$ for helices with r = 0.4 and p = 4, calculated at $\eta = 0.493$, $P^* = 1.5$, in screw smectic B phase. 94
6.37 The parallel correlation function $g\perp(R_\perp)$ for helices with r = 0.4 and p = 4, calculated at $\eta = 0.493$, $P^* = 1.5$, in screw-smectic B phase. 94
6.38 The screw orientational parallel correlation function $g_{1,\|}^{\hat{\mathbf{w}}}(R_\|)$ for helices with r = 0.4 and p = 4, calculated at $\eta = 0.493$, $P^* = 1.5$, in screw smectic B phase. 94
6.39 Full phase diagram of the helices with r = 0.1 shown in the plane of volume fraction η and pitch of the particle. Points plotted as circles indicate Isotropic phase; squares indicate Nematic; triangles indicate smectic phase. Different colours indicate different phases observed. Yellow - Isotropic; Blue - Nematic; Light green - smectic A; Dark green - smectic B 96
6.40 Surface plot of screw-like order parameter $P_{1,c}$ plotted in the plane of η and pitch of the helix for r = 0.1 96
6.41 Full phase diagram of helices with r = 0.2 shown in the plane of volume fraction η and pitch of the particle. Points plotted as circles indicate Isotropic phase; squares indicate Nematic; triangles indicate smectic phase and diamonds indicate crystal like structure. Different colours indicate different phases observed. Each colour is labelled by the phase observed. . 97
6.42 Surface plot of screw-like order parameter $P_{1,c}$ plotted in the plane of η and pitch of the helix for r = 0.2. 97

6.43 Full phase diagram of helices with r = 0.4 shown in the plane of volume fraction η and pitch of the particle. Points plotted as circles indicate Isotropic phase; squares indicate Nematic; triangles indicate smectic phase and diamonds indicate crystal like structure. Different colours indicate different phases observed. Each colour is labelled by the phase observed. . 98
6.44 Surface plot of screw-like order parameter $P_{1,c}$ plotted in the plane of η and pitch of the helix for r = 0.4. 99
6.45 smectic order parameter $\langle P_{1,c} \rangle$ as a function of volume fraction η for helices with r = 0.3 and p = 3. 100
6.46 The parallel correlation functions $g\perp(R_\perp)$ for helices with r = 0.3 and p = 3, calculated at $\eta = 0.399; 0.461; 0.484$. 100
6.47 The perpendicular correlation function $g\perp(R_\perp)$ for helices with r = 0.3 and p = 3, calculated at $\eta = 0.484$. 100
6.48 The screw orientational parallel correlation function $g^{\hat{\mathbf{w}}}_{1,\parallel}(R_\parallel)$ for helices with r = 0.3 and p = 3, calculated at $\eta = 0.484$, $P^* = 1.3$, in screw smectic B phase. 101
6.49 Snapshot of the system of helices having r = 0.3, p = 3 at $\eta = 0.399$ in $Sm^*_{B,S}$ phase. The colouring is done according to the position of the helices. 101
6.50 Snapshot of the system of helices having r = 0.3, p = 3 at $\eta = 0.484$ in columnar phase phase. The colouring is done according to the position of the helices. 102
6.51 Snapshot of the system of helices having r = 0.3, p = 3 at $\eta = 0.484$ in columnar phase. The colouring is done according to the local tangent of the helices. 102

List of Tables

1.1 Reported smectic phases 6
1.2 Examples of biological liquid crystals 8

Chapter 1

Introduction

1.1 Liquid crystals

Matter was for a long time classified into three states: solid, liquid and gas. This picture changed in the late eighteen eighties, when it was discovered that the transition between solid and liquid states is not always direct. It is possible for a series of transitions to occur between solid and liquid, giving rise to intermediate phases called mesophases. These mesophases have structural, optical and mechanical properties between those of solid and liquid. For this reason, these mesomorphic phases are termed as 'liquid crystals'[6] [7].

Liquid crystals were first discovered in 1888 by Austrian botanist Friedrich Reinitzer [8], while doing experiments on cholesteryl benzoate. Instead of a direct solid to liquid transition, he found that it undergoes two transitions: solid first melts into cloudy liquid and then to a clear liquid. Later Otto Lehmann performed polarised optical microscopic measurements confirming the crystal behaviour of the cloudy liquid and coined the word "liquid crystal" for the intermediate phase. Until 1960's, few studies were done because of the lack of direct applications of liquid crystals. Research on liquid crystals dramatically increased in 1970's and 1980's after the discovery of switchable optical properties of liquid crystals for display technologies. Different types of systems, like micellar solutions of surfactants [9], certain organic molecules, polymers [10] and many biomolecules [11] exhibit liquid crystalline phases.

In solids, molecules are constrained to occupy lattice sites and point their molecular axes in a specific direction. Thus a crystal exhibit three dimensional positional order and orientational order. In liquids, molecules usually occupy random positions and posses random orientations. Thus liquid lacks long-range positional or orientational

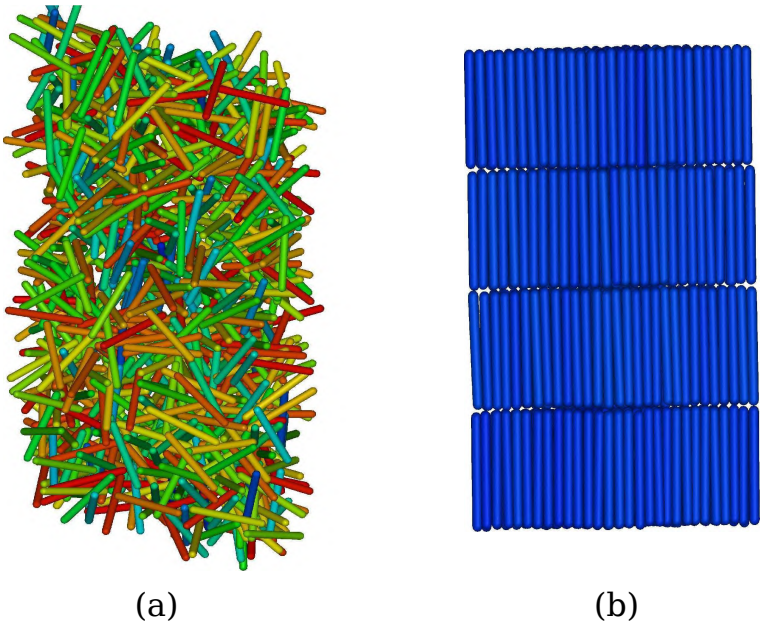

FIGURE 1.1: System of rod-like particles in (a) isotropic liquid-like state and (b) crystal state

order. Figure 1.1 shows an example of isotropic fluid with random orientations and a crystal structure of the system of rods.

Liquid crystals are characterized by the orientational order and positional order either in one or two dimensions [6] [7]. They exhibit liquid like order in at least one direction and posses degree of anisotropy which is characteristic of some sort of order. Typically these requirements are met if the particles are anisotropic in shape either rod-like or disc-like [12] [13]. However all anisotropic molecules do not form liquid crystal phases [14].

1.2 Liquid crystal phases formed by anisotropic molecules

Molecules having shape anisotropy may have three types of order. The simplest order is orientational order [15] [16]. This describes the extent of alignment of symmetry axes of molecules along a specific direction. The second type is positional or translational order in either one or two dimensions. Positional order is a general term describing the extent of translational symmetry shown by molecules. The third is the bond orientational order. Here bond is not a chemical bond but a line joining the adjacent molecules. Depending on the type of order present, molecules exhibit different liquid crystalline phases. On going from the least ordered phase (isotropic (I) shown in 1.1) to the most ordered phase (crystal) with increasing density, we see the following liquid crystal phases.

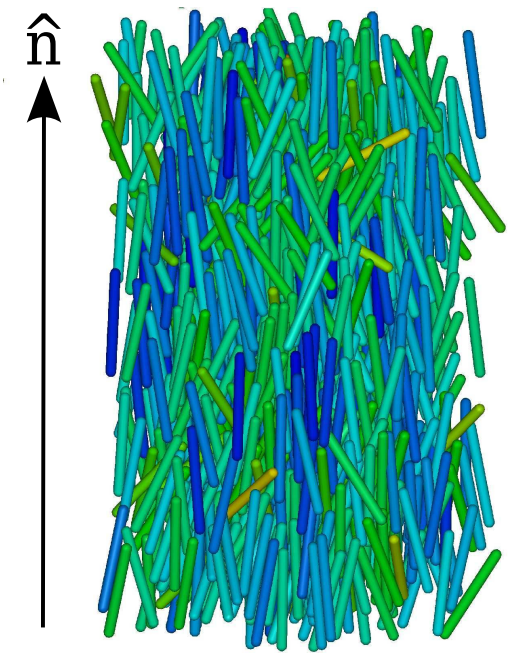

FIGURE 1.2: Alignment along director $\hat{\mathbf{n}}$ in nematic phase

The Nematic phase (N)

The simplest liquid crystal phase is the nematic phase (N). Nematic phases are characterized by long range orientational order (usually of a single particle axis) and the absence of long-range positional order. In the nematic phase, all molecules orient themselves along a specific direction denoted as a director $\hat{\mathbf{n}}$. The word nematic is derived from a Greek word $\nu\eta\mu\alpha$ (nema), which means thread. This is because of thread like disclinations observed in the nematic phase. In rod shaped molecules, the long axis of the molecules is the director and in the disc-shaped molecules the normal to the disc is the director. The correlation lengths, parallel to $\hat{\mathbf{n}}$ and perpendicular to $\hat{\mathbf{n}}$ are not equal. The uniaxial symmetry of the director is an important feature of the nematic phase i.e., $\hat{\mathbf{n}}$ and -$\hat{\mathbf{n}}$ are not distinguishable. Random distribution of centres of mass about $\hat{\mathbf{n}}$ indicates the lack of positional order. It is important to understand the long range orientational order which is causing the anisotropic properties of the nematic phase. The details of the uniaxiality and nematic order parameter are discussed in detail in chapter 3.

The smectic A phase (Sm_A)

The second common type of liquid crystal phase is called smectic phase. Semctic phases have layered structure and thus more ordered compared to nematic phase. The director and the normal to the layer are the two main directions in smectic phases. The word 'smectic' is derived from a Greek word *smektikos*, which means soap. This is because the thick and slippery substance at the bottom of a soap is smectic liquid crystal. There are several types of smectic phases showing important structural variations. The simplest is smectic A Sm_A. The presence of positional order in the same direction that the particles

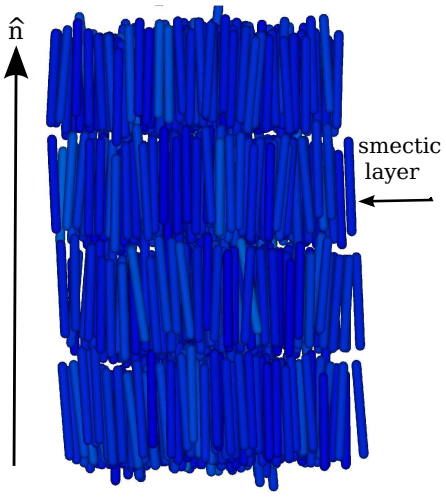

FIGURE 1.3: Schematic of alignment in smectic A phase in the system of rods

are aligned leads to Sm_A. Sm_A can be viewed as stacking of two dimensional fluids with well defined inter-layer spacing. All molecules are oriented in parallel direction to the layer normal as shown in the figure 1.3. This phase is incompressible and uniaxial. More details about the characterization of different smectic phases are given in chapter 6.

The smectic B phase(Sm_B)

This phase is characterized by a layered structure and long range bond orientational order within the layers. As mentioned before, bonds are the lines joining the adjacent molecules. The system possesses bond orientational order if the orientation of these bonds is maintained over a long range. The molecules can best pack in a hexagonal structure giving rise to six fold symmetry in the orientation of bonds. In Sm_B phase, molecules posses local hexagonal ordering within the layers and their orientational alignment is the same as that observed in Sm_A. This is a special class of smectics [17]. This phase is characterized by long range positional order in the direction perpendicular to layers and short range positional order within the layers. A top view of the molecules within a plane in Sm_A, Sm_B and a crystal structure is shown in the figure 1.4. The top view of the layer in Sm_A phase shows a random arrangement of particles while Sm_B phase shows short range hexagonal order and crystal shows long range hexagonal order.

Tilted smectics: smectic C phase (Sm_C)

The Sm_C phase is similar to Sm_A phase as this is a layered structure and positions of molecules in each layer are random. However, molecules are on average, tilted with respect to the layer normal. The layer normal and the director are not collinear as shown in figure 1.5. There are various tilted phases possessing different structures just like the untilted phases.

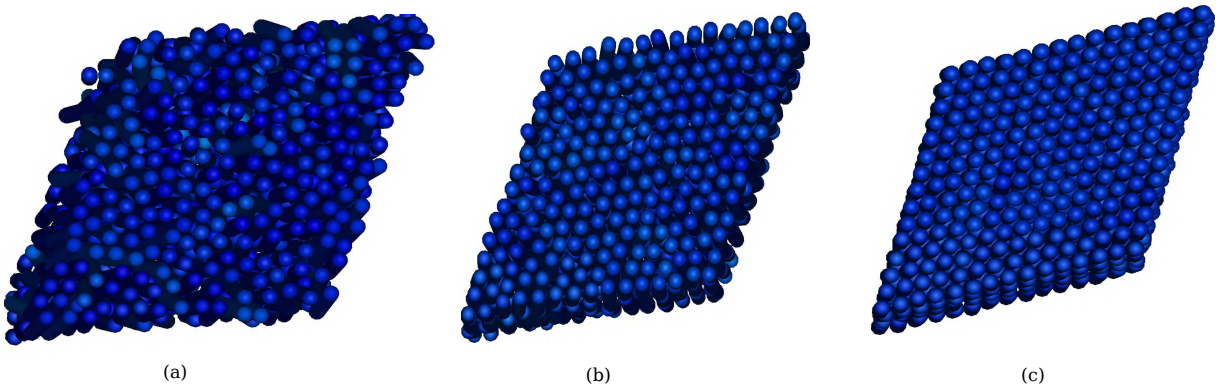

FIGURE 1.4: A top view of molecules within a layer of (a) Sm_A showing no hexagonal ordering (b) Sm_B showing short range hexagonal order and (c) crystal like structure with long range hexagonal order

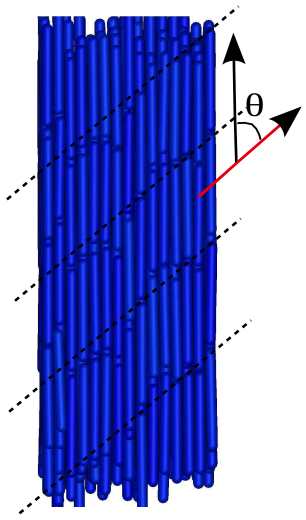

FIGURE 1.5: Schematic of the tilted layers in Sm_C phase. θ is the tilt angle with respect to the director $\hat{\mathbf{n}}$. Dashed lines are the guidelines indicating the average layer positions

There are 12 different smectic phases identified so far. The list of all these phases is given in the table 1.1. This classification is done based on the tilt position of the layer and the bond orientational order in molecular packing. Some of these phases are considered as crystal smectics.

1.2.1 Liquid crystal phases of chiral molecules

A molecule which cannot be superimposed on its mirror image is called a chiral molecule *eg.* helix. A molecule is achiral when an improper rotation (which is a combination of a rotation and a reflection in a plane perpendicular to the axis of rotation) results in the same molecule. Chiral molecules lack such kind of symmetry. Handedness is a phenomenon which is able to classify the chiral molecules into 'right-' and 'left-' handed

TABLE 1.1: Reported smectic phases

Smectic type	Phase type	Molecular packing	Tilt position
A	fluid	random	orthogonal
B	hexatic	hexagonal	orthogonal
C	fluid	random	tilted
D	plastic	micellar?, rod? —	
E	crystal	orthorhombic	orthogonal
F	hexatic	pseudo-hexagonal	tilt to side
G	crystal	pseudo-hexagonal	tilt to side
H	crystal	herringbone monoclinic	tilted
I	hexatic	pseudo-hexagonal	tilt to apex
J	crystal	pseudo-hexagonal	tilt to apex
K	crystal	herringbone monoclinic	tilted
L	crystal	hexagonal	orthogonal

http://www.mc2.chalmers.se/pl/lc/engelska/tutorial/smectable.html

[18]. "All handed objects are chiral but not all chiral objects are handed" [18] *eg.* potato. A system is said to be homochiral if all the molecules of the system are of the same chiral form (same handedness). Nearly all bio-polymers are homochiral in nature. Amino acids that comprise proteins are left handed and all sugars in DNA and RNA tend to be right handed.

The chirality in the molecular shape has strong impact on liquid crystal properties. Usually chiral mesophases are formed by chiral mesogens. Recent results have shown some achiral molecules forming chiral mesophases [19]. However, the origin of the chirality and the propagation of chirality from individual molecule to mesophase is still an open question. Chiral mesophases are characterized by the helical twisting of the long axis of the molecules. Like achiral molecules, chiral molecules form nematic and smectic phases with an additional helical twist.

The chiral nematic or cholesteric phase N^*

The nematic phase shown by chiral molecules is called chiral nematic or cholesteric phase N^*. The intrinsic chirality of the molecule produces intermolecular forces that favour alignment of molecules but at a slight angle to one another. This leads to the helical distortion of the nematic director $\hat{\mathbf{n}}$ in which $\hat{\mathbf{n}}$ rotates about its perpendicular direction say '$\mathbf{z}$' with an angle $2\pi/P$. Here P is cholesteric pitch which is equal to the distance it takes for $\hat{\mathbf{n}}$ to make 360° rotation. Chiral nematic phase can be viewed as a stack of nematic layers with the director showing some twist with respect to the director in the layers below and above. In a chiral nematic phase the director shows a continuous helical twist about the direction perpendicular to the director '$\mathbf{z}$' as illustrated in the figure 1.7. The double headed black arrows in the figure represent the orientation of the director in the layers. Chiral nematic phases which have a small twist and large cholesteric pitch

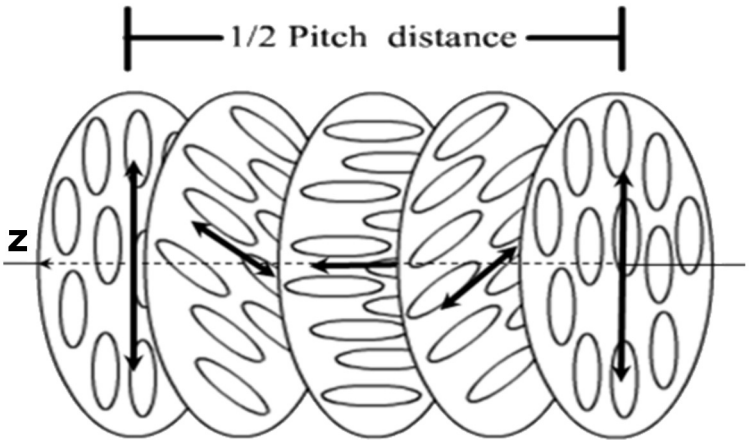

FIGURE 1.6: Schematic structure of a right-handed chiral nematic phase. Black arrows represent the orientation of director, which rotates perpendicularly to **z**-axis in a helical manner.

are considered locally nematic. The chiral phases are usually designated with an asterisk next to letter *eg.* N^*. Chiral molecules also exhibit chiral tilted phases like the chiral smectic C Sm_C^* in which the director precesses about the layer normal in going from layer to layer.

1.3 Why helices?

Helical shape has always a special importance in nature. Many systems like polynucleotides, polypeptides and viruses acquire helical shapes. Because of their shape anisotropy, all these particles exhibit liquid crystal phases at high densities. At such high densities, the shape of the helices start to be relevant and affects the liquid crystal ordering. New functional materials [20] [21]can be produced by exploiting the intrinsic chirality of the helical structures, which are useful in catalysis and demixing of enantiomers [22] [23].

Bio-molecules like nucleic acids, proteins, carbohydrates and fats exhibit liquid crystal phases [11]. Their synthetic counterparts are also studied for biological applications such as biosensors. Biological liquid crystals are known to display hexagonal, smectic, blue phases, chiral-nematic and nematic phases depending on various parameters. The rigid shape anisotropy, the ionic environment that regulates charge on molecule and the concentration of molecules dictate the phase of the liquid crystal.

Table 1.2 shows some examples of bio-molecules and their liquid crystal organization [11]. Although all these molecules have chiral structure, TMV virus form a nematic phase, the fd virus, DNA (Deoxyribonucleic acid) and collagen form chiral nematic phase and

Table 1.2: Examples of biological liquid crystals

Biomaterial	liquid crystal organization
DNA	isotropic - blue phases - precholesteric - cholesteric - hexagonal
Collagen	coexistence, isotropic and chiral nematic phases
fd virus	finger-print texture chiral-nematic phases
TMV	coexistence, isotropic - nematic
Helical flagella from S typhimurium	coexistence, isotropic and conical

helical flagella form a new phase called a 'conical phase' [5]. The reason for this behaviour remains unknown and some of these issues will be addressed in this work.

Because of its biological interest, DNA is the most emblematic of all helical biomolecular systems. The DNA molecules can be compacted to give high-ordered packing structures. At such high concentrations, DNA molecules show liquid crystal phases like blue, cholesteric, hexagonal columnar or hexatic [24] and crystalline phases which are sensitive to various parameters [11]. DNA is a right handed helix, but makes left handed superhelices in cholesteric phase. The features of the cholesteric phase like pitch and handedness depend on the geometry of the helix [25] [26]. Due to the end to end hydrophobic interactions, short DNA duplexes stack one top on other forming a long DNA. Due to stacking, DNA does not show smectic phases but allow very short DNA to make cloumnar phase. Rill et al. mistakenly identified a smectic phase for nucleosomal DNA [27], but later Livolant disproved this claim by looking at the defects in the texture. The same end-to-end interaction was later invoked by Zanchetta et al. in their study of the mesophase behavior of the ultra-short DNA [1]. The densest liquid crystalline phase of DNA is the columnar hexagonal [28]. Long range hexagonal bond orientational order with short positional order is found in case of long DNA [24]. In the phase diagram of long DNA, the hexatic phase of very long DNA displaces the columnar hexagonal phase present for the short fragment DNA. The hexatic order is analysed in the Chapter 6. Due to the similarity in shape, dsDNA (double stranded Deoxyribonucleic acid) are often approximated to rods, overlooking the effect of helical shape. The coexistence lines of liquid crystal phases obtained from the experiments on DNA are often compared to those predicted by the Onsager theory and computer simulations done on hard spherocylinders. To compare with the phase diagram of spherocylinder, the effective diameter of the helix is considered as the diameter of the spherocylinder. Figure 1.7 shows recent experimental results on short DNA where the helices are assimilated to rods [1]. Also the numerical simulations on DNA stacking are done by mimicking helix to rod-like structure [2]. Kornyshev modelled DNA as a cylinder with helical charge distribution on the surface of the cylinder as shown in figure 1.8 to study electrostatic interactions [3] [4]. This clearly tells us that the effect of helical shape on the liquid crystal phase diagram of DNA has been neglected.

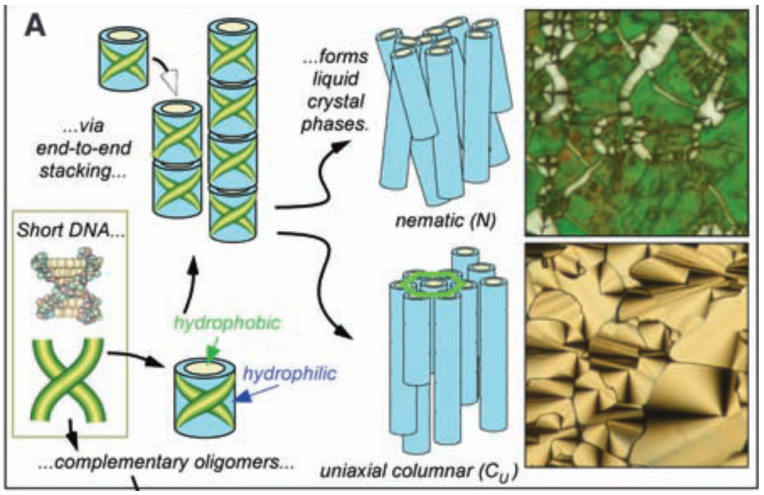

FIGURE 1.7: Nano scale B-DNA approximated to cylinders. The Stacking of DNA is shown by the stacking of cylinders. This picture is taken from the work done by Michi Nakata *etal.* [1]

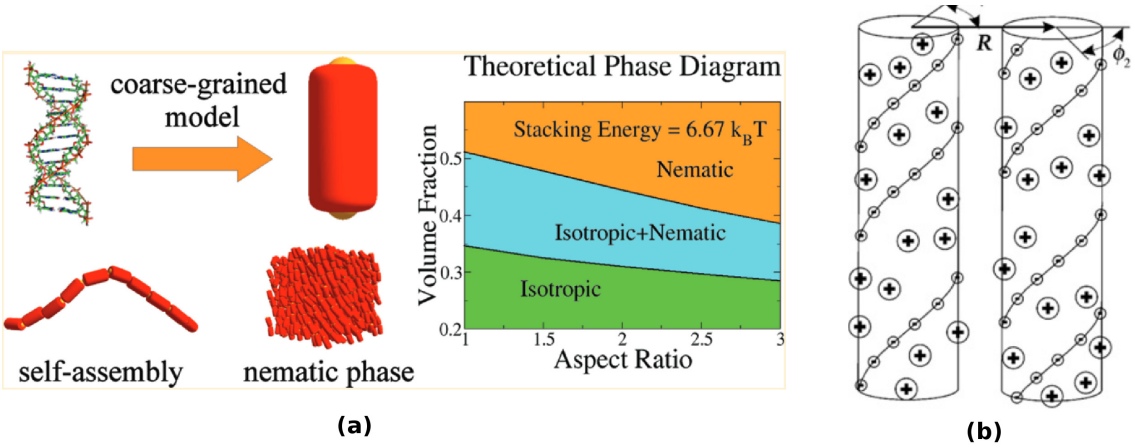

FIGURE 1.8: (a) Coarse-grained model of DNA duplexes used in studying the stacking interaction of DNA. This picture is taken is taken from the work done by Cristiano *etal.* [2]. (b) dsDNA represented by dielectric cylinders with helical strands of point-like negative charges at the surface. This picture is taken from the work done by Alexei A. Kornyshev *etal.* [3] [4]

Other interesting helical systems showing liquid crystal phases are the suspensions of filamentous bacterophages, denoted by fd viruses and helical flagella. The rod like fd virus is a micron-length semi flexible poly-electrolyte formed by a ssDNA(single stranded DNA) around which proteins are coated [29]. The suspensions of fd virus in aqueous solutions form isotropic, chiral nematic, smectic and columnar phases [11]. Although fd virus has helical charge distribution, they can be sterically stabilized by binding polymers on its surface [30]. Due to the electrostatic repulsion, the effective diameter D_{eff} is larger than the diameter of the bare molecule and D_{eff} changes with ionic strength. It is reported that the flexibility of the virus depends on the temperature [31]. The advantage with this kind of colloidal suspensions is that they are monodisperse

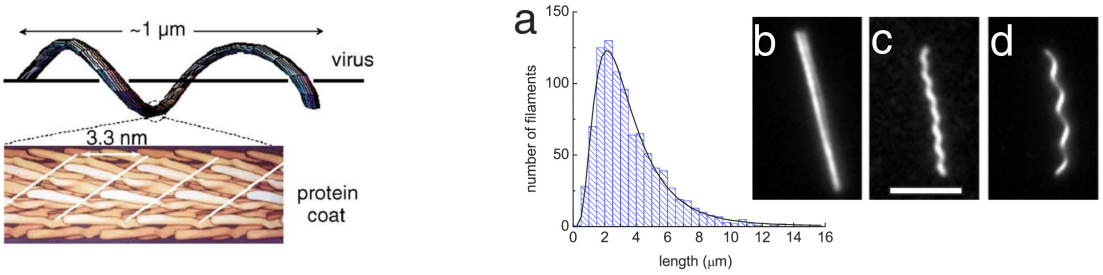

FIGURE 1.9: Left: Helical shape of fd virus. Picture taken from the ref. Right: Length distribution of flagella isolated from strain SJW1103 and florescently labelled flagella showing different shapes. This picture is taken from the work [5].

enough to form smectic phases [32] [33]. Although TMV and $pf1$ viruses are chiral in structure, they form nematic instead of chiral nematic phase [29]. Like this, there are several questions unexplained about the phase behaviour of virus particles. The results obtained are always compared with the results obtained from the Onsager theory of hard rods. There are obvious deviations from the theory. Our model of interest i.e., hard helices are more similar to this colloidal virus suspensions than the hard rods. Thus finding the phase behaviour of helical particles help us to understand the phase behaviour of fd virus.

Flagellar filaments are helical structures assembled from a single protein called flagellin. The advantage of this flagellum is that its helical shape is tunable. From rod-like shapes to curly helical shapes can be produced by changing the flagellin amino acid sequence, the pH and the temperature of the suspension [5]. Though the flagella are chiral, studies report that they do not exhibit a chiral nematic phase. Instead it is reported that they show “conical phase". This will be focussed again in chapter 3. Figure 1.9 shows the helical shapes of fd virus and flagellum.

In order to gain a better understand on the liquid crystal behaviour of these biomolecules, it is necessary to study the effect of helical shape on liquid crystal phases. We have modelled a right handed helix as a chain of hard spheres and performed Monte Carlo simulation to obtain the liquid crystal phases. Different shapes of helix are studied by varying the helical parameters. We have taken the phase diagram of hard spherocylinder as the reference since hard-helix approaches hard-rod in the limit.

1.4 Phase behaviour of hard rods

Before going to discuss about the phase behaviour of helix, I will introduce the phase diagram of spherocylinders [34]. Figure 1.10 shows the phase diagram of hard spero-cylinders. Different liquid crystal phases are shown by plotting volume fraction against

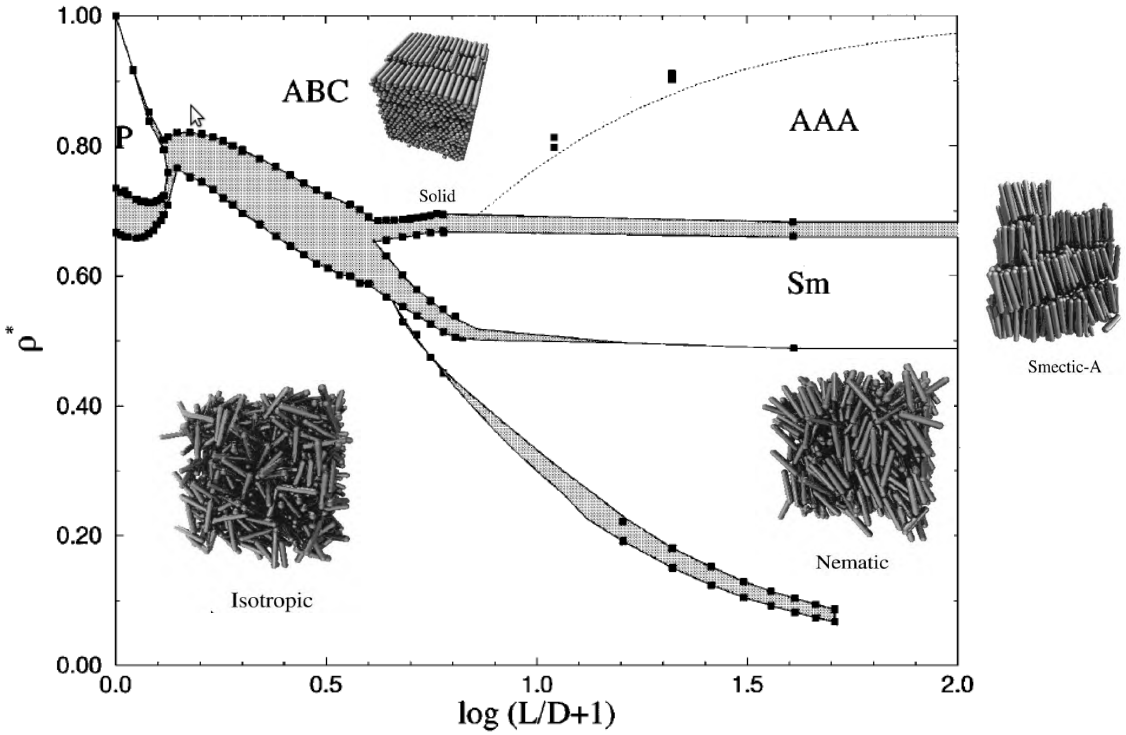

FIGURE 1.10: Phase diagram of hard spherocylinders

logarithm of aspect ratio. The aspect ratio of spherocylinder is defined as L/D where L is the length of the spherocylinder and D is the width of the helix. From the figure we can say, the system of hard spherocylinders form isotropic (I), nematic (N), smectic A (Sm_A) and solid phases. The triple points I-Sm_A-solid and I-N-Sm_A are found at $L/D = 3.1$ and $L/D = 3.7$, respectively. Monte Carlo simulation techniques like NVT, NPT and variable shape constant volume Monte Carlo are used to equilibrate the system [35] [12].

We plan to follow the similar techniques in order to obtain a phase diagram of hard helices. However, We need to resort to certain special techniques in order to speed up the simulation. This will be explained in detail in chapters 2 and 3. Because of the non-convex shape of hard helices, we need to consider large system sizes and efficient algorithms to reduce the computational cost. Any deviation from this phase diagram helps to draw important conclusions about the effect of a helical shape. Our study of the phase behaviour of hard helices not only tells the effect of helical shape on liquid crystal phases but also introduce new phases ascribable to the helical shape. This might help in understanding experimental results of the fd virus and helical flagella.

1.5 Thesis outline

In this thesis, I first give a brief introduction of Monte Carlo methods that are used in this work in Chapter 2. In Chapter 3 I present results on isotropic to nematic phase transition of hard helical particles. Chapter 4 is dedicated to the isopointal set structural search method which is used to find dense packing of hard helices. In Chapter 5 I introduce the new chiral nematic phase called 'screw nematic' which is particular to helical shape. In Chapter 6 I present full phase diagram of helical particles including high density smectic phases.

Chapter 2

Monte Carlo methods

2.1 Introduction

Calculating the properties of a condensed matter system by solving the equations of motion is not feasible because of the large number of atoms($\approx 10^{23}$) in the system. Bringing the system to thermodynamic equilibrium by allowing the system to interact with surroundings makes the problem even more complex. With the help of statistical mechanics, this problem can be conveniently transferred to calculating the average properties of large enough systems by treating them in a probabilistic way. Any equilibrium property can be obtained by taking the average of the corresponding thermodynamic variable over the microstates collected with the probability density appropriate to the imposed equilibrium conditions.

As an example, let us consider a canonical system of N atoms in a volume V and temperature T. The partition function Z of such system is given by

$$Z = \int dp^N dr^N \exp[-\beta H(\mathbf{r}^N, \mathbf{p}^N)] \tag{2.1}$$

where $\mathbf{r}^N$ denotes the coordinates of all N particles, $\mathbf{p}^N$ denotes corresponding momenta, H is the Hamiltonian of the system and $\beta = \frac{1}{k_B T}$. The probability of finding the system in state i is proportional to the Boltzmann factor $\exp(-\beta H_i)$. The thermal average of any equilibrium property A is given by,

$$\langle A \rangle = \frac{1}{Z} \int dp^N dr^N A(\mathbf{r}^N, \mathbf{p}^N) \exp[-\beta H(\mathbf{r}^N, \mathbf{p}^N)] \tag{2.2}$$

Using thermodynamic relations, other macroscopic equilibrium properties can be obtained. Thus the problem is simplified to that of finding the properties in a given ensemble. An ensemble consists of all microstates of an equilibrium macroscopic system under a particular set of thermodynamic constraints. We define different ensembles depending on the nature of the constraints such as micro-canonical, canonical and grand canonical ensembles.

The important imposition for generating microstates is ergodicity. Macroscopic properties measured in experiments are time averaged quantities. The time scale of the observation is very large when compared to the switching time scale from one microstate to another [36]. Because of this, we can assume that system visits all accessible microstates during the observation time. Hence a macroscopic quantity obtained by taking an average over a suitable ensemble is equivalent to the time averaged quantity [37] [38]. In order to ensure that the system is in equilibrium, the sampling of microstates should obey a condition termed “detailed balance", which requires that the forward and backward rates of any transition between states are equal.

Construction of equilibrium ensembles by generating microstates according to the Hamiltonian of the system is viable by computer simulation. Monte Carlo (MC) and Molecular Dynamics (MD) are the two popular and powerful methodologies followed in computer simulations. Using MD, one can construct an equilibrium ensemble by solving Newton’s equations of motion numerically. On the other hand MC methods ignore the dynamics and kinetics of the system, and simply attempt to accurately sample the microstates of an ensemble by making a random change in the system with probabilities carefully chosen to give reliable average thermodynamic properties. In the present work, we employ Monte Carlo techniques in different ensembles like canonical ensemble (NVT), isothermal-isobaric ensemble (NPT) and grand canonical ensemble (μ,V,T) to study the phase behaviour of the hard helices. In this chapter, I briefly explain Monte Carlo simulation in all three ensembles.

2.2 Importance sampling

To sample efficiently, we need to collect large number of microstates representative of the thermodynamic ensemble. Simple MC moves may result in poor sampling of microstates, increasing the variance. Estimates from any finite sample risk suffering from poor statistics, and the uncertainty in the results is directly related to the variance of the sample observed. Importance sampling is one of the variance reduction techniques and helps to sample points from the region of interest. The probability of observing a particular system energy depends on two independent measures; one is the abundance

of states with a particular energy, D(E) and the other is the Boltzmann factor, which favours the occupation of lower energy states. For a canonical system, the density of states $D(E)$ increases with energy E and the Boltzmann factor associated with energy E is given by $\exp(-\beta E)$ [39].The resultant probability distribution $P(E)$ is given by

$$P(E) = D(E)\exp(-\beta E) \tag{2.3}$$

Using importance sampling, the microstates are sampled according to probability density $P(E)$. The computer implementation of importance sampling Boltzmann distribution given by 2.3 is known as Metropolis Monte Carlo algorithm [40]. The average of macroscopic quantities in the canonical ensemble are calculated by averaging over the sampled micro states. According to eq. 2.2, one needs to know Z to compute averages, which is not known. Metropolis proposed an elegant method to construct ensembles which requires no knowledge of the partition function.

2.3 Metropolis algorithm

The purpose of the algorithm is to generate a Markov chain of microstates starting from an initial configuration C_0 i.e, $C_0 \rightarrow C_1 \rightarrow C_2.....C_k \rightarrow C_{k+1}.....$ These states are generated by performing a random walk in the configuration space according to the probability distribution. From the initial configuration say C_i having energy E_i, a trial configuration C_t with energy E_t is generated by making a random move in the configuration. This move is accepted or rejected according to the acceptance probability which is proportional to the ratio of probabilities associated with C_i and C_t, $\frac{\exp(-\beta E_t)}{\exp(-\beta E_i)}$. The ratio cancels out the partition function in both numerator and denominator.

Thus the acceptance probability is given by

$$p = \min(1, exp[-\beta(E_t - E_i)]) \tag{2.4}$$

The algorithm proceeds as follows:

• Let C_i be the current configuration with energy E_i
• Generate a trial configuration C_t by making a random move to one of the randomly chosen particles in C_i. Calculate its energu E_t
• If $E_t \leq E_i$ then accept the trial configuration: $C_{i+1} = C_t$
• If $E_t > E_i$, calculate the ratio of Boltzmann weights, $p = exp[-\beta(E_t - E_i)]$

Select a random number ζ. If $\zeta < p$ accept trail configuration: $C_{i+1} = C_t$
else reject the trial configuration and set $C_{i+1} = C_i$.

By iterating over the whole procedure, we can generate a Markov chain. The asymptotic part of the Markov chain consists of configurations that belong to the canonical ensemble.

2.4 Monte Carlo in various ensembles

The first importance sampling MC simulation is implemented on hard disks by Metropolis in 1953. Since then studying atomic and molecular fluids by MC has been an active research area. Solids and dilute fluids can be treated analytically using statistical Mechanics. Where as studying highly correlated dense fluids is very difficult. This is where simulations are useful to study phase transitions in fluids.

The general approach of formulating MC simulation in any ensemble of interest consists of the three steps.
i. Determining the microstate probability distribution for the ensemble of interest
ii. Determining the set of MC moves accomplishing changes in all fluctuating quatities.
iii. Imposing the detailed balance condition to find the acceptance criterion

2.4.1 Canonical Monte Carlo simulation (NVT MC)

Implementation of the Metropolis algorithm in canonical ensemble(NVT) is described in section 2.3. But in order to get the equation of state, we need to know pressure. It is not straight forward to obtain pressure from NVT MC since this is an intensive variable. However, using virial theorem, one can obtain the value of pressure.

$$P^* = \rho k_B T + \frac{1}{3V} \left\langle \sum_{i<j} f(\overrightarrow{r}_i - \overrightarrow{r}_j).(\overrightarrow{r}_i - \overrightarrow{r}_j) \right\rangle \tag{2.5}$$

where as ρ is the number density, $f(\mathbf{r}_i - \mathbf{r}_j)$ is the force between the particles i and j. Forces can be easily calculated for continuous and pair wise interactions as the force is directly related to the derivative of the potential. So the virial theorem can be re-expressed in terms of pair correlation function.

$$P^* = \rho k_B T - \frac{2}{3}\pi\rho^2 \int_0^\infty drr^3 \frac{du(r)}{dr} g(r) \tag{2.6}$$

However, this expression does not work for discontinuous potentials like the hard core potential which is in the form of

$$u(r) = \infty, r < r_0$$
$$u(r) = 0, r > r_0$$

We need to use other techniques like NPT MC to study phase transitions of such systems.

2.4.2 Isothermal-isobaric Monte Carlo simulation (NPT MC)

Isothermal-isobaric Monte Carlo simulations were first described by W. W. Wood [41]. He explained this in the context of hard disks. McDonald was the first to apply NPT MC on Lennard-Jones mixture [42]. Isothermal isobaric ensemble is widely used in MC because most of the experiments are done at controlled pressure and temperature. Constant NPT MC simulations are used to find equation of state for the systems where virial expression for pressure cannot be calculated. To study fluid-solid transitions or to study transitions between mesophases like liquid crystals, NPT MC is very useful. These systems exhibit first order phase transitions showing a jump in the first derivatives of thermodynamic variables. By choosing volume as the extensive variable, there is a risk that system might fall into a forbidden region, where it is not able to access any of the coexisting phases. Where as at constant pressure, the system is completely free to find the lowest free energy state. So NPT MC is the convenient technique to simulate systems in the vicinity of first order transitions.

To derive the partition function for the canonical ensemble, we assume that our system with constant N, V and T is in contact with a large heat bath. This thermal contact between the system and a reservoir allow system to have energy fluctuations at constant T. Thus we obtain the Boltzmann factor. To derive the partition partition function in the isothermal-isobaric ensemble, the system is considered to be in thermal contact with heat bath and mechanically coupled with a volume bath. The mechanical coupling allows the system to change its volume in order to keep its pressure constant. So the heat bath acts a thermostat and volume bath acts as barostat.

Since the volume of the box changes, it is convenient to express the coordinates r^N in scaled units of box length L, s^N. The partition function in the NPT ensemble is given by,

$$Q(N,P,T) = \frac{\beta P}{\Lambda^{3N} N} \int dV V^N \exp(-\beta PV) \int ds^N \exp[-\beta H(s^N;L)] \tag{2.7}$$

The free energy associated with the NPT ensemble is the Gibbs free energy

$$G = -k_B T ln(N,P,T) \tag{2.8}$$

Volume is an additional degree of freedom in NPT ensemble. Including volume to the probability distribution

$$\begin{aligned} N(V;s^N) \propto & V^N \exp(-\beta PV) \exp[-\beta H(s^N;V)] \\ = & \exp -\beta[H(s^N;V) + PV - N\beta^{-1} \log V] \end{aligned}$$

This new Boltzmann factor can be used to formulate an acceptance rule for MC trial move from an old configuration 'o' to new configuration 'n'. This involves a simple volume change V to $V' = V + \Delta V$, where ΔV is randomly chosen from $[-\Delta V_{max}, \Delta V_{max}]$

$$acc(o \to n) = \min(1, \exp -\beta[H(s^N;V') - H(s^N;V) + P(V - V') - N\beta^{-1} \ln(V'/V)]) \tag{2.9}$$

The volume trial move can be performed by changing the logarithm of the volume instead of direct volume, from $\log V$ to $\log V + \Delta(\log V)$ [43]. In this case, the integral of V^N over dV is changed to an integral of V^{N+1} over $d \log V$. In the acceptance rule, N is changed to (N+1).

Algorithm:

- Let C_i be the current configuration with energy E_i and volume V_i
- Generate a random number ζ in between 1 and (N+1)
- If $\zeta \leq$ N generate trial configuration C_t by making a random move to one of the randomly chosen particles in C_i. Calculate its energy E_t

else if ζ = N+1 generate trial configuration C_t by performing volume move. Calculate its energy E_t

- If $E_t \leq E_i$ then accept the trial configuration: $C_{i+1} = C_t$
- If $E_t > E_i$, calculate the ratio of Boltzmann weights,

$$p = \exp -\beta(E_t - E_i) + P(V_t - V_i) - (N+1)\frac{\log(V_t/V_i)}{\beta} \tag{2.10}$$

Select a random number ζ. If $\zeta < p$ accept trail configuration: $C_{i+1} = C_t$ else reject the trial configuration and set $C_{i+1} = C_i$.

2.5 Details of the MC simulation of hard helices

This work deals with hard helical particles. All the particles are represented by their center of mass coordinates. To overcome the finite size effect, care has to be taken in choosing the number of particles in the simulation box. The simulation of hard spherocylinders require number of particles ≈ 500 to give correct results. Due to the non-convexity in shape, we need to consider more than 500 particle. The number of particles considered in the simulation is in the range of 900 to 2000. Instead of using euler angles (ϕ, θ, ψ), I used quaternions to represent the orientation of the molecule. This is because of the ease in the implementation of rotational moves using quaternions [35] [44]. Using euler angles, the rotational operations are expressed in terms of trigonometric functions which are very time consuming. We can avoid trigonometric equations if we deal with quaternions. A quaternion can be defined as the unit vector in four dimensional space $Q \equiv (q_0, q_1, q_2, q_3)$ with $q_0^2 + q_1^2 + q_2^2 + q_3^2 = 1$. Quaternion offers an efficient way to generate uniform random vector on four dimensional unit sphere [45]. However, result does not depend up on the representation of rotation. The one-to-one correspondence between the two representations is given by

$$\begin{aligned}
q0 &= \cos\left(\frac{\theta}{2}\right)\cos\left(\frac{\phi+\psi}{2}\right)\\
q1 &= \sin\left(\frac{\theta}{2}\right)\cos\left(\frac{\phi-\psi}{2}\right)\\
q2 &= \sin\left(\frac{\theta}{2}\right)\sin\left(\frac{\phi-\psi}{2}\right)\\
q3 &= \cos\left(\frac{\theta}{2}\right)\sin\left(\frac{\phi+\psi}{2}\right)
\end{aligned}$$

and the rotation matrix defining the rotation is given by

$$\begin{pmatrix} q_0^2+q_1^2-q_2^2-q_3^2 & 2(q_1q_2-q_0q_3) & 2(q_1q_3+q_0q_2) \\ 2(q_1q_2+q_0q_3) & q_0^2-q_1^2+q_2^2-q_3^2 & 2(q_2q_3-q_0q_1) \\ 2(q_1q_3-q_0q_2) & 2(q_2q_3+q_0q_1) & q_0^2-q_1^2-q_2^2+q_3^2 \end{pmatrix}$$

The only interactions involved in the system are hard-core interactions. Thus entropy alone plays a major role in forming stable phases. The hard-core potential is given by

$$U(R) = \infty, R < D$$
$$U(R) = 0, R > D$$

where D is the diameter of the bead forming helix (see model of the helix in chapter 3). Simulations with hard particles consume more computational time compared those with soft particles. This is because of the overlap check for each pair of particles. In hard helical particles, the distance between two helical particles cannot be less than the diameter of the sphere. And the overlap check in such non-convex particles need some tricky algorithms to reduce the computer time in overlap testing. The overlap test in hard helices is explained in chapter 3. Normal periodic boundary conditions are used in the entire work.

Chapter 3

Isotropic to nematic phase transition of hard helical particles

3.1 Introduction

Dating back to van der Waals, a common notion in liquid structure theory held that when the liquid is far away from its critical point, the density is determined by the attractive part of the potential and the structure by the repulsive part [46]. For this reason, the system of hard spheres has been important as a reference system to study the structural properties of simple liquid [47] [48] [49]. The fluid to crystal transition in a system of hard spheres is the first example of an entropy driven phase transition. This finding showed that attractive interactions are unnecessary to study long-range transitions.

In 1949, Onsager[50] paved the way for an entirely new field through his theoretical prediction of isotropic to nematic transition in the case of hard slender rods. However the nematic phase was observed in the suspensions of inorganic biological rod-like particles in 1925 [51] [52]. Original Onsager theory is based on the virial exansion of the free energy truncated at the second virial coefficient. Thus the applicability of the original theory is limited to very long rods. Recently, several improvements have been made to include higher order contributions to the original theory [50] [53] [54]. This motivated studies on many monodisperse or polydisperse systems (heterogeneous or homogeneous) using a series of computer simulations [55] [13] and a number of DFT approaches. All these studies confirm that the entropy alone is enough to bring order in the system.

We recall the biomolecules introduced in chapter1– polynucleotides, polypeptides and virus form nematic or chiral nematic liquid crystal phases at high concentrations. An experimentally favoured rod-like colloidal suspension is the filamentous fd virus particles.

Though they are helical in shape and have chiral symmetry, they are often approximated to rods while interpreting their liquid crystal phases. This is due to the similarity in the shape anisotropy and non-availability of theoretical studies or numerical simulations on hard helical shapes. Experimental studies on the isotropic to nematic transition of filamentous viruses are compared to theoretical studies of rods taking charge and semi-flexibility into account [30] [33]. The onsager treatment and the technical details of the experiments on fd virus are clearly explained in Ref. [33]. At low ionic strength $\approx 1mM$, the effective diameter D_{eff} of virus is large ≈ 60 and thus aspect ratio is small $L/D_{eff} \approx 15$. At such conditions Onsager theory is not in agreement with experimental results and predicts lower coexistence concentrations. At higher ionic strengths $\approx 100mM$ where the particles are long enough $L/D_{eff} \approx 83$, Onsager theory is in quantitative agreement with experiments. All these observations have inspired the investigation of the isotropic-nematic transition of hard helical particles. This chapter mainly focusses on the isotropic-nematic transition of different geometries of helix– from slender rods to curlier helices [56]. These results might help in understanding the differences in theory and experiments observed in fd viruses.

Hard helices are chiral in shape and expected to form chiral mesophases. The pitch of the chiral nematic phase is known to be orders of magnitude larger than the length of the particle. For example, B-DNA (B-form double helix) length $\approx 50nm$ and the pitch of the chiral nematic $P \approx 2.8\mu m$. It is not possible to simulate such large systems. However the chiral nematic phase locally behaves as nematic. In numerical simulations, the nematic phase seen could be a chiral nematic phase in macroscopic scale.

In this chapter I introduce the model of the helix used to study the phase behaviour of hard helical particles. In subsequent sections, focus is laid on the description of the isotropic to nematic transition and details of NPT MC simulation carried out to study this transition in hard helical particles. In the results and discussion section, I discuss about the effect of helical parameters on the isotropic to nematic transition and the differences with corresponding spherocylinder phase diagram.

3.2 Model of the helix

The model of helical particles used in this work is a chain of 15 partially fused hard spherical beads, each of diameter D, rigidly arranged in a helical fashion as shown in Figure 3.1. All lengths in this work are expressed in the units of D. To ensure overlap of the beads, the contour length L of the chain is set to a value less than $15D$. In this work, L is fixed to $10D$. The number of beads and this contour length are chosen such that the particles are long enough to show liquid crystal behaviour. The fusion of the beads

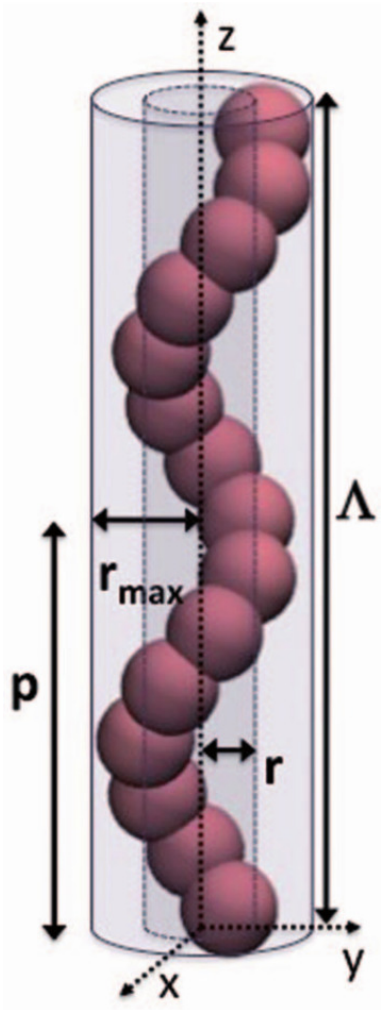

FIGURE 3.1: Model helix made up of 15 partially fused hard spheres of diameter D with $\Lambda = z_{15} - z_1$. r_{max} being $2r+D$ and p is the distance along z axis in making one complete turn.

is considered to make the helix more continuous by reducing the void spaces between the spheres. The centres of the beads are defined by the following helix parametric equations

$$\begin{aligned} x_i =& r\cos(2\pi t_i) \\ y_i =& r\sin(2\pi t_i), \qquad 1 \leq i \leq 15 \\ z_i =& pt_i \end{aligned}$$

where r is the radius of the helix and p is the pitch of the helix. As shown in the Figure 3.1, the centres of the beads lie on an inner cylinder of radius r. The diameter of the outer cylinder $(2r + D)$ is the width of the helix. The long axis of the helix $\hat{\mathbf{u}}$ passes through

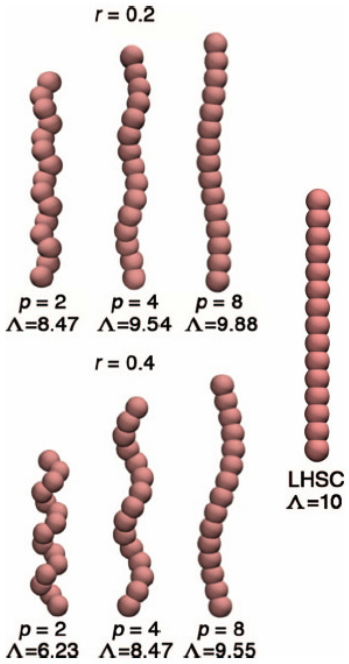

FIGURE 3.2: Shapes with different r and p. For comparison a fully extended Linear hard sphere chain(LHSC) is shown

the center of the helix. Given the values of r, p and L, the increment $\Delta t = t_{i+1} - t_i$ is determined by the following equation

$$\frac{L}{14} = 2\pi\Delta t\sqrt{r^2 + \left(\frac{p}{2\pi}\right)^2} \tag{3.1}$$

The parameteric equations can also be written taking number of turns as the fixed value instead of fixed L [ref. Appendix A]. The euclidean length Λ is measured as the component parallel to the long axis of the helix of the distance between first and last bead. Different helix shapes can be achieved by varying r and p. In this work, different shapes – from a slender rod to a highly coiled helix – are studied by considering different values of r and p. Figure 3.2 show different shapes of helices and their respective r, p and Λ values. A long hard sphere chain (LHSC) shown in the figure is considered a reference of rod-like shape. We investigate how sensitive phase structures and phase behaviour are to the curliness of the helix defined by the helical parameters (r and p).

3.3 Isotropic to nematic phase transition (IN)

As discussed in chapter 1, the nematic phase is characterized by the long range orientational order and short range positional ordering. To favour orientational ordering, the particles should be sufficiently anisotropic and the concentration of the system high. All

the particles are aligned into a single preferred direction while their centres are randomly distributed. The average local orientation of the particles is described as nematic director and is denoted by a unit vector $\hat{\mathbf{n}}$. Helices are rotationally invariant about their C_2 axis passing through the centre and perpendicular to the long axis of helix $\hat{\mathbf{u}}$, so there is no physical difference between particles aligned in the up and down directions i.e., $\hat{\mathbf{u}}$ and $-\hat{\mathbf{u}}$. Similarly, the average physical properties of the nematic phase are not altered upon the inversion of the sign of $\hat{n}$ though the inversion does not allow the exact mapping of the particles. If one of the perpendicular axes to $\hat{\mathbf{n}}$ is taken as a reference, in the nematic phase, C_2 axes of individual helices are randomly oriented. However at higher densities, we see a different picture which arises due to the details of helix shape. I discuss about those phases in the chapters 5 and 6.

Onsager theory explains the first order transition of the IN transition of long thin rods considering only steric interactions. Theory demonstrates that the density driven isotropic - nematic transition is because of entropy gain induced by excluded volume effect. The stability of nematic phase can be explained as the result of the trade-off between the orientational entropy and translational entropy. Rotational entropy is maximum when rods orient in all possible orientations with equal probability. Translational entropy is maximum when rods have maximum free volume to move in. This occurs when all rods orient in one direction. At low densities, rotational entropy dominates resulting in a stable isotropic phase and at high densities translational entropy dominates stabilising the nematic phase. Parson and Lee incorporated higher virial coefficients in an approximate model which is useful for short molecules [53] [54]. Maier Saupe theory gives the mean field description of the isotropic-nematic transition by considering each molecule to be placed in the mean field of all others [57]. Landau-de-Gennes theory of the isotropic-nematic transition is done by expanding free energy in powers of order parameters and required few phenomenological parameters which can be fitted with the experiment [6].

An extension of Onsager theory was applied to study isotropic-nematic transition of hard rods having finite aspect ratios by taking higher order virial terms into account [53] [54]. The similar extension of Onsager theory i.e., Onsager theory coupled with Parson Lee (PL) and Modified Parson Lee (MPL) approximations is applied to study isotropic-nematic transition of hard helical particles with finite aspect ratios by Elisa Frezza and Alberta Ferrarini. The performance of this theory has been tested by comparing with the Monte Carlo simulations. We present an evidence that helical shape effects the location of isotropic-nematic transition through theory and simulation. The results obtained cast doubt on providing a direct link between the phase diagram of hard spherocylinders and that of hard helices.

3.3.1 Nematic order parameter $\langle P_2 \rangle$

The orientational symmetry of simple nematic phase is described by a scalar order parameter, which is zero in isotropic phase and nonzero in the nematic phase. Considering rods, having cylindrical symmetry about their long axis, the orientational order parameters can be defined as the expansion coefficients of the orientational distribution function $f(\Omega)$; $\Omega = (\theta, \phi)$, where θ and ϕ are the polar angles of the long axis of the particle . Since the distribution function is invariant under the rotation about the nematic director, it can be expanded in a wigner series(in a basis of Wigner rotation matrices) [39]:

$$f(\Omega) = \sum f_{lmn} D^{l}_{m,n}(\Omega). \tag{3.2}$$

If the nematic director is chosen as the z-axis, the m value becomes zero. Because of the cylindrical symmetry, rotation about the long axis does not change the distribution, which implies n = 0 and f depends only on θ, the angle between the director and the long axis of the rod. Because of the symmetry in the plane perpendicular to the nematic director, only terms with even l can appear. The oreintational order parameters are linear expansion coefficients in eq 3.2 and are given by

$$\bar{D}^{l^*}_{0,0} = \int d\Omega f(\Omega) D^{l^*}_{0,0}(\Omega). \tag{3.3}$$

The D-matrix elements with second index equal to zero are proportional to spherical harmonics and associated Legendre polynomials:

$$\bar{D}^{l^*}_{0,0}(\equiv \langle P_l \rangle) = \int d\Omega f(\Omega) P_l(\cos\theta). \tag{3.4}$$

The $\langle P_l \rangle$ is the ensemble average of even Legendre polynomials. $\langle P_2 \rangle$ is the simplest orientational order parameter sufficient to measure nematic ordering and is given

$$\begin{aligned}\langle P2(\cos\theta)\rangle =& \langle \frac{3}{2}\cos(\theta)^2 - \frac{1}{2}\rangle \\ =& \frac{1}{N}\sum_{i=1}^{N} \frac{3}{2}(\hat{n}.\hat{u}_i)^2 - 1\end{aligned}$$

Several experimental techniques measure the nematic order using this equation. It is not possible to implement $\langle P2(\cos\theta)\rangle$ directly in simulations as it involves the prior

knowledge of $\hat{n}$. It is more convenient to characterize using second rank ordering tensor Q.

$$Q_{\alpha\beta} = \frac{1}{N}\sum_{i=1}^{N}\frac{3}{2}\left(u_i^{\alpha}u_i^{\beta} - \frac{\delta_{\alpha\beta}}{2}\right) \tag{3.5}$$

where $\alpha, \beta \epsilon x, y, z$ indices referring to the laboratory frame, u_i^{α} is the component of the unit vector of particle i along α. The Q- matrix is symmetric, tracless and second rank tensor. The three eigenvalues $\lambda_1, \lambda_2, \lambda_3$ of Q-matrix are a measure of nematic order in the three orthogonal directions defined by the corresponding eigenvectors. In case of the uniaxial nematics, $-2\lambda_1 = -2\lambda_2 = \lambda_3$. The maximum eigenvalue λ_3 is the nematic order parameter $\langle P_2 \rangle$ and corresponding eigenvector is the nematic director $\hat{n}$.

One can raise the question of the uniaxiality of the nematic phase shown by helical particles as the shape lacks cylindrical symmetry about the long axis. From the eigenvalues of the Q matrix, obtained for the system of helical particles we confirm the uniaxial nature. The difference between the λ_1 and λ_2 eigenvalues of Q was found to be smaller than 5%, in agreement with our assumption of uniaxial nematic order. This means in conventional nematic phase, the helices are still free to rotate about its long axis.

3.4 NPT Monte Carlo Simulation details

Each helix is represented by its centre (the centre on the long axis of the helix) and a quaternion defining the orientation of the helix. Isothermal-Isobaric(NPT) MC simulations were carried out using $N = 900$ to 2000 particles in a box with a triclinic shape with standard periodic boundary conditions. This means the simulation box has the freedom to change its shape by changing its side lengths and the angles between the sides. Each Monte Carlo cycle consists of $N/2$ translational, $N/2$ rotational and one volume move. Volume move allows the box size and shape to change. An equilibration run of 3×10^6 MC cycles is implemented followed by a production run of 3×10^6. During the equilibration, the maximum change in displacement, orientation and volume moves are chosen such that $30\% - 40\%$ of moves are accepted. while in the production run these values are fixed to avoid any possible violation of the detailed balance condition. Simulations were either started from a dilute initial configuration or from a compact configuration generated from ISSM which is discussed in Chapter 4.

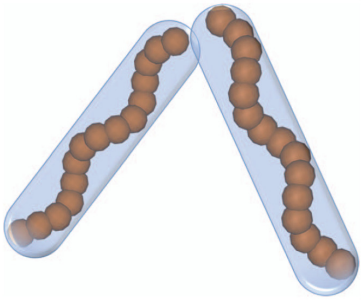

FIGURE 3.3: Cartoon of the overlap between the spherocylinders containing a pair of helices

3.4.1 Overlap Check

The main problem in the simulation of non-convex hard bodies is the computer time invested in checking the overlap. In NPT MC, each volume move consists of N^2 overlap checks and each translational or rotational move consists of N overlap checks. In view of the computation time, simulations of hard helices are more demanding than the simulation of hard spherocylinders. Depending on the state point and the helical parameters considered, the computational cost is as high as 8 times that of the spherocylinder. Also, the non-convex shape demands large numbers of particles in the system to avoid finite system size effect.

The overlap check in the current helix model can be reduced to the overlap check in beads forming helices. But checking for the overlaps in a system containing $N \times 15$ spheres will make the test again computationally expensive.

To save computer time, an overlap check between a pair of helices is done in three levels [Appendix B]. Checking goes to the next level only if there is an overlap in the previous level.

i) Overlap check between the spheres containing the whole helix
ii)Overlap check between the spherocylinders containing helix.
iii)Bead to bead overlap check for the pair of helices.

Figure 3.3 shows the cartoon of the pair of spherocylinders containing helices. This strategy is helpful in reducing the computer time by a factor of 5. The overlap test in spherocylinders is done by following the algorithm proposed by Lago and Vega [58]. This method is based on the idea of finding the minimum distance between two line segments. The number of regions to be searched for the closest approach is reduced to four depending on the angle between the line segments. This test is relatively fast compared to the methods used before.

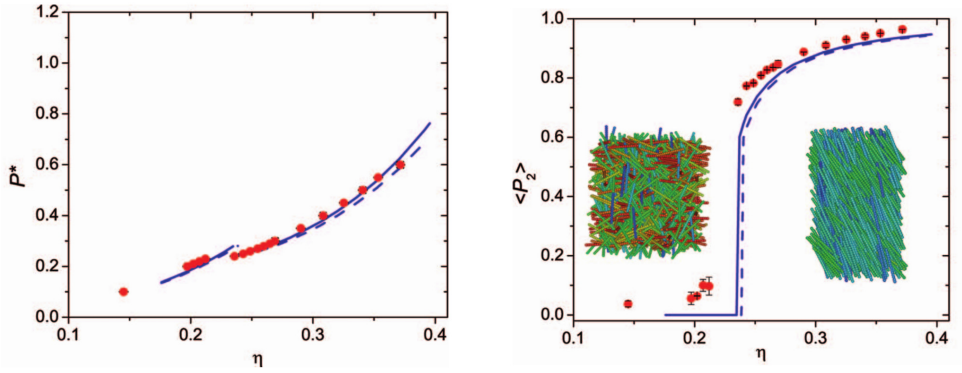

FIGURE 3.4: Pressure(P^*) as a function of volume fraction (left) η and $\langle P_2 \rangle$(right) as a function of η (right) for LHSC. Results from MC simulations are shown in closed circles and from Onsager theory with PL(dashed line) or MPL(solid line) approximation. Insets on the right panel are representative snapshots for Isotropic and Nematic phases obtained by using QMGA software

3.5 Results and Discussion

We have investigated the IN transition of helical particles with different helix structural parameters (i.e., r and p) using NPT MC simulations. Results are presented in reduced units, with D taken as the unit of length, and reduced pressure $P^* = PD^3/k_BT$. This work was done in collaboration with Elisa Frezza, Alberta Ferrarini and Giorgio Cinacchi. Monte Carlo results are compared with the results obtained from Onsager theory with PL and MPL approximations carried out by Elisa Frezza and Alberta Ferrarini. Monte Carlo results are presented with error bars, evaluated according to reblocking algorithm [59].

A preliminary test is performed for Linear hard sphere chain (LHSC) shown in figure 3.2 for which $\Lambda = L$. Figure 3.4 shows the $\langle P_2 \rangle$ and P^* as a function of the packing fraction. The solid line in the figure corresponds to the results from Onsager theory with PL approximation and the dashed line with MPL approximations. The red dots are from NPT Monte Carlo simulations.

From figure 3.4, we see an IN phase transition at $\eta \approx 0.24$, characterized by a jump in the order parameter. $\langle P_2 \rangle$ takes values greater than 0.8 in the deep nematic region.The non- zero $\langle P_2 \rangle$ values obtained in the isotropic region are due to the finite size effects in the simulation. Figure 3.4 shows a good agreement between theory and simulations for LHSCs. The results obtained using PL and MPL are very close to one another. This agrees with [60] where it is shown that for LHSCs the discrepancies between MC simulations and PL theory, and correspondingly also the improvements of the MPL scaling decreases as the superimposition between adjacent spheres increases.

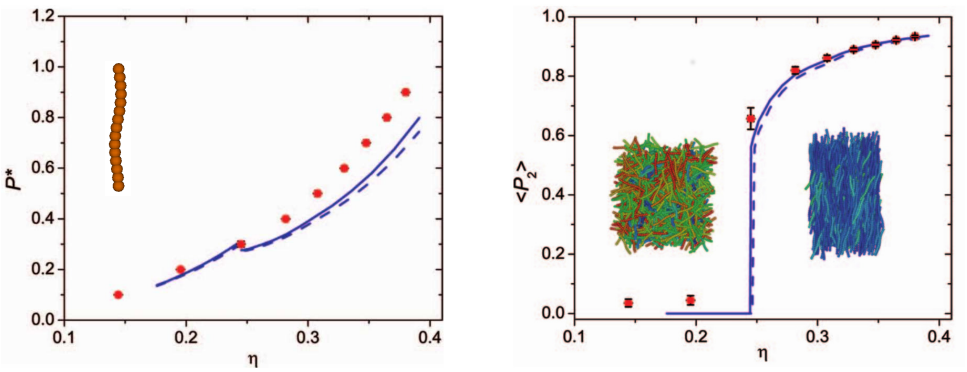

FIGURE 3.5: Pressure(P^*) as a function of volume fraction η (left) and $\langle P_2 \rangle$(right) as a function of η (right) for helix with $r = 0.2$, $p = 8$. Results from MC simulations are shown in closed circles and from Onsager theory with PL(dashed line) or MPL(solid line) approximation.

Figures 3.5 to 3.7 show $\langle P_2 \rangle$ and equation of state curves for the helices with r = 0.2 and decreasing pitches p = 8, 4 and 2. Decrease in pitch increase the curliness of helix. So we expect the discrepancies with respect to LHSCs are more pronounced with decreasing pitch. In all these cases an IN transition is occurring with the transition shifting towards higher densities with decreasing pitch. This effect can be qualitatively understood in terms of a decrease in euclidean length of the helix (and hence the aspect ratio $(\Lambda + D)/(2r + D)))$ with the decrease in pitch. The choice of the aspect ratio is discussed in the section 3.5.1. The values of aspect ratio are 7.77, 7.52 and 6.76 for helices with $r = 0.2$ and $p = 8$, 4 and 2 respectively.

From the equation of states, we can notice that the pressure is underestimated by theory. This can seen from the equation of state curves. The differences between theory and simulation increase with increasing density and decreasing pitch. From order parameter curves, it appears like an IN transition occurrs at lower a volume fraction for curlier helices. The decrepancies are even more pronounced for helices with $r = 0.4$. Because an increase in radius increases the curliness of the helix. These results could probably give some idea about the differences observed in the location of the IN transiton of fd virus when compared to Onsager theory [30].

The MPL variant gives slight improvement over the PL approximation. This deviation suggests the need for a better theory to account for real excluded volume. This discrepancy increases with the increase in the radius of the helix. Theory predicts well for those helices which are elongated and rod like.

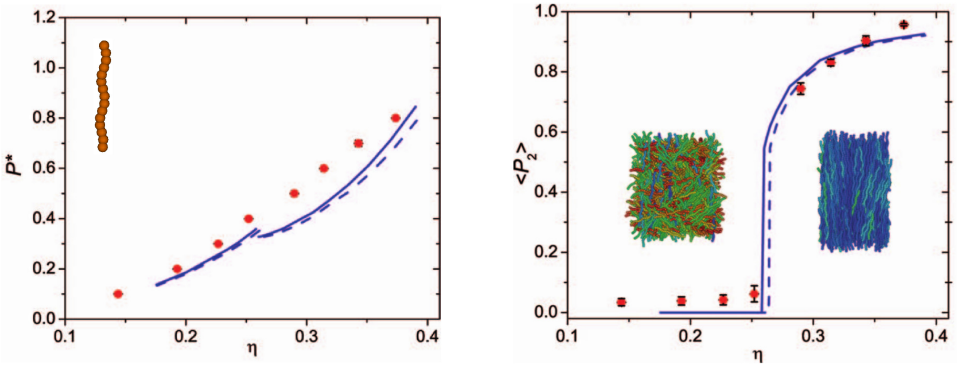

FIGURE 3.6: Pressure(P^*) as a function of volume fraction η (left) and $\langle P_2 \rangle$(right) as a function of η (right) for helix with $r = 0.2$, $p = 4$. Results from MC simulations are shown in closed circles and from Onsager theory with PL(dashed line) or MPL(solid line) approximation.

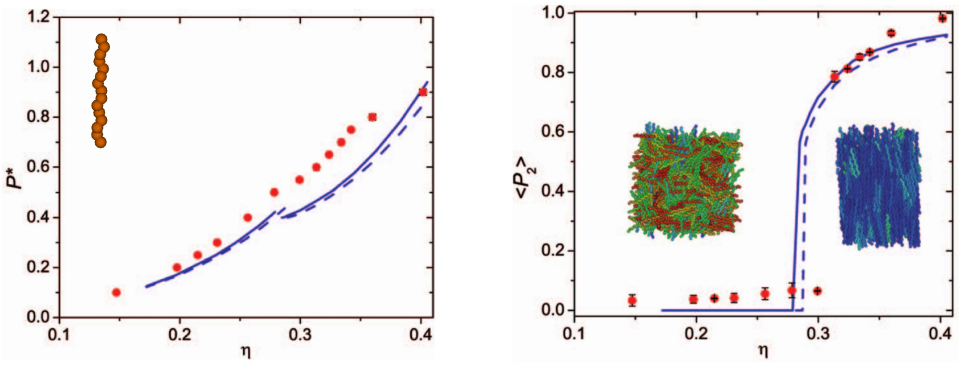

FIGURE 3.7: Pressure(P^*) as a function of volume fraction *eta* and $\langle P_2 \rangle$(right) as a function of *eta* (right) for helix with $r = 0.2$, $p = 2$. Results from MC simulations are shown in closed circles and from Onsager theory with PL(dashed line) or MPL(solid line) approximation.

3.5.1 Defining an aspect ratio for helix?

An interesting point related to the above findings is whether the IN transition for helices can be mapped on to the that of rods in terms of simple parameters such as the aspect ratio, as generally done in experimental work on helical systems. Like spherocylinders, the contour length L, which is identical for all the helices is not a significant parameter. On the other hand, euclidean length Λ, although more meaningful is not fully satisfactory either, since for the same aspect ratio Λ/D, the density at which the IN transition occurs has a non-trivial dependence on the combination of the helical parameters r and p. The better approximant for the aspect ratio can be obtained by considering the total width of the helix ($2r$+D) instead of D i.e., $(\Lambda + D)/(2r + D)$. As a general rule, we find the transition to move towards higher volume fraction with increasing degree of non-convexity.

Figure 3.8 shows the IN transitions signalled by a jump in $\langle P_2 \rangle$ in case of $r = 0.3$ and

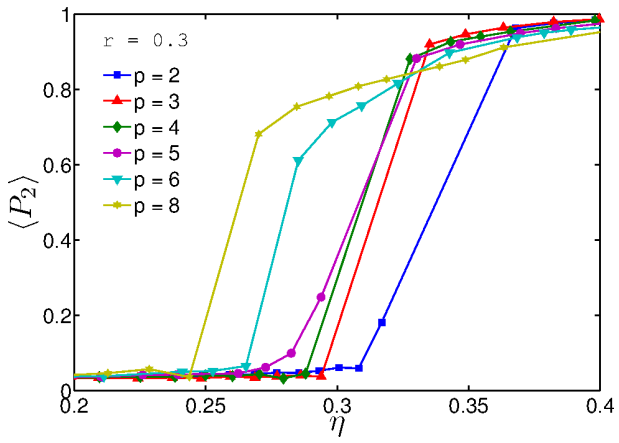

FIGURE 3.8: Figure showing $\langle P_2 \rangle$ order parameter for helices with radius 0.3 and different pitches

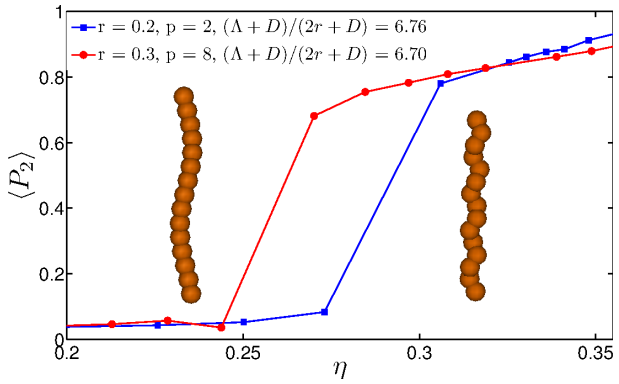

FIGURE 3.9: helices with nearly same aspect ratios with different locations of IN transition

different pitch values. With increase in the pitch, the location of IN transition moves towards lower densities. This is a direct consequence of an increase in the euclidean length with increase in pitch.

Two helices having similar aspect ratios ($(\Lambda + D)/(2r + D)$) are studied using NPT MC simulation. Figure 3.9 shows that the location of the IN transition is different for two helices having similar aspect ratios. The helix with higher aspect ratio is actually showing IN transition at higher density which is not usual. This result betrays an ambiguity in defining an aspect ratio of helices. The fact that the location of an IN transition is not uniquely related to the aspect ratio may have implications for the analysis of experimental data for helical particles as anticipated.

3.5.2 Conclusions

Systems of hard helices were investigated using NPT Monte carlo and variations of Onsager theory. Our main goal was to rationalize the changes in the isotropic to nematic

phase transition on going from straight rod-like to quite tortuous helical particles. We have found that helicity affects the location of the IN transitions, with the latter in general being shifted to higher densities with increasing aspect ratios, as is the case for spherocylinders. However the same aspect ratio can be achieved with different structural parameters of hard helices, and this affects the IN transition. In other words, the aspect ratio cannot be a good candidate for the interpretation of liquid-crystal phase diagram of strongly curled helical particles. We have found that for high helicities Onsager theory significantly departs from the numerical simulations, even when a modified from of Parson-Lee rescaling is included to account for the non-convexity of particles. When compared to MC data, Onsager theory generally underestimates pressure, with deviations that increase with increasing density and upon transition from the isotropic to the nematic phase. This points to the need of more effective theory for hard non-convex particles, a field that remain largely unexplored.

Chapter 4

Packing of helices by Isopointal set Structural Search Method(ISSM)

4.1 Introduction

Recent advances in the synthesis of different colloidal nano-particles with non-spherical shapes and their self assembly into crystal structures makes predicting dense packing an interesting and useful study [61] [62] [63] [64]. Dense packing structures are the most likely stable self assembling structures of colloids. Spherical colloids [49] showing a fluid to crystal transition is an example of an entropically driven crystallization, where configurational entropy is sacrificed for a greater volume per particle in structures that can be compressed to high density . Simulations of hard spheres has given insight into the self assembly of colloids. Examples of non-spherical shaped hard particle simulations include spherocylinder [34], ellipsoids [65], bowl shaped particles, banana shaped particles [66], dumbbells *etc.* In designing such advanced anisotropic particles, it is important to understand the relation between the shape of the particles and its maximum packing density or at least be able to predict the densest crystalline structure for a given particle shape. Different methods have been implemented in predicting crystal structures for various three dimensional (3D) and two dimensional (2D) shapes[61] [62]. But the dense packing of chiral objects like helices is given much less attention in the literature. In this chapter, I discuss the Isopointal set Structural Search Method (ISSM) and its implementation on helical particles to find densest packing. Our aim is to find a relationship between the maximum packing fraction and the helical shape defined by r and p. Since anisotropic particles with high aspect ratio tend to form layered structures at higher densities, this study is done on a single layer of helices with their centres restricted to a plane. This considerably reduces the computational cost of the search, because structural search in

the 17 two dimensional wall paper groups is computationally much cheaper than working in the 230 space groups in 3D.

The other important reason behind the interest in this study is the difficulty arising in the MC simulation of helices in dense phases such as those I will discuss in chapters 5 and 6. Initial conditions must be chosen that allow simulations to span the whole phase diagram, and thus access all phases ergodically. Usually a disordered initial condition is unable to probe the most compact phases. On the other hand, the high density compact configurations of particles of arbitrary shape cannot reliably be envisaged or constructed without a reliable search method.

4.2 Isopointal set Structural search Method(ISSM)

The ISSM was developed by Toby Hudson and Peter Harrowell [67] [68]. They implemented this method to find dense packing structures for binary hard sphere mixtures and dense packing of arbitrary 2D shapes. The idea of the ISSM is to break the whole configuration space of possible crystal structures into finite number of subspaces called isopointal sets where each set can be explored via a good local optimization method such as simulated annealing to find the best packing within it. These isopointal sets are generated by the crystallographic input and symmetry elements present in the system. Thus the search is limited to a few isopointal sets. This reduces the computational cost in two ways. Particles with particular symmetry are incommensurate with some crystal structure symmetries, which limits the number of isopointal sets that must be searched. Within an isopointal set, many particles are symmetrically related to one another, so the search space is parametrized by fewer variables. This idea of selective search works well because the particles in nature prefer to crystallize into fairly symmetric crystals, with symmetry-related particle positions and orientations, in spite of having many possibilities.

4.2.1 Two dimensional search space

4.2.1.1 Wallpaper groups

Wallpaper groups are also called plane symmetry groups or plane crystallographic groups. There are 17 wall paper groups. The classification is done based on symmetries in a repeated pattern in 2D. The symmetries in a plane are translation, rotation, reflection and glide. The 17 wallpaper groups are given the following labels:
p1, pg, pgg, pm, cm, cmm, pmg, pmm, p2, p4, p4m, p3, p3m1, p31m, p6, p6m

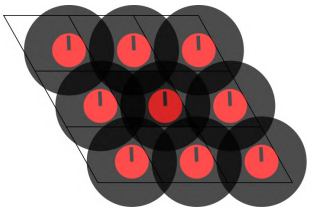

FIGURE 4.1: Optimal two-dimensional packing in wallpaper group p1 of helices with radius 0.3 and pitch 3. The perimeter of the red circle represents the helical radius. The perimeter of the black circle represents the maximum extent of the edge of the beads. The small black line represents the orientation of the C_2 axis.

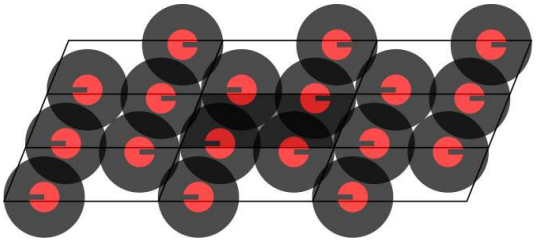

FIGURE 4.2: Wallpaper group p2 for helix with radius 0.3 and pitch 3

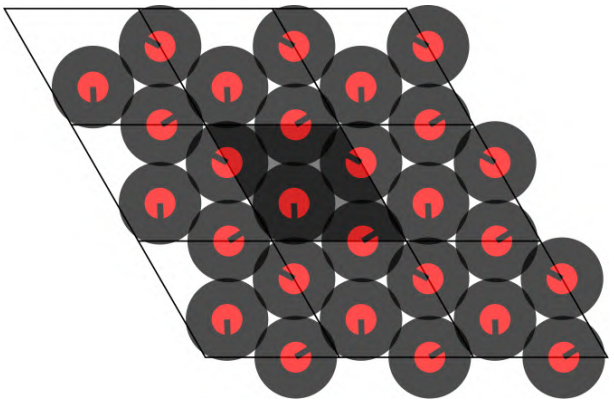

FIGURE 4.3: Wallpaper group p3 for helix with radius 0.3 and pitch 3

This notation gives the information about symmetry elements in the group. The group start with p or c primitive or centred cell. The number n shows n-fold rotational symmetry. The following letters m, g or 1 represent mirror, glide reflection or none respectively. Out of 17 wall paper groups, for a layer consisting solely of right handed helices only 5 wall paper groups are possible. Absence of mirror symmetry and glide symmetries for helix allow only p1, p2, p3, p4 and p6 wall paper groups.

Figures 4.1 to 4.5 show a 3×3 cell arrangement in the five wall paper groups of helix with radius 0.3 pitch 3, where there is only one set of symmetry-related particles, with related orientations and positions. This is a planar representation of the helix showing each helix as circle and its centre as the centre of helix in the plane. The red circle is projection of the outer extremities of the spheres making up the helix. The overlap in the circles is shown by dark grey areas. Here all the particles are hard particles and no overlap

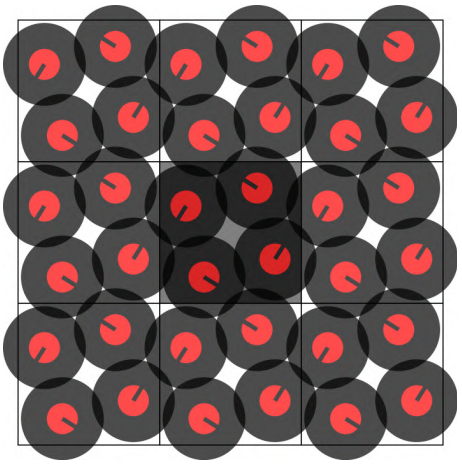

FIGURE 4.4: Wallpaper group p4 for helix with radius 0.3 and pitch 3

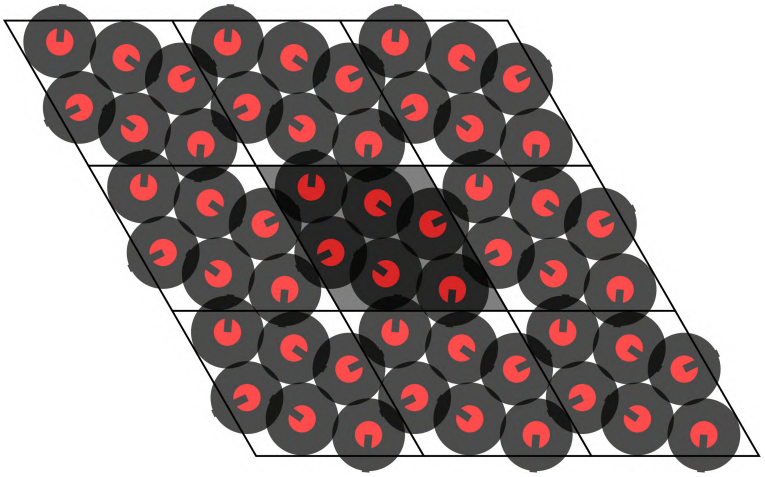

FIGURE 4.5: Wallpaper group p6 for helix with radius 0.3 and pitch 3

is permissible. The apparent overlap in the circles shows the extent of interpenetration of turns of one helix into those of another. The black line at the centre of the circle indicates the orientation of the two fold C_2 symmetry axis of helix. The corresponding three dimensional picture is shown in the figure 4.7. Notice that in figure 4.1, the p1 wall paper group has all particles aligned in the same direction with large interpenetration shown by dark grey areas. In case of no interpenetration, the maximal packing would be the two dimensional hexagonal structure, having $\eta = \frac{\pi}{12} = 0.906$ and with larger circle inscribed in the unit cell of area equal to $\frac{(2r+1)^2\pi}{3}$. Figure 4.6 shows $r = 0$ case with no overlapping.

4.2.1.2 Wyckoff sites

Wyckoff sites are the positions in the unit cell which are not affected by particular symmetry operations of the space group. Positions associated with particularly symmetry

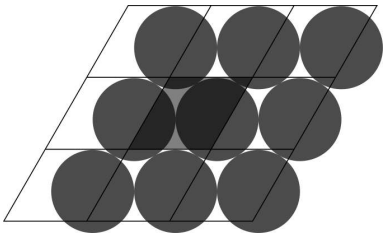

FIGURE 4.6: maximally packed two dimensional structure of helices in the limit case $r = 0$

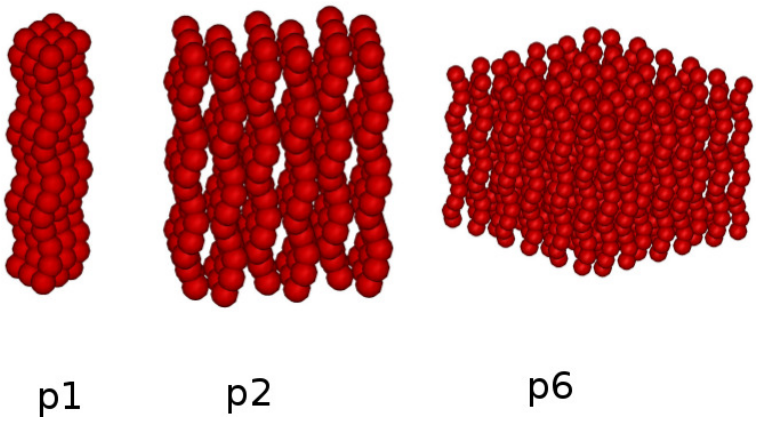

FIGURE 4.7: 3D representation of wall paper groups of helix with radius 0.3 and pitch 3

centres, rotation axes or mirror planes are distinct Wyckoff positions. Any two points which are similarly affected (e.g. are both only on the same mirror plane) will have the same Wyckoff positions. Once a particle is placed on such a site in the cell, there will be a set of associated image particles (collectively called as 'orbit') which map onto one another when the symmetry operations are applied. The number of such positions in the unit cell is called multiplicity of the Wyckoff position.

4.2.1.3 Isopointal sets

All structures within a wallpaper group and with the same occupied Wyckoff sites belong to the same isopointal set. The only things that vary between these structures are the cell lengths, cell angle and the position of one particle in each occupied Wyckoff orbit.

4.3 Implementation of ISSM on helical particles in 2D

Since the number of isopointal sets that we can search is enumerable but unbounded, we limit them by considering only those with a small number of occupied Wyckoff sites, N_{occ}. This approximation is based on the observation that the vast majority of crystalline

materials, and dense packings have a very small number of occupied wyckoff sites. For example 90% of organic crystal structures in the Cambridge Structure Database have $N_{occ} = 1$, and 9% have $N_{occ} = 2$ [69]. We choose to search the sets with the number of Wyckoff sites up to 3. Recall that the isopointal sets that must be searched are further limited by the fact that a right handed helix cannot pack in a space group with a mirror plane, because that would imply the presence of left handed helices. Once the isopointal sets are generated, simulated annealing technique is implemented in each set to find the structure with maximum packing with in the set. For a fixed helical shape, the configurational parameters for a search in 2D are the two unit cell side lengths($cell_x$, $cell_y$), the angle between the sides($cell_\theta$), the fractional coordinates L_x and L_y of each of N_{occ} particles in unit cell and the orientation of each of these particle(L_θ).

Our particular implementation first iterates over the maximum number of Wyckoff sites to be occupied. The second level of the enumeration is to loop through all permissible wallpaper groups. Within each isopointal set a simulated annealing Monte Carlo algorithm is implemented which stochastically varies the parameters like particle coordinates, orientation and cell edges and angle. Moves that cause direct overlap between particles are rejected. The function it seeks to optimize is simply the density of the structure. This density is determined entirely by the shape and number of the particles and the cell volume, provided no overlap. Moves that do not cause overlap are accepted according to the Monte Carlo acceptance criterion where the “energy" of the system has been replaced by the inverse of the density, and a fictitious temperature is gradually decreased through out the simulation. This continues until the particle moves become very small, and the density improvements cease. Simulated annealing within an ergodically-connected space is guaranteed to eventually converge on the global minimum if the search is conducted for long enough and the temperature decrease is slow enough [70].

4.3.1 Algorithm

4.3.2 Simulated annealing technique

The algorithm involves following steps.

1. Initialisation: Generate a random initial configuration ‘o’ in a given isopointal set with no overlapping particles.

2.Random Moves: Generate a new trial configuration ‘n’ by making a random change in one of the configurational parameters for that isopointal set.

3.Acceptance criterion: a. Reject the configuration 'n' if it has any overlaps b. If n does not contain overlap, then i. if $\eta_n \geq \eta_o$, accept the move ii. if $\eta_n < \eta_o$, probabilistically either accept or reject the move based on controlled acceptance probability.

$$P_{acc}(o \rightarrow n) = min\left(1, \exp\left[\frac{\frac{1}{\eta_o} - \frac{1}{\eta_n}}{T^*} + N \ln\left(\frac{\eta_o}{\eta_n}\right)\right]\right) \tag{4.1}$$

where η_i is the packing density of configuration i, T^* is the simulated annealing temperature and N is the number of particles in the unit cell.

4: Iterate: Repeat steps 2 and 3 in a loop for the given number of Monte Carlo cycles

Simulation Temperature T^*

Simulation starts with a temperature(T^*_{start}) and ends with Temperature(T^*_{end}). The annealing scheme determines how the T^* decrease between moves from T^*_{start} to T^*_{end}. The relaxation time increases with the decrease in temperature. To ensure proper equilibration of the system, the cooling rate must be very slow. Previous studies found that an exponential decrease works well compared to a linear decrease in T^* []. In this work,

$$\frac{T^*_{start}}{T^*_{end}} = 200, T*_{mid} = \sqrt{0.00005}, T^*_{start} = 0.1, T^*_{end} = 0.0005 \tag{4.2}$$

and T^* decreases by 0.11% per 100 moves. The exponential decrease allows the system to optimize its packing when T^* is low. These parameters were tested by conducting 10 multiple runs and found that all of them converge on the same structure.

4.4 Shapes studied

From the definition of helix described in chapter 3, a variety of helical shapes are obtained by varying r and p. The ISSM method is implemented on helices with radius ranging from 0.1 to 1.0 with an interval of 0.1 and pitch ranging from 1 to 10 with the interval 1. Figure 4.8 shows all the shapes that are studied using ISSM.

4.5 Overlap detection

A chiral object such as helix is not symmetric about its long axis. Through out the implementation of ISSM in 2D, care has to be taken with the rotation move in the

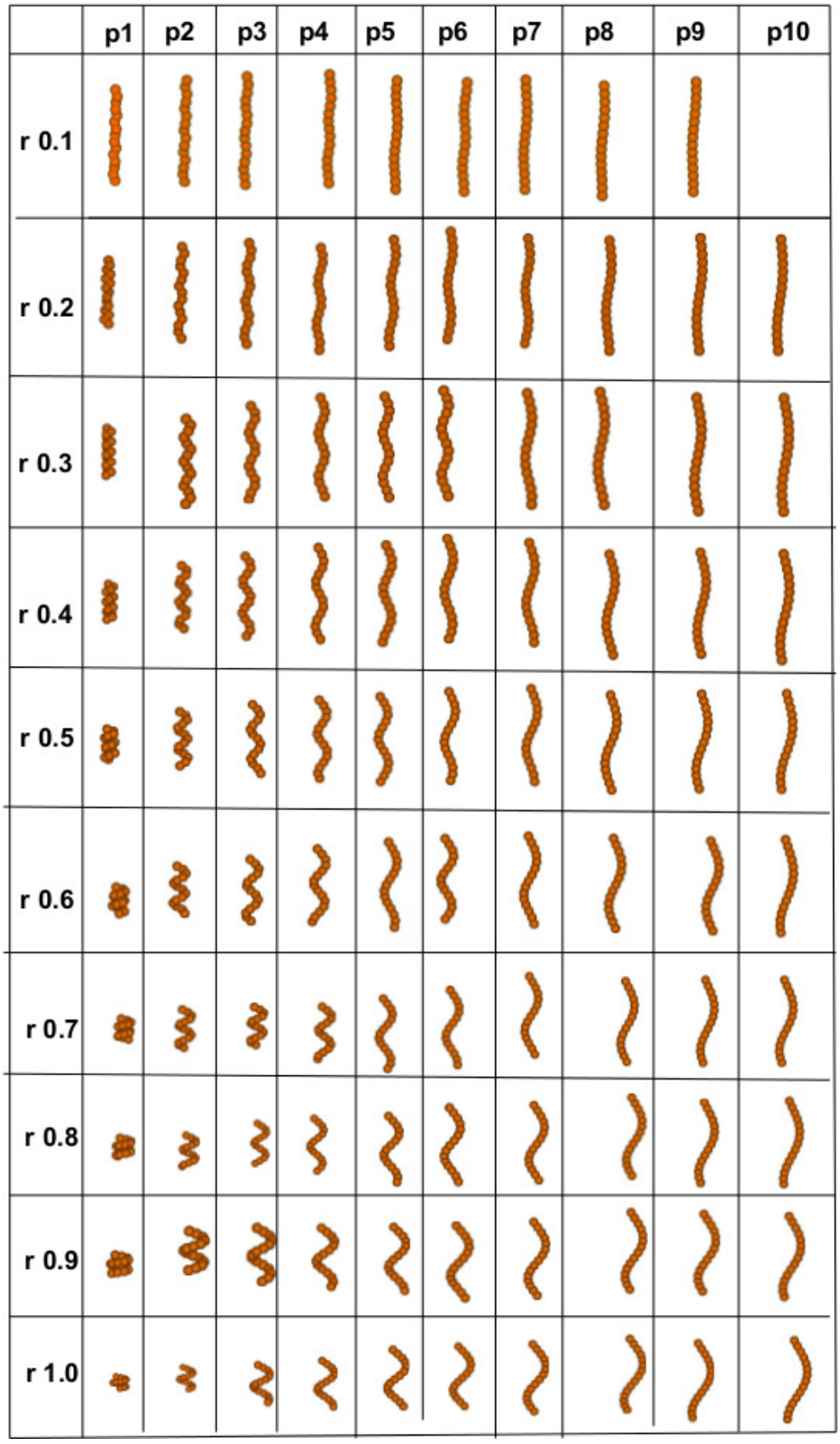

FIGURE 4.8: Helical shapes studied with r ranging from 0.1 to 1.0 and p ranging from 1 to 10

simulated annealing Monte Carlo moves within the ISSM. In this method the long axis of helix is perpendicular to the plane with centre of the helix lying on a plane. The rotational move brings change in the orientation of helix about its long axis. The overlap check is done by considering the full 3D structure of the helix. The configurational parameters in 2D are used to get the information the details of the 3D structure. All six configurational parameters in a plane are used to build a 3D helix.

Unit cell lengths and angle ($cell_x$, $cell_y$ and $cell_\theta$) are used to construct a rotation matrix.

$$\begin{pmatrix} cell_x & cell_y \cos(cell_\theta) & 0 \\ 0 & cell_y \sin(cell_\theta) & 0 \\ 0 & 0 & \Lambda + D \end{pmatrix}$$

The position of the helix is given by the position coordinates(L_x, L_y). The quaternion to represent the orientation is obtained from L_θ.

$$\begin{aligned} q0 &= \cos(L_\theta/2) \\ q1 &= 0 \\ q2 &= 0 \\ q3 &= \sin(L_\theta/2) \end{aligned}$$

Knowing the position and orientation of each helix, the overlap test is done implementing the procedure discussed in chapter 3.

4.6 Calculating volume fraction

The volume fraction is defined as

$$\eta = \frac{n_h V_h}{V_{cell}} \tag{4.3}$$

where n_h is the number of helices, V_h is the volume of the helix V_{cell} is the volume of the crystalline unit cell.

The volume v_0 of a linear chain formed by m fused hard spheres of Diameter D and center to center distance d_{acc} is given by

$$v_0 = \frac{\pi}{6}D^3\left[1 + \frac{m-1}{2}\left(3\frac{d_{acc}}{D} - \left(\frac{d_{acc}}{D}\right)^3\right)\right] \tag{4.4}$$

From the ISSM we get the area (A_{cell}) of the 2d cross section of the cell. Since all helices are parallel and their long axis perpendicular to the plane, a reasonable estimate and upper bound for the volume of the 3D cell is obtained by multiplying area of the 2D cell with height of the helix ($\Lambda + D$)

$$V_{cell} = A_{cell}(\Lambda + D) \tag{4.5}$$

4.7 Results and Discussion

Our aim is to determine the relation between the shape of the helix and its maximum packing density η_{max}. Because of the asymmetry and voids in the shape of the helix, helices intercalate. The level of maximum intrusion depends on the helix parameters r and p. Because of the chirality in the shape, the relative orientation of the helices (twist) around their long axes plays a major role in achieving packing density. The results obtained from ISSM not only give the relation between the shape of the helix and its maximum packing but also an insight into the effect of helical shape on intercalation coupled with the twist of the C_2 axis.

All the helical shapes, except a few cases with $p = 1$, have their best packing structure in the p1 wall paper group with one occupied Wyckoff site i.e., one particle per unit cell [71] [72]. Arrangement of helices in the p1 wall paper group can be seen in the figure 4.1. This indicates that all the helices are in register and oriented in the same direction. The compact structures of helices are characterized by the inter penetrating helices with their C_2 axes preferably aligned in one direction. Though all the helical shapes resulted in similar arrangement, the major difference is observed in their respective packing densities. The overlapping region in circles varies with the shape of the helix. The bigger the overlap, the better is the packing. Three such cases are shown in figure 4.9 in the order of increasing packing fraction. The corresponding helical parameters are shown inside the figure. The three structures are in the order of $\eta_{max} = 0.37; 0.58; 0.76$. The increase in the overlapping area with increasing packing fraction is clearly visible.

A few helical shapes found their best packing in p1 wall paper group with two or three occupied Wyckoff sites. Helices with $r = 0.2$, $p = 1$; $r = 0.5$, $p = 1$; $r = 0.7$, $p = 1$ obtained maximum packing with two occupied Wyckoff sites. The helix with $r = 0.8$, $p = 1$ obtained maximum packing with $N_{occ} = 3$. All these shapes are tightly coiled helices with $p = 1$. Figure 4.10 shows two such cases with two occupied Wyckoff sites.

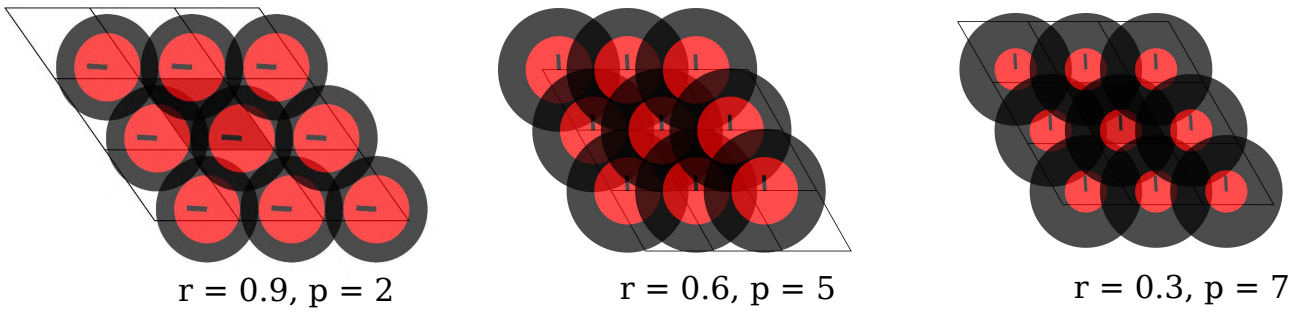

FIGURE 4.9: Structures with maximum packing density for helices having $r = 0.9$, $p = 2$ at $\eta = 0.37$; $r = 0.6$, $p = 5$ at $\eta = 0.58$; $r = 0.3$, $p = 7$ at $\eta = 0.76$;

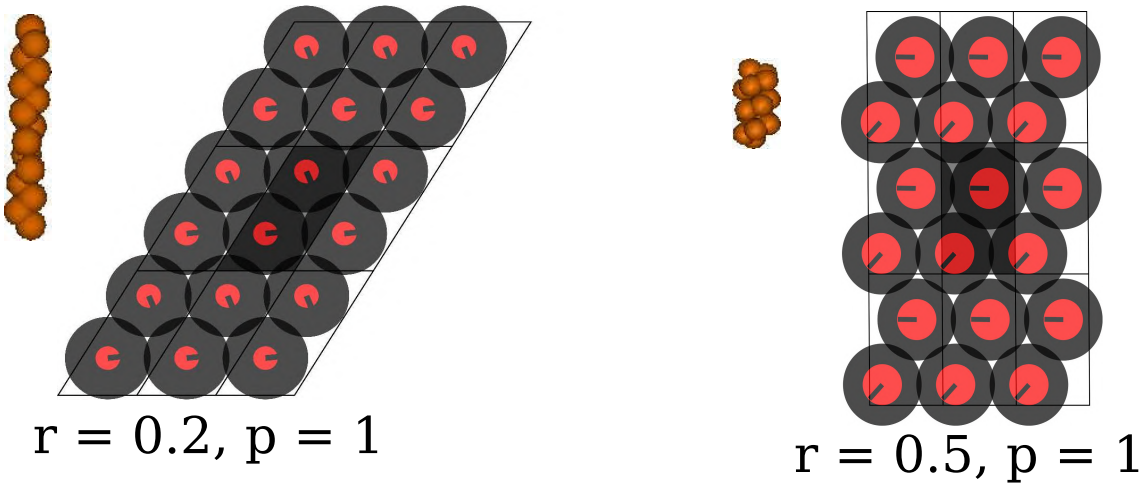

FIGURE 4.10: Structures with $N_{occ} = 2$

Note that that the C_2 axes of the particles are aligned. The tight pitch of these helices does not allow any possibility of the interpenetration, so the best packing depends on the detailed match between the spheres on the outer surfaces.

4.7.1 Maximal packing density as a function of radius and pitch

Figure 4.11 shows a surface plot of the maximum volume fraction projected on to a plane of radius and pitch. The colour bar next to the plot indicates the colour variation with the value of η. The numbers shown inside the plot are the values of η. The shape of each helix is shown for every combination of radius and pitch. There is a clear trend in the η_{max}. Very curly helices are not good candidates for the best packing. The intermediate helices showing the intermediate packing density. After a certain crossing, there is a plateau region showing the similar packing density. From the figure, one can draw the conclusion that neither slender helices nor curly helices are giving the highest packing. The highest packing 0.78 is achieved by intermediate helices with particular combination of radius and pitch.

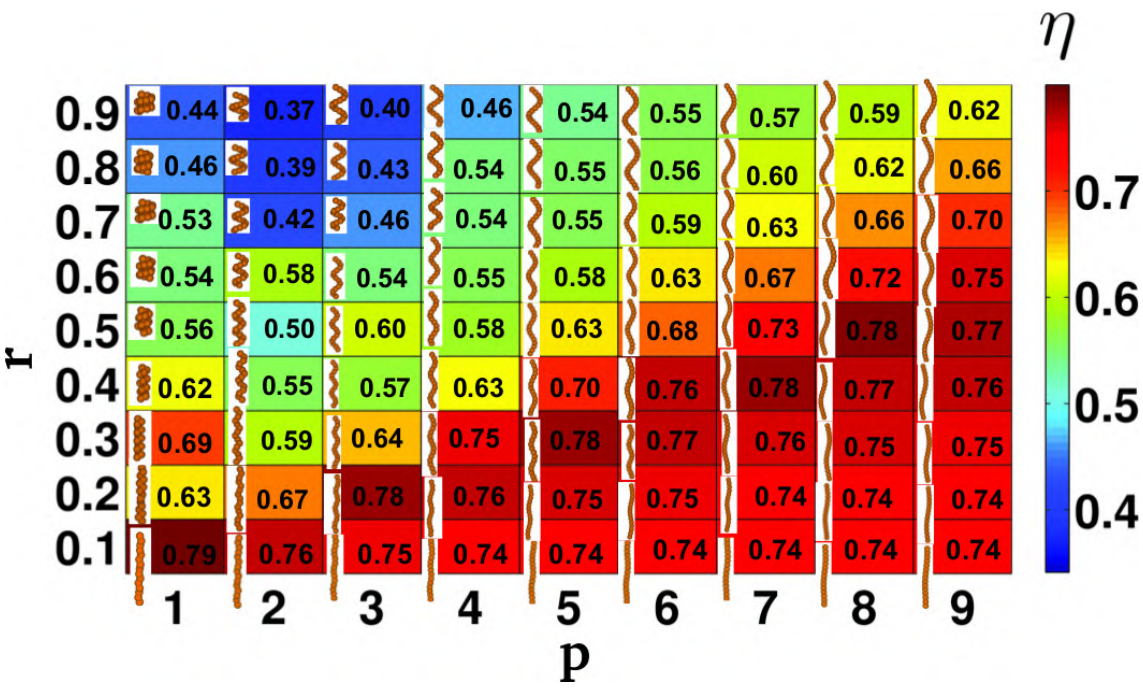

FIGURE 4.11: Colour map of the maximal volume fraction, η, achievable by a given helix as a function of its radius r and pitch p. The color code is from dark red (high packing) to dark blue(low packing). The value on the side of each helix is its effective aspect ratio,$(\lambda/(2r+D))$. The cartoon on the bottom left of each r, p pair shows the corresponding helix shape

Since all the helices are restricted to a plane, it is interesting to see the areal number density (A_{den}) in a plot similar to 4.11. The figure 4.12 shows the areal number density $A_{den} = N_h/A_{cell}$ plotted in radius and pitch plane. Figure 4.11 and 4.12 are showing similar patterns. However in the areal number density plot, there are no irregularities in the plateau region. This shows that after the cross over all helices are equally dense in the plane. The small differences observed in the figure 4.11 are due to the structure of helix and volume of the helix.

The other important purpose of ISSM is to obtain the compact initial configuration for NPT MC simulations. We obtain a single layered compact structure from ISSM. The initial configuration is constructed by replicating this layer exactly one top on another. Though the information about the arrangement between the layers is missing, this act as a good starting point for the expansion. I discuss about these compact structures in chapters 5 and 6.

4.8 Conclusions

Helical shapes are chiral in nature and studying densest packing of this chiral object constitutes an interesting subject. Using isopointal set structural search method (ISSM),

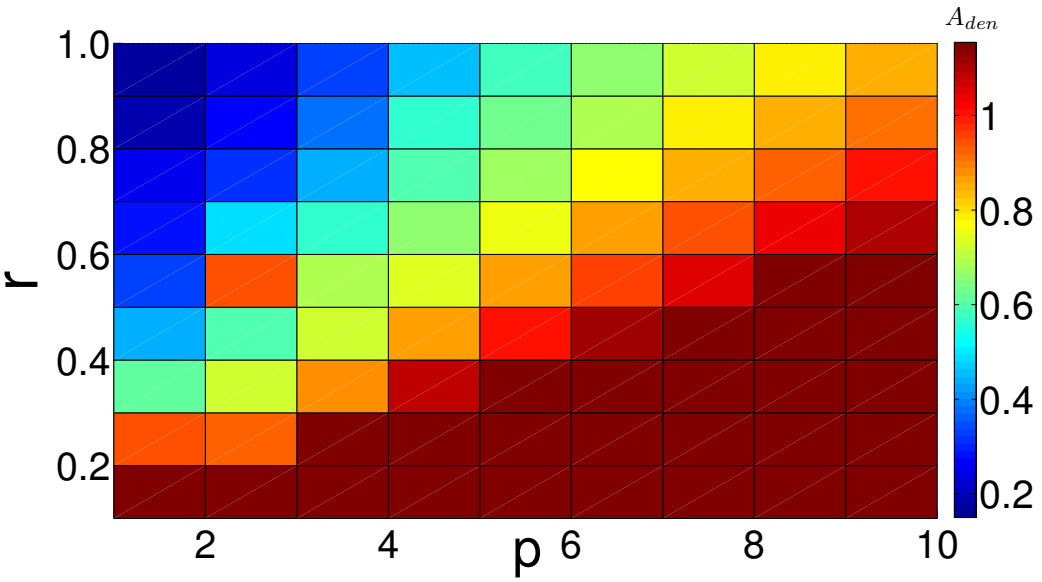

FIGURE 4.12: Colour map of the areal number density, A_{den}, achievable by a given helix as a function of its radius r and pitch p. The color code is from dark red (high packing) to dark blue(low packing).

we obtained the maximum packing fraction of different shapes of helices. All the helices are found to be well packed in p1 wallpaper group. Except few cases with $p = 1$, we found one particle per unit cell for all shapes showing that helices prefer hexagonal ordering to achieve high packing densities. A clear trend is seen in the volume fraction obtained for different helical shapes. Neither curly helices nor slendor helices are giving the best packing density. Those helices with intermediate helicity found to be well packed. However areal density is found to be similar for all those helices lying after the crossover. This indicate that planar density is similar and differences are arising due to the height of the helix and the volume of the helix. The structure thus obtained can be used as the initial configuration for Monte Carlo simulation and especially to trace the compression curve. The single layer obtained from ISSM is replicated by stacking one top on another to construct an initial configuration.

Chapter 5

Evidence of new screw-like nematic phase

5.1 Introduction

We have discussed the isotropic-nematic transition for helical particles in Chapter 3. Elongated particles form a nematic phase upon compression. Non convex shapes like helices are expected to show unconventional behaviour at higher densities. The shape of the helix plays a key role in the self assembly and thus exhibit a different phase behaviour at higher densities. In this chapter I introduce a special chiral nematic phase which is peculiar to the helix shape. The new phase observed is based on the screw-like order that develops at higher densities in the system [73]. Using NPT MC, a strong evidence of the new stable chiral nematic phase is provided in this chapter [71] [72]. This phase occupies a significant region in the phase diagram. However the screw-like order propagates to the higher densities resulting in the new chiral smectic phases. These phases are discussed in chapter 6.

In our model, shape of the helix is defined by a radius and a pitch. The long axis of the helix is denoted by $\hat{\mathbf{u}}$. In the nematic phase, all the $\hat{\mathbf{u}}$ axes tend to align in one direction and this direction is denoted by main director $\hat{\mathbf{n}}$. In the cholesteric phase [6] [74], this $\hat{\mathbf{n}}$ spirals about a perpendicular axis to $\hat{\mathbf{n}}$. The local chiral character of the helical constituents translates into a global chirality resulting in a chiral nematic phase. Similarly we define a C_2 axis perpendicular to $\hat{u}$ to each helix. In principle, any axis passing through the center of the helix (midpoint of the long axis $\hat{\mathbf{u}}$) perpendicular to $\hat{\mathbf{u}}$ is two fold (C_2) symmetry axis. Inorder to define the rotation of the helix about long axis $\hat{\mathbf{u}}$, a fixed C_2 symmetry axis $\hat{\mathbf{w}}$ is considered for each helix as shown in the figure. Like $\hat{\mathbf{n}}$, $\hat{\mathbf{w}}$ axes can orient along a specific direction $\hat{\mathbf{c}}$. Similar to the cholesteric phase,

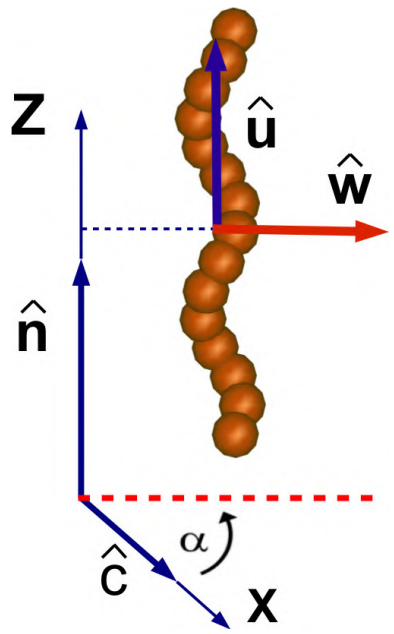

FIGURE 5.1: Helix with arrows showing the unit vectors $\hat{\mathbf{u}}$ and $\hat{\mathbf{w}}$ defined in the molecular frame, and the unit vectors ($\hat{\backslash}$,$\hat{\mathbf{c}}$) defined in the laboratory frame. X,Z are the axes of the laboratory frame, with α the angle between $\hat{\mathbf{w}}$ and the X-axis.

this phase is still nematic in that helices are homogeneously distributed and mobile with their long axis $\hat{\mathbf{u}}$ preferentially oriented along the main director $\hat{n}$. In contrast to the cholesteric phase, in this new organization it is the short axes, $\hat{\mathbf{w}}$, that spirals around $\hat{\mathbf{n}}$ with a periodicity equal to helix pitch. In this work we refer this order as screw-like order and the nematic phase with screw-like order as screw nematic N_S^*.

5.2 Understanding screw-like order

When helices are far apart, they are free to rotate about their long axes. In this case, helices behave like rods as shown in the figure 5.2. At lower densities, helical shape is not so relevant and the liquid crystal phase thus formed is a conventional nematic phase. This is however no longer the case when the helices are in close contact. In close contact, one turn of a helix can intrude into the groove of the other helix resulting a in-phase locked configuration as illustrated in figure 5.2. This intrusion limits the orientation of $\hat{\mathbf{w}}$ axes of the helix. This restriction on the C_2 axes of particles lowers the rotational entropy. This is compensated by the gain in the translation entropy in order to form a new stable chiral nematic phase. The translation is coupled to the rotation giving rise to a screw like motion. This is schematically shown in the figure 5.3.

This screw organisation develops in the system and is peculiar to the helical shape. The N_S^* phase is a new kind of chiral phase different from the chiral nematic (N^*)phase. In

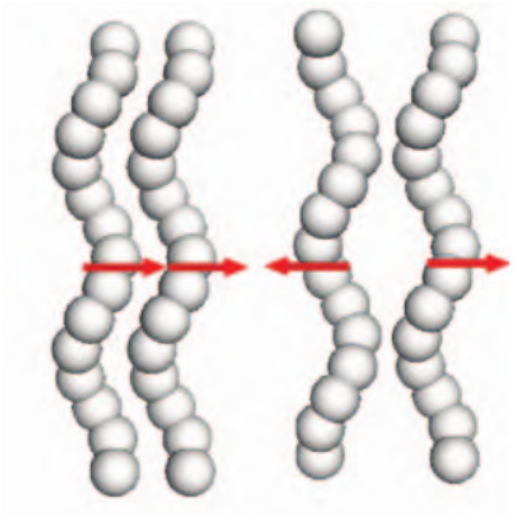

FIGURE 5.2: Pair of helices inphase and antiphase

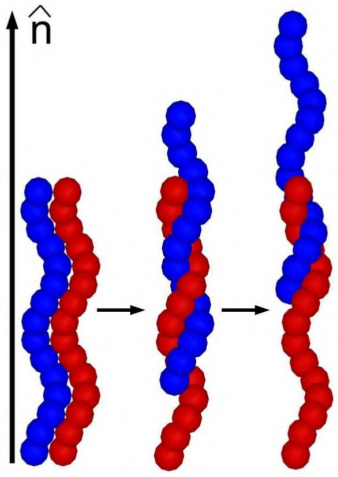

FIGURE 5.3: Screw like motion showing translation coupled rotation

the cholesteric phase the $\hat{\mathbf{u}}$ axes of the helices spiral around a perpendicular axis–$\hat{h}$– as illustrated in figure 5.4. The order of the $\hat{\mathbf{u}}$ axes is non polar, i.e, there is up-down symmetry. In the N_S^* phase $\hat{\mathbf{u}}$ axes are preferentially aligned along the same direction through out the sample, but the transverse $\hat{w}$ axes spiral around this direction as depicted in 5.4 . In this case the $\hat{\mathbf{w}}$ axes have polar order, i.e. they preferentially point in the same direction. Another important difference between screw-nematic and cholesteric is the length scale of the phase periodicity. In N_S^* the pitch of the phase is equal to the pitch of the particle where as in the cholesteric phase the pitch is orders of magnitude longer than the size of the particle. Because of this reason, screw-like nematic can be observed in numerical simulations with box size comparable to the particle length.

The screw nematic can also be described in Frenet frame [Appendix C] which is usually used for the flexible and semi flexible polymers description. This description was used in the experimental work done on helical flagella by Barry *etal* [5]. The screw-like nematic

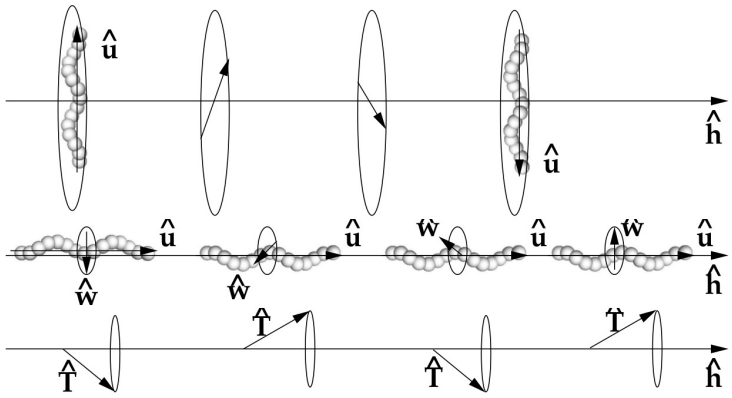

FIGURE 5.4: Top: Cartoon showing the orientation of the $\hat{\mathbf{u}}$ of helix in cholesteric phase. Middle: Cartoon of the screw-like nematic phase showing the orientation of $\hat{\mathbf{w}}$. Here $\hat{\mathbf{h}}$ is a unit vector parallel to the axis around which $\hat{\mathbf{u}}$ or $\hat{\mathbf{w}}$ rotates. Bottom: Another representation of screw-like nematic showing conical path. Here $\hat{\mathbf{T}}$ is the local tangent of the helix.

phase can be viewed as the conical movement of the local tangent of helices along the director. As shown in the bottom panel of the figure 5.4, the tip of the local tangent ($\hat{\mathbf{T}}$) follows a conical path on moving along the director ($\hat{\mathbf{n}}$), due to the variation of the azimuthal angle at fixed polar angle. We used the same idea for the visualization of snapshots, colour coded according to the local tangent of helices.

5.3 Experimental evidence of the screw nematic phase

There is an experimental evidence to this kind of organization found in helical flagella[]. A transition from isotropic to N_S^* phase as density increases has been observed in colloidal suspensions of helical flagella by Barry *etal.*, using polarizing and differential interference contrast microscopy, combined with experiments on single particle dynamics. A striped birefringent pattern was observed consistent with a picture where the local tangent of the helix, tilted with respect to $\hat{\mathbf{n}}$, is rotating in a conical way. By analogy with a similar behaviour occurring for the cholesteric phase in the presence of an external field parallel to the twist axis, this phase was denoted as conical, although the underlying mechanism and detailed structure is different. Figure 5.5 shows the screw nematic phase observed in helical flagella.

5.4 Characterization of the screw Nematic(N_S^*)

In order to fully characterize the new phase, we need a special set of correlation functions and order parameter are required. We used lowest rank order parameter $\langle P_{1,c} \rangle$ which is

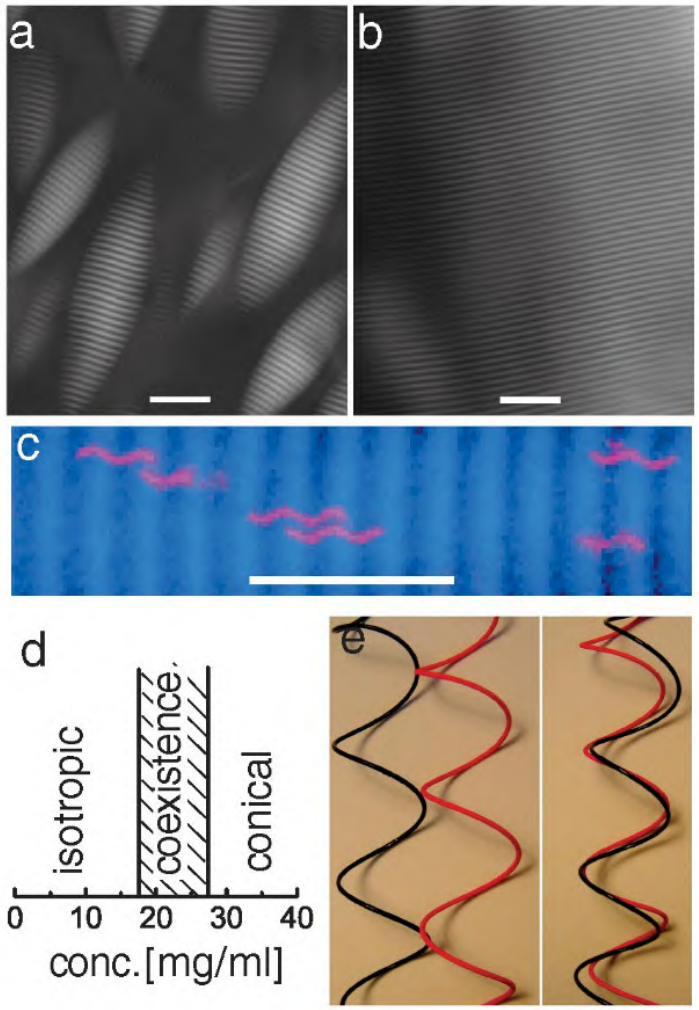

FIGURE 5.5: Experimental results on flagella SJW1103 [5]. (a) and (b) coexistence and single phage with polarized microscope. (c) fluorescently labelled flagella dissolve in conical medium. (d) phase diagram of flagella (e) schematic showing the excluded volume between two helices.

related to the one proposed in the framework of a theoretical description of a screw like organization [24].

$$\langle P_{1,c} \rangle = \langle \hat{\mathbf{w}}.\hat{\mathbf{c}} \rangle \tag{5.1}$$

where $\hat{\mathbf{w}}$ is the fixed C_2 axis shown in the figure 5.1, $\hat{\mathbf{c}}$ is the local nematic director of the $\hat{\mathbf{w}}$ axes. This order parameter measures the average alignment along a common direction($\hat{\mathbf{C}}$) of the secondary axes($\hat{\mathbf{w}}$) of helices having their centre of mass on the same plane perpendicular to the main director $\hat{\mathbf{n}}$.

This cannot be directly implemented as it involves the information of $\hat{\mathbf{c}}$. So the following

procedure is followed to avoid the problem of finding local $\hat{\mathbf{c}}$ director. For each configuration, after having determined nematic director $\hat{\mathbf{n}}$ as explained in 3, a rotation of $-2\pi Z_i/p$ around $\hat{\mathbf{n}}$ is imposed on the coordinates of the particles. This is the untwisting of $\hat{\mathbf{w}}$ axes done about $\hat{\mathbf{n}}$. The exact angle to untwist depends on the position Z_i of the particle in the box as we know that pitch of the phase is equal to the pitch of the particle p. Then the $\hat{\mathbf{c}}$ is calculated following the procedure explained in 3 for nematic order parameter of $\hat{\mathbf{w}}$ instead of $\hat{\mathbf{u}}$. Then the quantity $\hat{\mathbf{w}}.\hat{\mathbf{c}}$ is calculated for each helix and finally $\langle P_{1,c}\rangle$ is obtained by averaging over all helices and configurations. This parameter enables us to distinguish between conventional Nematic and screw-nematic by giving non zero value for N_S^* and near zero value for N.

Another way to characterize the phase is by using orientational pair correlation function defined as

$$g_{1,||}^{\hat{w}}(R_{||}) = \langle \hat{\mathbf{w}}_i.\hat{\mathbf{w}}_j\rangle_{R_{||}} \tag{5.2}$$

where $R_{||} = R_{ij}.\hat{\mathbf{n}}$, the projection of the interparticle seperation R_{ij} along the $\hat{n}$ axis. Thus $g_{1,||}^{\hat{\mathbf{w}}}$ is computed as a function of the distance projected along the main director. This gives the information about polar correlation between the C_2 symmetry axes of two helices.

5.5 Results and discussion

In this section, I present results from NPT Monte Carlo simulations showing the emergence of the screw-like order and discuss its dependence on the geometry of the helix. This section focuses only on screw-like order in the nematic region. Propagation of the screw like order in denser phases (like the smectic phase) is discussed in chapter 6. We found three different transitions: IN (isotropic-nematic); $N - N_S^*$ (nematic-screw nematic); and $I - N_S^*$ (isotropic-screw nematic) in the nematic region depending on the helical parameters. Near rod like helices with $r = 0.1$ show conventional IN transition similar to that of found in spherocylinders. For helices with $r = 0.2$, as the volume fraction increases, a first order IN transition is followed by a second order $N - N_S^*$ transition. For helices with $r = 0.3$ and $r = 0.4$, depending on the pitch value we see a direct first order $I - N_S^*$ transition.

In the sub-section 5.5.1, characterization of $N - N_S^*$ transition is discussed in detail by showing the order parameter and correlation function curves. In the sub-section 5.5.2, $I - N_S^*$ transition is discussed by showing the order parameter and correlation function

plots. In sub-section 5.5.3 phase diagrams are shown, discussing the effect of r and p on the screw-like order.

5.5.1 N - N_S^* transition

Figures 5.6, 5.7 and 5.8 show the equation of state in P^* versus η plane for helices having $r = 0.2$ and $p = 8$, 6 and 3 respectively. All the points in the equation of state are obtained from NPT MC simulation implemented as explained in chapter 3. Points labelled as I, N, N_S^* and Sm correspond to isotropic, nematic, screw nematic and smectic phases respectively and each phase is indicated with different colour. Yellow indicates isotropic; blue indicates nematic; red indicates screw-like nematic and green indicates smectic. The same colour convention is followed in the rest of the document. These phases are distinguished with the help of order parameters $\langle P_2 \rangle$, $\langle P_{1,c} \rangle$, τ_1 and the correlation function $g_{1,\|}^{\hat{\mathbf{w}}}$. The details of the smectic and higher density phases are discussed in chapter 6.

From these figures it is evident that the system first undergoes IN transition as η increases and followed by a $N - N_S^*$ transition, with N_S^* always occurring at $\langle P_2 \rangle$ close to 1. For a fixed radius, aspect ratio of each helix decreases with a decrease in pitch. In going from $p = 8$ to 3, we see the location of the IN transition moving towards higher densities and also decrease in the width of net nematic region ($N + N_S^*$). This change can be qualitatively understood in terms of the decrease in the aspect ratio (as explained in chapter 3).

When the η value is sufficiently high and all the particles are aligned along a common direction, the $N - N_S^*$ transition occurs because of the interlocking of the grooves of helices. We notice an increase in the width of N_S^* region with the decrease in pitch. With the decrease in the aspect ratio the system is gradually favouring screw nematic over conventional nematic. This is due to the fact that the nematic phase tends to stabilize at higher densities for shorter helices. When the density is high enough, helices with lower pitch values interlock giving rise to the screw like motion.

Figure 5.9 shows $\langle P_2 \rangle$ as a function of η for helices with $r = 0.2$ and decreasing pitches $p = 8$, 6 and 3. Figure 5.10 shows $\langle P_{1,C} \rangle$ as a function of η for helices with $r = 0.2$ and decreasing pitches $p = 8$, 6 and 3. Different colours are used to indicate different phases. Different symbols are used to indicate different pitch values. An IN transition is associated with the jump in $\langle P_2 \rangle$. It is clearly visible that the location of the IN transition is shifting from $\eta \approx 0.24$ to $\eta \approx 0.3$ with decreasing pitch, in agreement with the results shown in chapter 1, where as the location of $N - N_S^*$ transition moves towards lower η with decreasing pitch. This can be explained as a combined effect of aspect ratio and

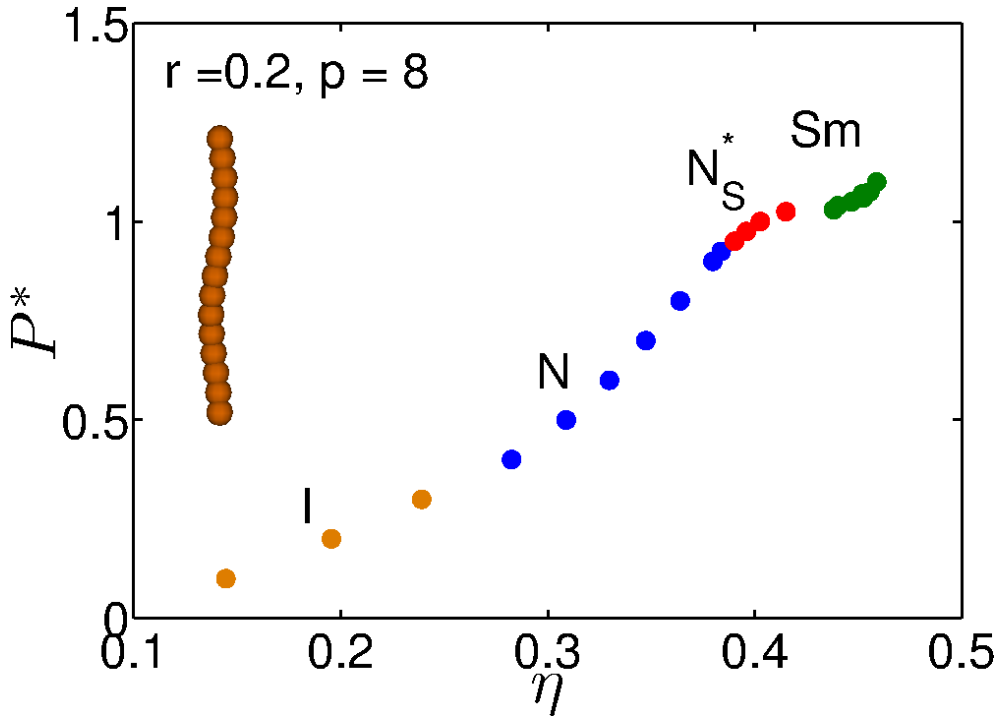

FIGURE 5.6: Equation of state plotted in reduced pressure P^* - volume fraction η plane for helices having r = 0.2 and p = 8. Different colours indicate different phases. Yellow circles(I)-isotropic; Blue circles(N)-nematic; Red circles(N_S^*)-screw nematic; Green circles(Sm)- smectic.

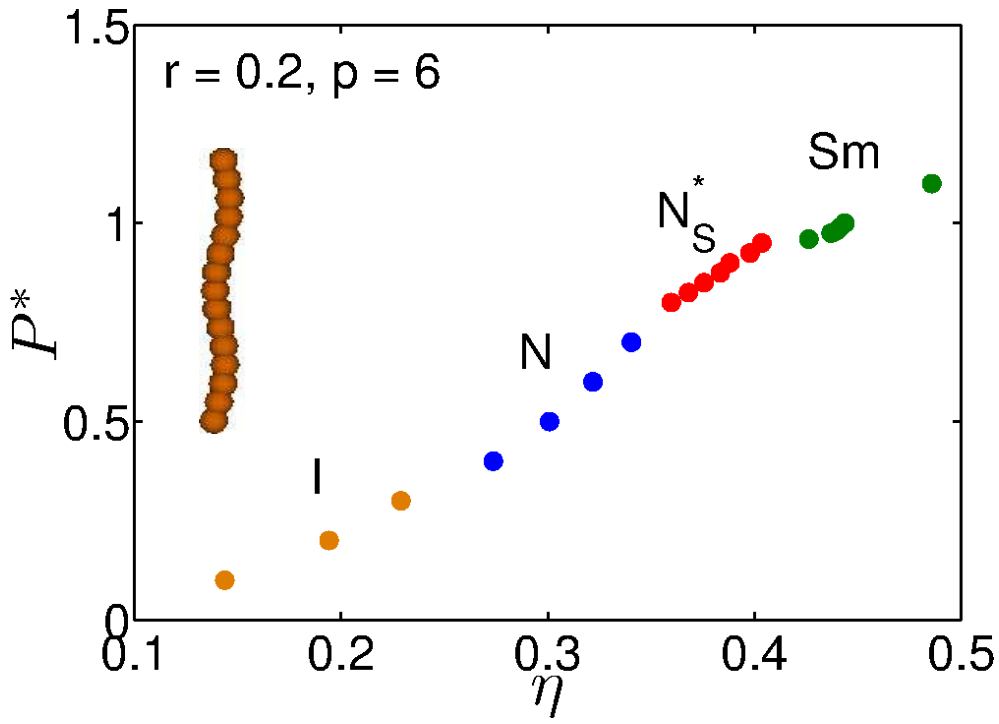

FIGURE 5.7: Equation of state plotted in reduced pressure P^* - volume fraction η plane for helices having $r = 0.2$ and $p = 6$. Different colours indicate different phases. Yellow circles(I)-isotropic; Blue circles(N)-nematic; Red circles(N_S^*)-screw nematic; Green circles(Sm)- smectic.

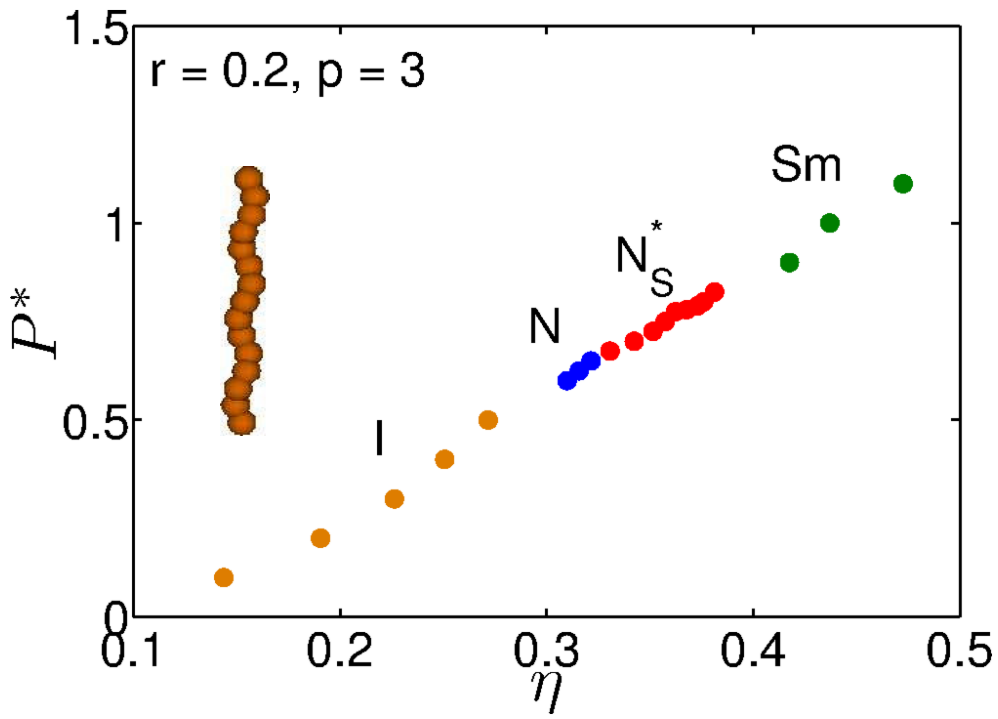

FIGURE 5.8: Equation of state plotted in reduced pressure P^* - volume fraction η plane for helices having $r = 0.2$ and $p = 3$. Different colours indicate different phases. Yellow circles(I)-isotropic; Blue circles(N)-nematic; Red circles(N_S^*)-screw nematic; Green circles(Sm)- smectic.

pitch of the helix. Because of its high aspect ratio, helices with pitch = 8 tend to form nematic phase at lower η but because of the less curly shape, screw like order develops only at higher η. Shorter helices like helices with $p = 3$ tend to form nematic phase at higher η but because of the more curly shape, screw like order develops at lower η when compared to slender helices.

Figures 5.11 and 5.12 show the correlation function $g_{1,\parallel}^{\hat{\mathbf{w}}}$ calculated for helices r = 0.2, p = 3 and r = 0.2, p = 6. In both cases, a sinusoidal wave with periodicity equal to p is clearly visible. Constant amplitude at long inter-particle distance indicates this as a long range correlation. This behaviour reflects the chiral organization of each particles $\hat{\mathbf{w}}$'s along $\hat{\mathbf{n}}$ and is the signature of screw-like ordering. The onset of the screw-like ordering with increasing volume fraction is clearly visible. For helices having $r = 0.2$, $p = 3$, $g_{1,\parallel}^{\hat{\mathbf{w}}}$ is close to zero everywhere at $\eta = 0.32$ showing lack of correlation between $\hat{\mathbf{w}}$ axes and at $\eta = 0.36$, maximum amplitude oscillation shows fully developed correlation. Oscillation continuously grows up with increasing η and $g_{1,\parallel}^{\hat{\mathbf{w}}}$ oscillate between ± 1 when perfect ordering occurs. The behaviour of $\langle P_2 \rangle$ in the figure 5.9 is a suggestive of a first order IN transition and the behaviour of $\langle P_{1,c} \rangle$ in figure 5.10 and correlation functions in figures 5.11, 5.12 indicate $N - N_S^*$ second order $N - N_S^*$ phase transition.

Figure 5.13 shows snapshots for helices with $r = 0.2$ and $p = 6$ at $\eta = 0.359$ to 0.397

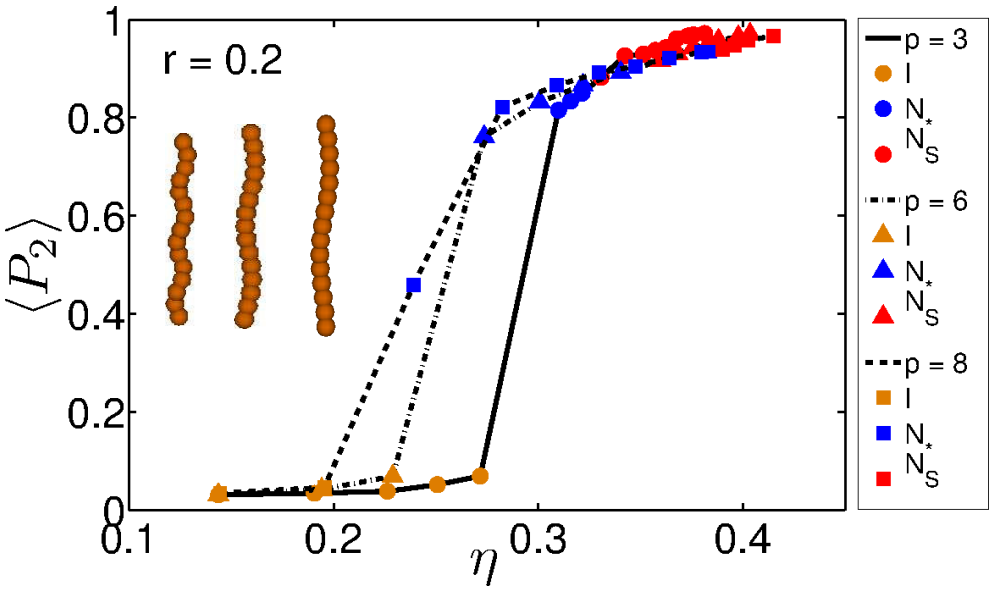

FIGURE 5.9: $\langle P_2 \rangle$ plotted as a function of η in the case r = 0.2 and different values of pitch. $p = 3$ (solid circles); $p = 6$ (solid triangles); $p = 8$ (solid squares).

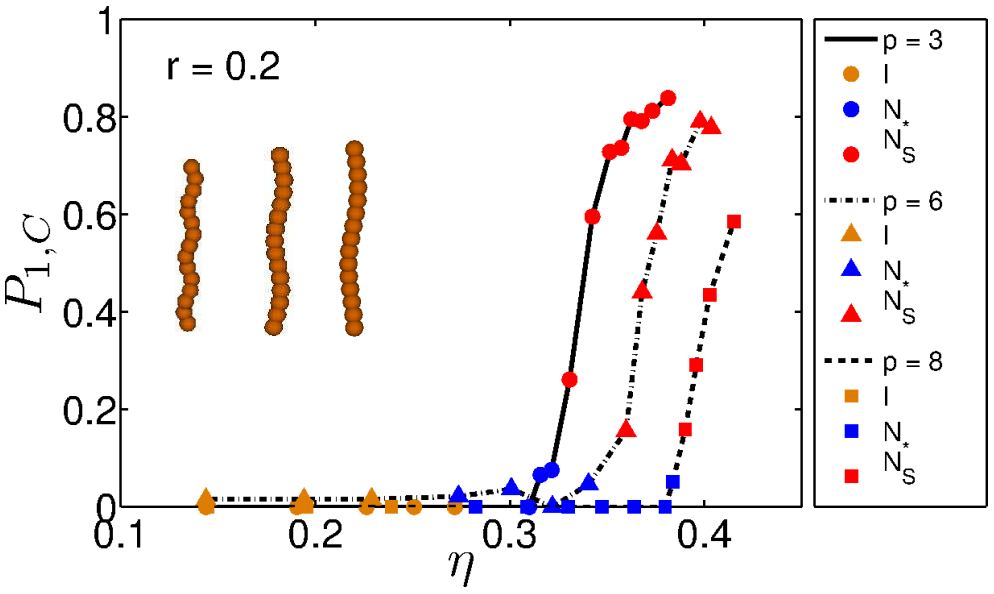

FIGURE 5.10: $\langle P_{1,C} \rangle$ plotted as a function of η in the case r = 0.2 and different values of pitch. $p = 3$ (solid circles); $p = 6$ (solid triangles); $p = 8$ (solid squares).

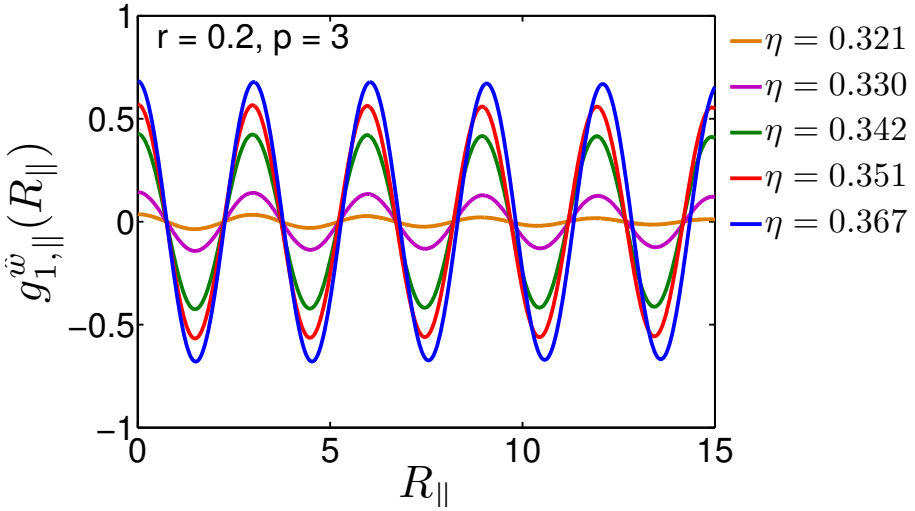

FIGURE 5.11: Correlation functions $g^{\hat{\mathbf{w}}}_{1,\|}(R_\|)$ showing the emergence of screw-like order with increasing η in case of helices with $r = 0.2$ and $p = 3$. Different colours are used to show correlation at different values of η

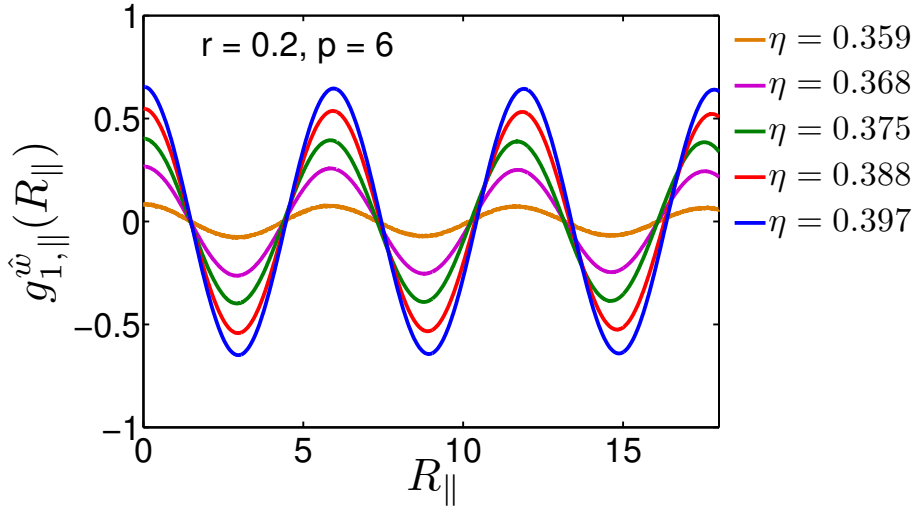

FIGURE 5.12: Correlation functions $g^{\hat{\mathbf{w}}}_{1,\|}(R_\|)$ showing the emergence of screw-like order with increasing η in case of helices with $r = 0.2$ and $p = 6$. Different colours are used to show correlation at different values of η

as shown in figure 5.12. In this figure helices are colour coded according to their local tangent. The colour bar shown in the figure shows the variation of colour with angle say θ going from 0 to 90 degrees. Here θ is the angle between the local tangent of the helix and x=y=z axis. The colour changes as the tangent moves along the helix and thus the periodicity of the colour pattern is equal to the pitch of the helix. So the presence of regular colour stripes correspond to a N_S^* phase and their absence corresponds to a N phase. This visual representation is in support of the interpretation of screw-like order in figures 5.10, 5.12. From snapshots, we can observe a gradual change in the ordering, going from a random coloured state to periodic colour stripes with increasing η value.

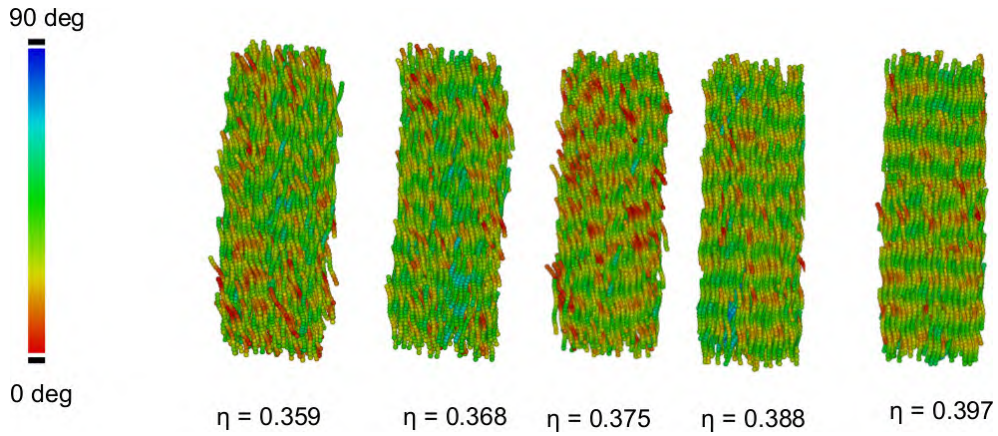

FIGURE 5.13: Visual representation of the emergence of screw like order in $N - N_S^*$ transition for the system of helices with $r = 0.2$ and $p = 6$. Snapshots and their corresponding η's are shown. Helices are colour coded according to their local tangent.

5.5.2 I - N_S^* transition

Figures 5.14, 5.15 and 5.16 show the equation of state in the $P^*Vs\eta$ plane for helices having r = 0.4 and p = 8;6;3. From figures 5.15, 5.16 it is evident that the systems of helices with $r = 0.4$, $p = 3$ and $r = 0.4$, $p = 6$ first undergoes a direct $I - N_S^*$ transition as η increases and is followed by a $N_S^* - Sm$ transition, with the N phase completely absent or occurring in a very narrow region. In case of helices with $r = 0.4$, $p = 8$, we can see a very narrow region of N followed by N_S^* and Sm phases. With the increase in the radius from $r = 0.2$ to $r = 0.4$, the aspect ratio decreases and helices become more curly. Due to this, nematic order develops at higher densities and thus increasing the chance of intercalation, making screw-like order more significant than the conventional nematic for this radius. Unlike the case of $r = 0.2$, the N phase is completely absent or exist in a very narrow region in case of $r = 0.4$. With the decrease in pitch, the N_S^* region decreases and acts as an intermediate phase helping the system to attain smectic order. Except $r = 0.4$ and $p = 8$ case, in other two cases $N_S^* - Sm$ transition is found to be continuous which will be discussed in detail in chapter 6.

Figure 5.17 shows $\langle P_2 \rangle$ as a function of η for helices with r = 0.4 and decreasing pitches $p = 8$, 6 and 3. Figure 5.18 shows $\langle P_{1,C} \rangle$ as a function of η for helices with r = 0.4 and decreasing pitches $p = 8$, 6 and 3. As expected, the IN transition moves towards higher densities with decreasing pitch, shown in figure 5.17. The behaviour of $P_{1,C}$ is markedly different in the case of $r = 0.4$ compared to $r = 0.2$ as depicted in figure 5.18. The simultaneous jump in both $\langle P_2 \rangle$ and $P_{1,C}$ is a suggestive of first order $I - N_S^*$ transition. Figures 5.19, 5.20 give additional insight into this direct transition. In figure 5.19, at $\eta = 0.298$, $g_{1,\|}^{\hat{\mathbf{w}}}(R_\|)$ is zero every where showing absence of correlation between $\hat{\mathbf{w}}$ axes

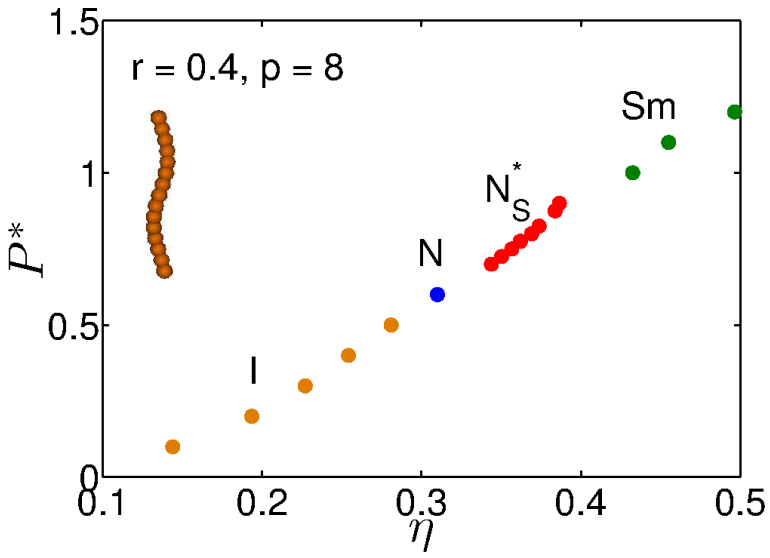

FIGURE 5.14: Equation of state plotted in reduced pressure P^* - volume fraction η plane for helices having $r = 0.4$ and $p = 8$. Different colours indicate different phases. Yellow circles(I)-isotropic; Blue circles(N)-nematic; Red circles(N_S^*)-screw nematic; Green circles(Sm)- smectic.

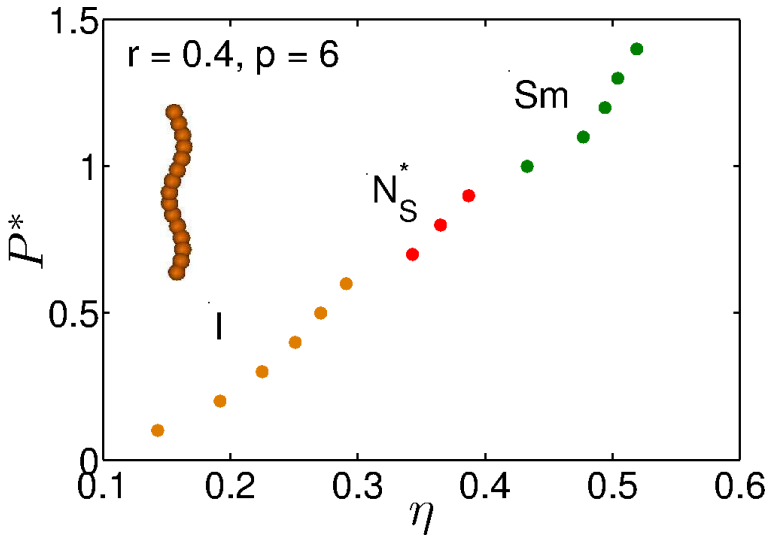

FIGURE 5.15: Equation of state plotted in reduced pressure P^* - volume fraction η plane for helices having $r = 0.4$ and $p = 6$. Different colours indicate different phases. Yellow circles(I)-isotropic; Red circles(N_S^*)-screw nematic; Green circles(Sm)- smectic.

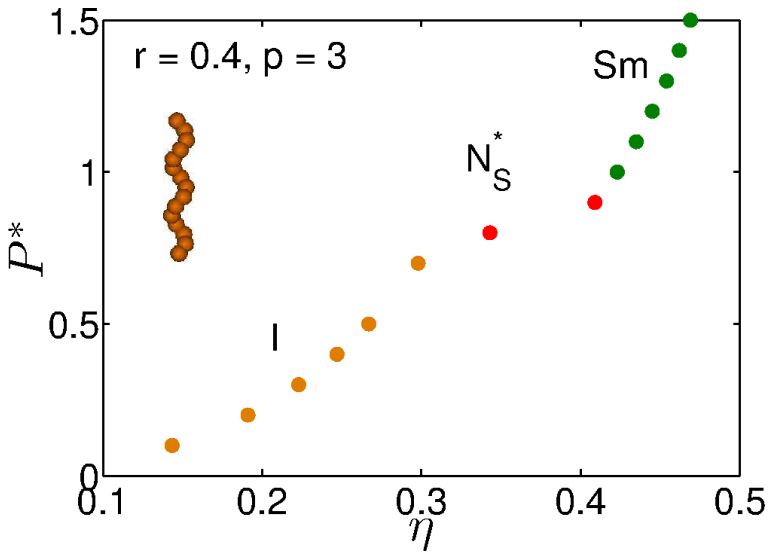

FIGURE 5.16: Equation of state plotted in reduced pressure P^* - volume fraction η plane for helices having r = 0.4 and p = 3. Different colours indicate different phases. Yellow circles(I)-isotropic; Red circles(N_S^*)-screw nematic; Green circles(Sm)- smectic.

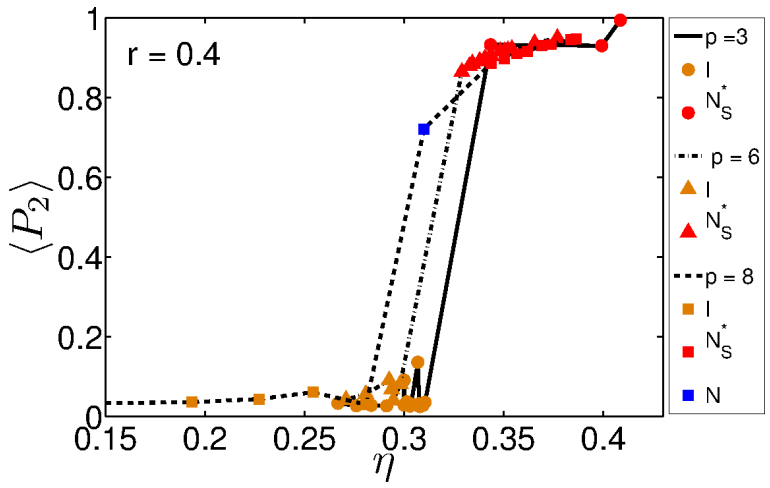

FIGURE 5.17: $\langle P_2 \rangle$ plotted as a function of η in the case $r = 0.4$ and different values of pitch. $p = 3$ (solid circles); $p = 6$ (solid triangles); $p = 8$ (solid squares).

where as at $\eta = 0.343$, system develops a full long range correlation between $\hat{\mathbf{w}}$ axes with periodicity equal to pitch of the helix .

Figure 5.21 shows snapshots for helices with $r = 0.4$ and $p = 6$ at $\eta = 0.298$ to 0.354 as shown in figure 5.12. The scheme of colour coding is the same as explained in subsection 5.5.1. This visual representation is in support of the interpretation of an $I - N_S^*$ transition shown in figures 5.18, 5.20. From snapshots, we can see a clear transition from an isotropic state shown by random distribution of colours at $\eta = 0.298$ to a screw nematic shown by regular colour stripes at $\eta = 0.329$.

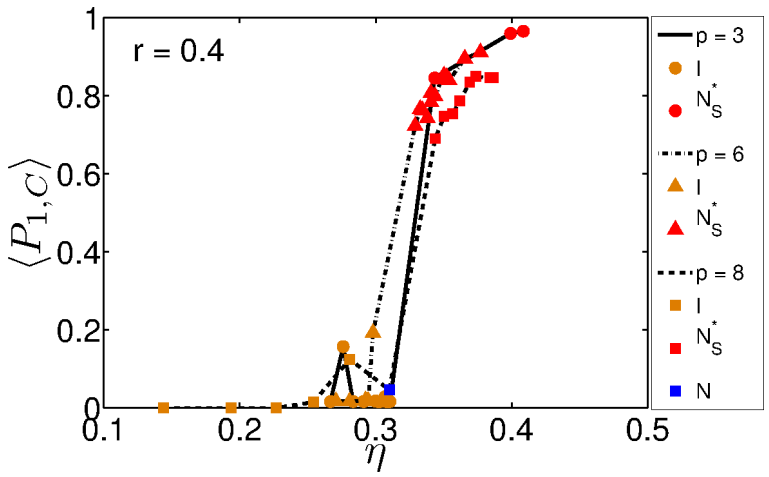

FIGURE 5.18: $\langle P_{1,c} \rangle$ plotted as a function of η in the case $r = 0.4$ and different values of pitch. $p = 3$ (solid circles); $p = 6$ (solid triangles); $p = 8$ (solid squares)

.

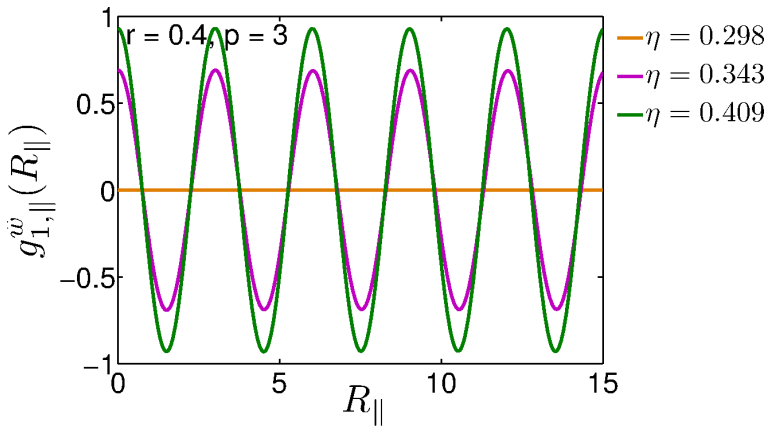

FIGURE 5.19: Correlation functions $g^{\hat{\mathbf{w}}}_{1,\|}(R_\|)$ showing the emergence of screw-like order with increasing η in case of helices with $r = 0.4$ and $p = 3$. Different colours are used to show correlation at different values of η

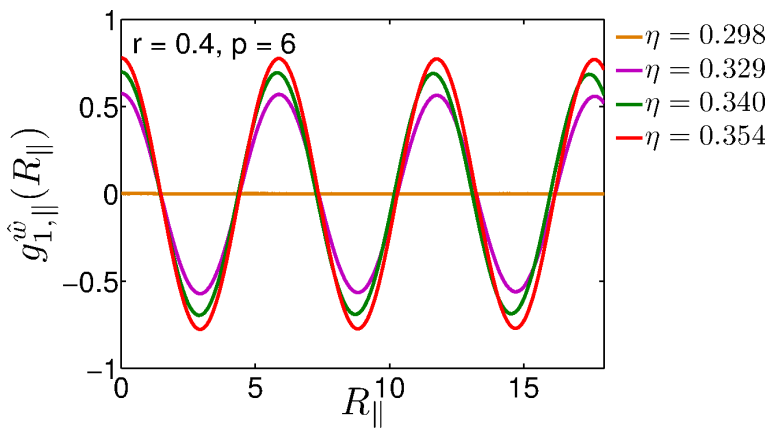

FIGURE 5.20: Correlation functions $g^{\hat{\mathbf{w}}}_{1,\|}(R_\|)$ showing the emergence of screw-like order with increasing η in case of helices with $r = 0.4$ and $p = 6$. Different colours are used to show correlation at different values of η

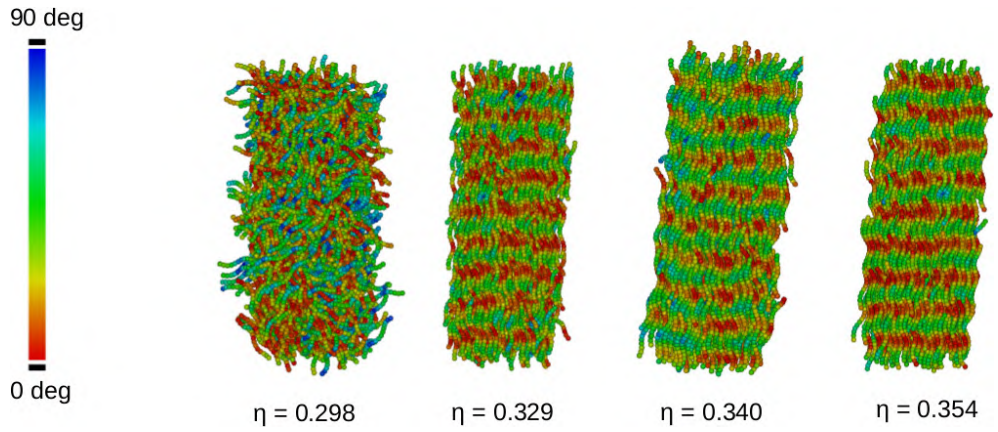

FIGURE 5.21: Visual representation of $I - N_S^* transition$ for system of helices with r = 0.4 and p = 6. Snapshots and their corresponding η's are shown. Helices are colour coded according to their local tangent.

5.5.3 Phase diagrams showing the effect of radius and pitch on Screw-like order

This section summarizes the phase behaviour of different helical shapes in nematic region. The effect of pitch on screw-like order is discussed by showing phase diagrams for each radius and different pitch values. Effect of radius is studied by comparing different phase diagrams at different radii. The data presented here is obtained from NPT MC simulation for helices with radius ranging from 0.1 to 0.4 and pitch ranging from 2 to 8. For a fixed value of the radius, the effect of pitch is shown in each phase diagram. Figure 5.22 shows the helical shapes that are studied. In the following sub sections phase behaviour of helices with $r = 0.1$ and $p = 2$ to 8; $r = 0.2$ with $p = 3$ to 8; $r = 0.3$ with $p = 2$ to 8; $r = 0.4$ with $p = 2$ to 8 are discussed. These phase diagrams help us to understand the effect of a helical shape on the IN, $N - N_S^*$ and $I - N_S^*$ transitions.

Phase diagram for $r = 0.1$

From figure 5.22 we can see that shapes with $r = 0.1$ are almost rod-like particles with very high aspect ratio. In this case we can expect phase behaviour not much deviant from that of the spherocylinder. Figure 5.23 shows the computed phase diagram of helices with $r = 0.1$ and $p = 2$ to 8. In this case we found isotropic to nematic and nematic to smectic transitions with increasing η. This phase behaviour is consistent with that of spherocylinder as shown in the phase diagram of spherocylinder in chapter1. The points plotted are shown in different colours and shapes to distinguish the phases(circles - isotropic; squares - nematic; triangles - smectic).The same colour convention defined in earlier sections is used here to shade the regions in the phase diagram. A dark yellow shade indicates an isotropic region; blue shade indicates nematic region and a green shade indicates a region with smectic and other higher density phases.

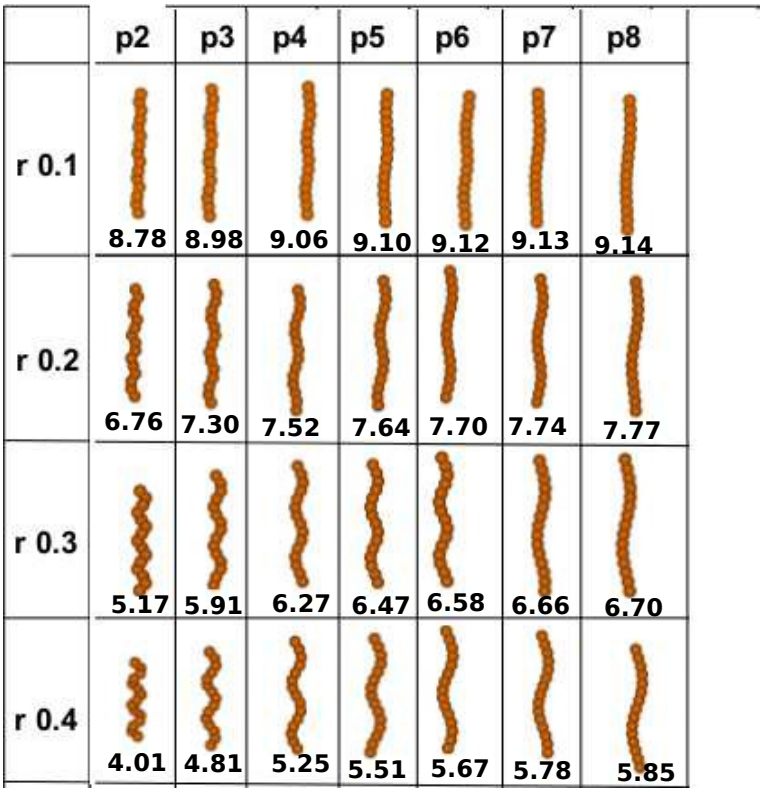

FIGURE 5.22: Helical shapes with radius ranging from $r = 0.1$ to 0.4 and $p = 2$ to 8. The numbers shown inside the picture are the corresponding aspect ratio values.

The absence of screw like order in this case is apparently due to slender rod like helical shape. The curliness in the shape is not large enough to develop a significant screw-like motion in the system. The aspect ratio of all helices is not very different and lies between 8.78 and 9.14. With an increase in the pitch, the aspect ratio increases and stabilizes the nematic phase at lower η. However the phase diagram does not show exact phase boundaries. This is the subject of our interest and currently is under study. From the order parameters calculated, it is estimated that helices with r = 0.1 exhibit a first order IN transition, followed by a first order nematic to smectic transition with increasing η.

Phase diagram for $r = 0.2$

Figure 5.24 shows the computed phase diagram of helices with r = 0.2 and p = 2 to 8. In addition to isotropic, nematic and smectic phases we see screw-nematic phase in this case. In the phase diagram, region plotted with solid squares represent total nematic region $(N + N_S^*)$ where red squares represent N_S^* phase and blue squares represent the conventional N phase. The red and blue shades in this region separate conventional N to N_S^* phase. The phase behaviour is consistent with what we have already discussed about $r = 0.2$ and $p = 3$, 6 and 8 cases in the section 5.5.1. The N_S^* phase is always observed at the higher end of the nematic region. In all cases we observe a first order

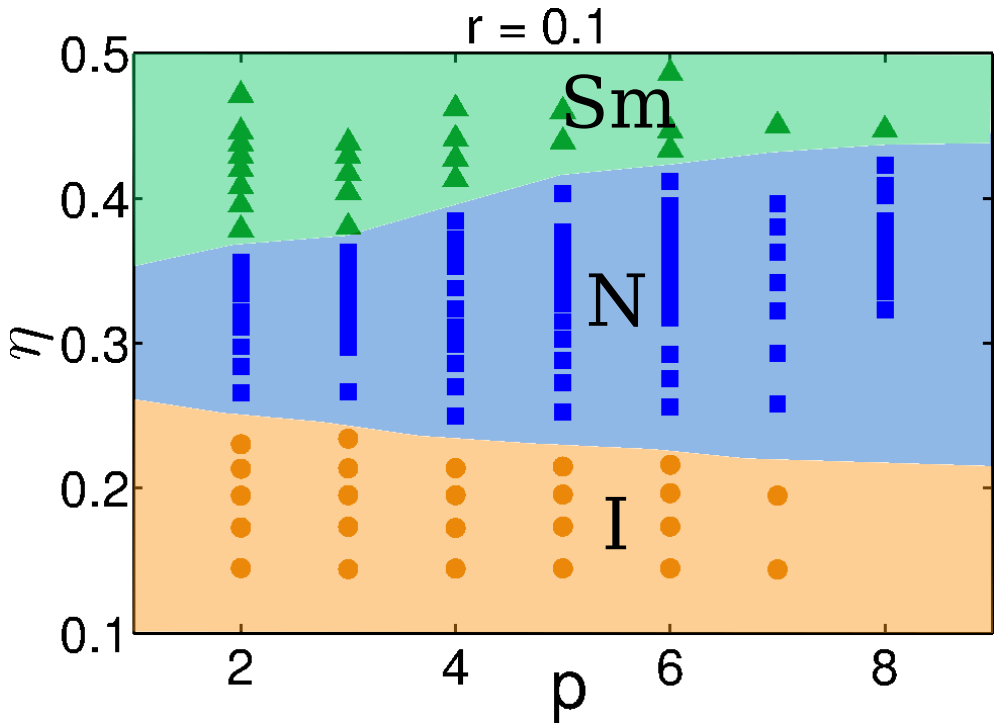

FIGURE 5.23: Phase digram plotted as η *Vs* pitch for helices having r = 0.1 and p = 2 to 8. circles indicate isotropic; Squares indicate nematic; triangles indicate smectic and other higher density phases. Shaded regions are rough estimates of the width of the phases.

IN transition, a second order $N - N_S^*$ transition and a continuous or a weak first order $N_S^* - Sm$ transition with the increasing η.

In this case, we can see a marked difference with the phase diagram of spherocylinders. Increasing radius brings the desired curliness in helical shape to develop screw-like order at higher densities. From the figure we can say, nematic phase tends to stabilize more with increase in pitch which is due to the increase in aspect ratio. But the N_S^* tends to stabilize more at lower pitch values. We can justify this by looking at shapes with r = 0.2 in the the figure 5.22. Because of the increased curliness in shape, particles with lower pitch values are more prone to the interlocking of the grooves at higher densities.

Phase diagram for r = 0.3

Figure 5.24 shows the computed phase diagram of helices with r = 0.3 and p = 2 to 8. Increasing the radius to 0.3 further increases the curliness and decreases the aspect ratio showing an interesting phase behaviour. The phases obtained are the result of a trade off between aspect ratio and the helical shape.

In this case we notice the smectic phase is preceded by nematic phase at lower pitch value. It is evident from the phase diagram of spherocylinder shown in the chapter 1 that smectic phase is the first to become stable with increasing aspect ratio. Helices

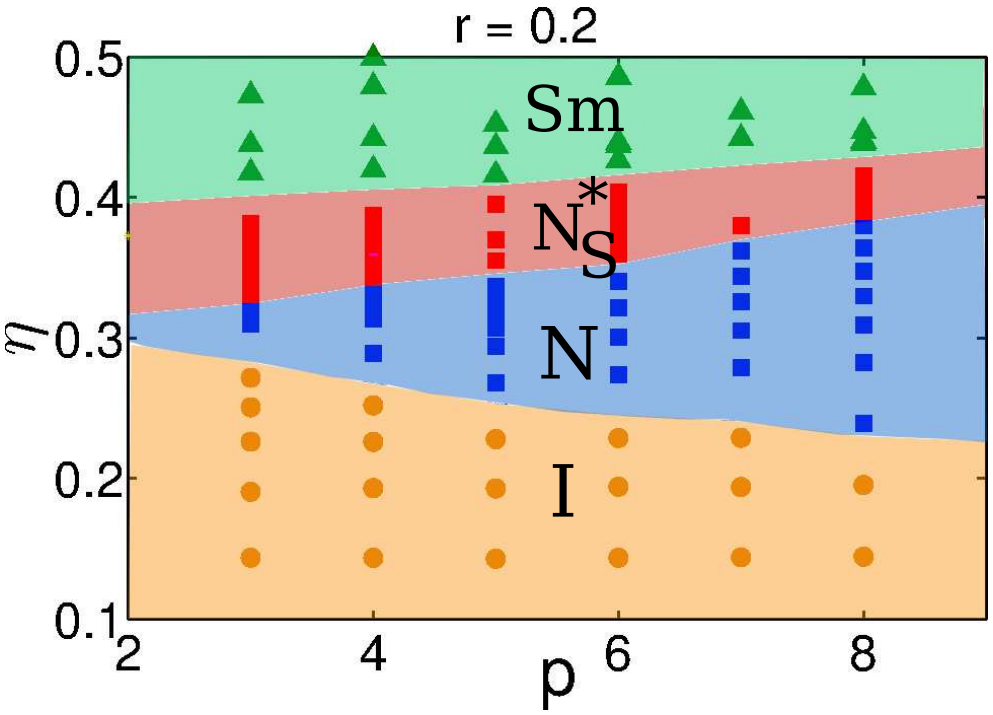

FIGURE 5.24: Phase digram plotted as η *Vs* pitch for helices having $r = 0.2$ and $p = 2$ to 8. Yellow circles indicate isotropic; Blue squares indicate nematic; Red squares indicate screw nematic; triangles indicate smectic and other higher density phases.

having $r = 0.3$ and $p = 2$ are short and cylindrical particles, making the helical shape less significant. For this particular case we see a direct first order isotropic - smectic transition. Depending on the pitch value, we see a I-Sm or IN or $I - N_S^*$ transition.

With our model, we always see N_S^* preceded by N with increasing aspect ratio. In case of spherocylinders, a $I - N - Sm$ triple point is found for the aspect ratio at L/D ≈ 3.7. In case of helices we can say that I-N-Sm triple point does not exit and there is a chance of having $I - N_S^* - Sm$ triple point at aspect ratio ≈ 5.0 and a $I - N - N_S^*$ tricritical point at aspect ratio ≈ 6.5. For intermediate pitches like 3, 4 and 5 we see $I - N_S^*$ ans $N_S^* - Sm$ transition. For pitches greater than 6, we I-N, $N - N_S^*$ and $N_S^* - Sm$ transitions.

Phase diagram for $r = 0.4$

Figure 5.26 shows the computed phase diagram of helices with $r = 0.4$ and p = 2 to 8. The phase behaviour is similar to the case with $r = 0.3$. The N_S^* region widens and the conventional nematic region shrinks compared to the phase diagram for r =0.3.

5.6 Conclusions

We found a new chiral phase called as 'screw nematic phase' for the systems of hard helical particles. We found a second order transition from conventional N to screw

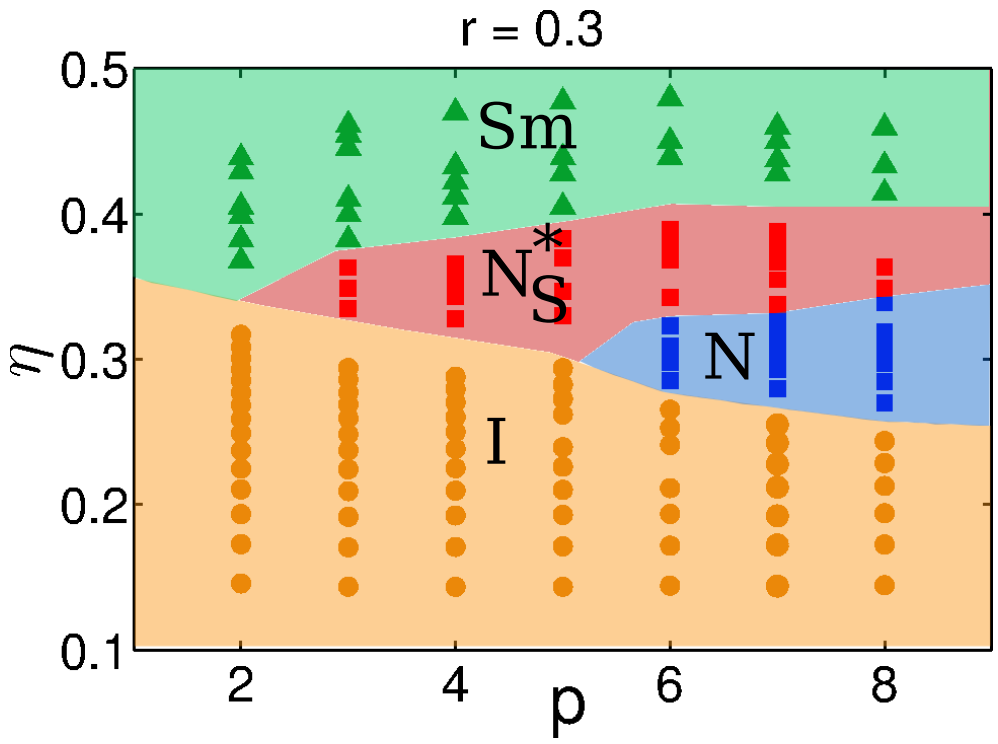

FIGURE 5.25: Phase digram plotted as η *Vs* pitch for helices having $r = 0.3$ and $p = 2$ to 8. Yellow circles indicate isotropic; Blue squares indicate nematic; Red squares indicate screw nematic; triangles indicate smectic and other higher density phases.

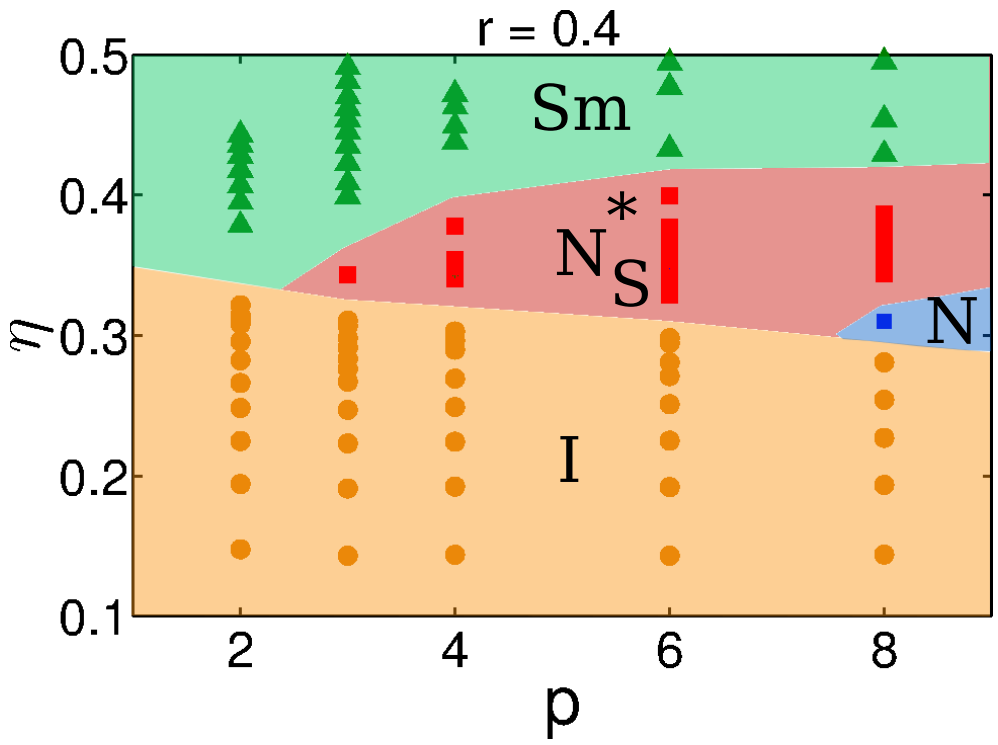

FIGURE 5.26: Phase digram plotted as η *Vs* pitch for helices having $r = 0.4$ and $p = 2$ to 8.

nematic N_S^* and a first order transition from an isotropic phase to N_S^* phase. This phase is peculiar to the helical shape and different to cholesteric phase. In principle these two phases could coexist and investigating their compatibility is our current interest. Phase diagrams showing isotropic, nematic and screw nematic phases are obtained for different shape. The effect of the radius and the pitch on screw-like order in nematic phase is clearly explained. Our results provide a theoretical explanation of $I - N_s^*$ transition observed in helical flagella. Our results raise the question of existence of this phase in other helical systems like concentrated DNA and helical polymers

Chapter 6

Characterization of the smectic phases of hard helices

6.1 Introduction

Particles with shape anisotropy exhibit rich phase behaviour at high densities. There are various smectic mesophases exhibited by particles with different shapes and interactions. Some common smectic types are mentioned in chapter 1. One of the remarkable phenomena observed in 1980's is the spontaneous formation of smectic phases by colloidal mono disperse rod-like particles spontaneously [75–77]. In any smectic phase, the density of particles is periodic in one dimension, parallel(tilted) to the principal direction of particle orientation. The loss of entropy occurring due to this partial positional ordering in smectic phases is compensated by the the loss in excluded volume. The emblematic example for computer simulations is the system of hard spherocylinders which shows smectic phase. First numerical evidence was provided by Frenkel et al.[78], showing that hard spherocylinders can form stable smectic phases spontaneously. Here entropy, stemming from hard-core interactions, alone is sufficient to drive the system to attain smectic order. Studies indicate nematic to smectic transition for rod like particles of any aspect ratio[79] is first order.

There are experimental findings on smectic phases exhibited by helical particles like semi flexible monodisperse *fd* viruses[32], single handed helical polymers[80] etc. All these particles are mono-disperse enough to form stable smectic phases. A solution of virus particles showing smectic phase, is the only experimentally investigated system dominated by repulsive interactions, that we can compare with the simulation of hard helices. There is considerable deviation in the N-Sm coexistence concentration and the layer spacing is found to be higher in case of simulations. Recent studies show that semi

flexible viruses form smectic B and columnar phases [29] at high densities which are not seen in hard-rods case. So studying the effects of helical shape on smectic order has its own significance.

In this chapter, I present the types of smectic phases that are observed in the system of helical particles. The main focus is laid on the propagation of screw-like order into smectic phases and its dependence on the shape of the helix. In section 6.2, different order parameters and correlation functions that are used to distinguish liquid crystal phases at higher densities are discussed. In section 6.3, types of smectic phases and their unconventional features are explained. Major part of the results section is dedicated to the explanation of the phase behaviour of three different helical shapes, going from the straightest helix to the curliest helix. This is done by showing phases in the equation of state curve and corresponding order parameters and correlation functions [72]. Finally combining all the results obtained, full phase diagrams are shown in case of r = 0.1, 0.2 and 0.4.

6.2 Order parameters and correlation functions to characterize higher density phases

In addition to the order parameters $\langle P_2 \rangle$ and $\langle P_{1,c} \rangle$ discussed in chapter 5, we need other order parameters to fully characterize higher density phases. The smectic order in the system is obtained by computing one dimensional translational order parameter τ_1. The hexagonal ordering is found by using six fold bond orientational order parameter ψ_6 and the crystal like organization is shown by Q_4 and Q_6 bond order parameters.

6.2.1 smectic order parameter

The calculation of smectic order [6] [74] is not a trivial task in the simulation especially when the system to close to the nematic to smectic transition. The one dimensional translational order [81] [82] is given by

$$\tau_1 = \int \rho(z^*) \cos(2\pi(z^*/d))\, dz \tag{6.1}$$

where z^* is the position coordinate along the direction normal to the layers $\hat{L}$, $\rho(z^*)$ is the singlet translation distribution function and d is the layer spacing. The order parameter has to be calculated in the coordinate frame with z-axis parallel to ffl$\hat{L}$. In case of smectic A and smectic B, $\hat{\mathbf{L}}$ is same as nematic director $\hat{n}$. Where as in tilted

phases like smectic C $\hat{\mathbf{L}}$ makes some some angle with $\hat{\mathbf{n}}$. Eq.6.1 can be calculated if the $\rho(z^*)$ is known as layer spacing can also be obtained form $\rho(z^*)$. But the positions of the particles and thus positions of layers are always changing during the course of the simulation making it difficult to find $\rho(z^*)$. These changes are more profound when the system is close to the transition. The other problem involved here is the ambiguity in the choice of the origin to find z^*. These problems can be overcome by considering general expression which is given by

$$\langle \tau_1 \rangle = |\langle \exp(2\pi i(z^*/d)) \rangle| \tag{6.2}$$

However eq.6.2 [83] [84] still has the disadvantage of requiring the prior knowledge of d. This is solved by computing τ_1 for different values of d and determining the d value that maximizes τ_1. The maximum τ_1 value is the smectic order parameter and the value of d which maximizes is the actual layer spacing. This order parameter is close to unity in case of perfect layering and close to zero in case of I, N and N_S^* phases.

Figure 6.1 shows τ_1 plotted as a function of d calculated at different η for helices with r = 0.2 and p = 4. The black line in the figure, with no peak, corresponds to N_S^* phase at $\eta = 0.370$. The blue, red and green lines, showing peaks, correspond to smectic phase and are in the order of increasing η. The maximum values of peaks are their corresponding smectic order parameters. With increase in η, the order parameter increases and corresponding layer spacing value decreases.

6.2.2 Hexatic order parameter

The positional ordering in each layer is analysed by calculating the six fold bond-orientational (hexatic) order parameter $\langle \psi_6 \rangle$ [83] [85].

$$\langle \psi_6 \rangle = \left\langle \frac{1}{N} \sum_{i=1}^{N} \left| \frac{1}{n(i)} \sum_{j=1}^{n(i)} \exp\left(6i\theta_{ij}\right) \right| \right\rangle \tag{6.3}$$

Here $n(i)$ is the number of nearest neighbours of molecule i with in a single layer. where θ_{ij} is the angle between vector $\tilde{r}_{ij}$ and a random fixed reference axis in plane perpendicular to layer normal $\hat{\mathbf{L}}$. As shown in the eq 6.4, $\tilde{r}_{ij}$ is defined as vector parallel to the projection of the unit vector $\hat{\mathbf{r}}_{ij}$ into the plane perpendicular to the layer normal $\hat{\mathbf{L}}$. Only nearest neighbour molecules are considered as i and j in the equation.

$$\tilde{r}_{ij} = \hat{\mathbf{r}}_{ij} - (\hat{\mathbf{r}}_{ij}.\hat{\mathbf{L}}).\hat{\mathbf{L}} \tag{6.4}$$

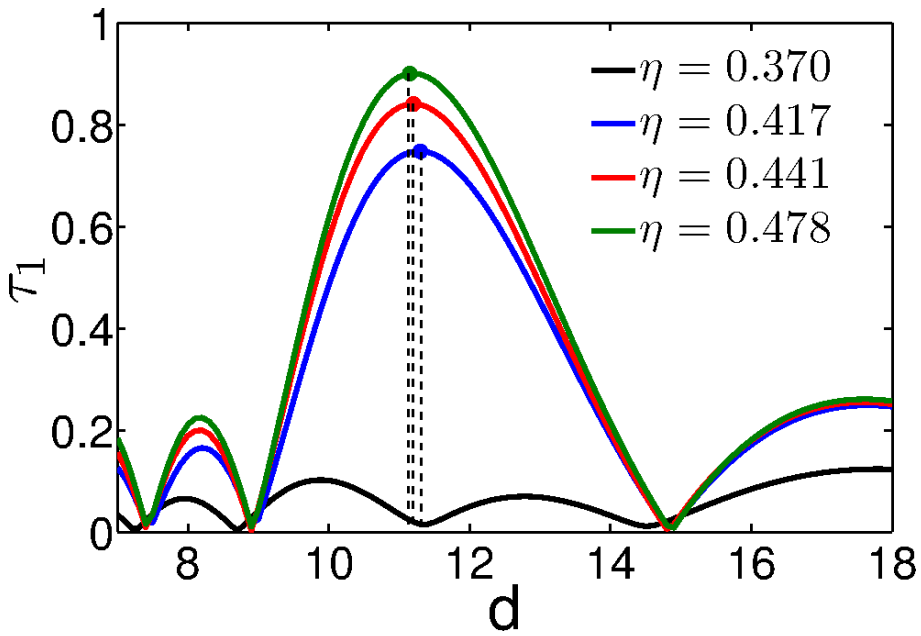

FIGURE 6.1: The dependence of translational order parameter $\langle \tau_1 \rangle$ on layer spacing for helices having $r = 0.2$, $p = 4$ is shown on either side of $N_S^* - Sm_A$ transition. The maximum value of τ_1 is the smectic order parameter.

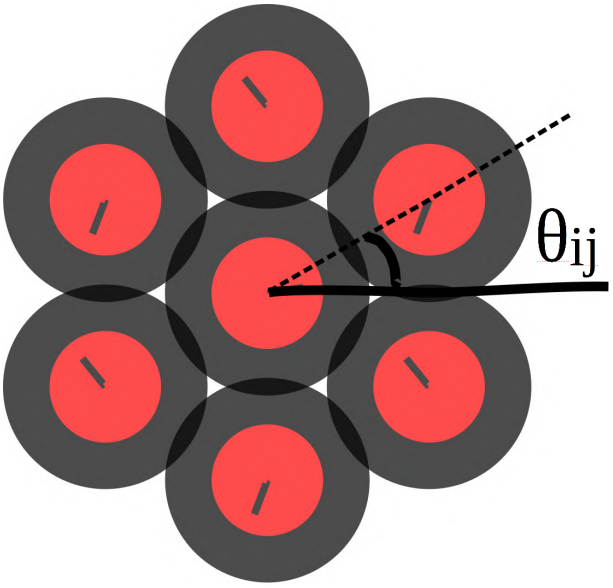

FIGURE 6.2: Figure showing how the line (dashed line) joining the nearest neighbour helices making an angle θ_{ij} with reference axis(solid line). Helices are projected on to a plane. Red circle denotes the radius of the helix. The short axis inside each circle is the fixed C_2 axis indicating the orientation of helix

Figure 6.2 shows the bond angle θ_{ij} between the line joining nearest neighbours (dashed line) and the reference axis (solid line) in the plane perpendicular to $\hat{\mathbf{L}}$. Projection of helices is shown following the same convention used in 4.

This $\langle \psi_6 \rangle$ order parameter helps to probe the onset of the hexatic order in the system.

This value is close to 1 incase of perfect hexagonal ordering and close to zero in the absence of hexagonal ordering with in the vicinity of nearest neighbour distance mentioned. Hexatic order is further supported by computing average number of nearest neighbours $\langle n \rangle$ with in each layer. This quantity is computed by taking the number of nearest neighbours for all helices in plane and averaging it overall configurations. This value tends to 6 in perfect hexagonal ordering. However both ψ_6 and $\langle n \rangle$ are very sensitive to the definition of the nearest neighbour distance. Nearest neighbour distance is decided from the first peak position of radial distribution function. Both $\langle \psi_6 \rangle$, $\langle n \rangle$ are consistent in displaying the hexatic order for different layers. The results shown for hexatic order are calculated for a single layer.

6.2.3 Q_4 and Q_6 bond order parameters

A family of local and global bond orientation order parameters are proposed by Steinhardt et al.[86] in 1983. These order parameters are commonly used to detect the crystal nucleus and characterization of its structure. They are useful in studying melting transitions, colloidal fluid-solid interfaces, glass transitions and crystalline clusters. The vector joining a pair of nearest neighbours is considered as bond. The idea is to quantify the spatial arrangement of nearest neighbours around a central particle. One can compute local q_l and global Q_l bond order parameters. The local order parameter gives the information about the local arrangement about each particle which is useful in studying liquids. The average of the local order of all particles gives global order which is an indicative of long range positional correlation.

These order parameters are based on the spherical harmonic functions $Y_{lm}(\theta, \phi)$ and therefore can be taken upto any number. Only few out of many possibilities are considered depending on the material of interest. The local bond order of particle i is given by

$$q_{lm}(i) \equiv \frac{1}{N_a(i)} \sum_{j=1}^{N_a(i)} Y_{lm(\hat{r}_{ij})} \tag{6.5}$$

where $\hat{r}_{ij}$ specifies the direction of the bond r_{ij}, $N_a(i)$ is the number of nearest neighbours of particle i and $Y_{lm}(\hat{\mathbf{r}}_{ij}) \equiv Y_{lm}(\theta_{ij}, \phi_{ij})$.By taking average of local bond order over all N particles, we get global bond bond order parameter Q_{lm}.

$$Q_{lm} \equiv \frac{\sum_{i=1}^{N} N_a(i) q_{lm}(i)}{\sum_{i=1}^{N} N_a(i)} \tag{6.6}$$

Inorder to measure the structure without any bond orientational dependence, rotational invariants are calculated.

$$Q_l(i) \equiv \sqrt{\frac{4\pi}{2l+1} \sum_{m=-l}^{l} |Q_{lm}|^2} \tag{6.7}$$

The local bond order parameter q_l is non-zero in both solid-like and liquid like states. Where as the global order parameter Q_l remains close to zero in liquids and non-zero in solids.

The idea of the bond order parameters is to capture the symmetry of bond orientations regardless of the bond lengths. A bond is defined as the vector joining a pair of neighboring atoms. The local order parameters associated with a bond are the set of numbers

$$Q_{lm}(R) \equiv Y_{lm}(\theta(R), \phi(R)) \tag{6.8}$$

where $\theta(R)$ and $\phi(R)$ are the polar and azimuthal angles of the bond with respect to an arbitrary but fixed reference frame, and $Y_{lm}(\theta(R), \phi(R))$are the usual spherical harmonics

$$Q_{lm} \equiv \frac{1}{N_b} \sum_{bonds} Q_{lm}(R) \tag{6.9}$$

where N_b is the number of bonds. To make the order parameters invariant with respect to rotations of the reference frame, the second-order invariants are defined as

$$Q_l = \sqrt{\frac{4\pi}{2l+1}} \sum_{m=-l}^{l} |Q_{lm}|^2 \tag{6.10}$$

The Q_4 and Q_6 bond order parameters are generally sufficient to identify different crystal structures. Characterization of the crystalline structures of helical particles is not simple because of their non-convex shape. The method of bond-orientational order parameters is used in case of simple systems like spherical molecules. Due to the shape anisotropy of hard helices we cannot implement this method directly to the current system. So we attempt to find the inplane order using bond order parameters neglecting the details of intralayer arrangement. Here the neighbouring helices are those lying in the same plane having distance less than or equal to the first minimum of the pair correlation function which is ≈1.8D.

6.2.4 Parallel and perpendicular pair correlation functions

We measure pair correlation function as a function of particle separation to get an insight into the structure of phase in planes parallel and perpendicular to the director($\hat{n}$). The perpendicular correlation function $g_{\perp}(R_{\perp})$ gives the probability of finding a particle at a distance of $R_{\perp}$, when projected onto a plane perpendicular to the director [87].

$$g_{\perp}(R_{\perp}) = \frac{1}{2\pi R_{\perp} N} \left\langle \frac{1}{\rho L_z} \sum_{i=1}^{N} \sum_{j \neq i}^{N} \delta(R_{\perp} - |R_{ij} \times \hat{n}|) \right\rangle \tag{6.11}$$

where N is the total number of particles, ρ is the number density, L_z is the length of the simulation box along the director $\hat{\mathbf{n}}$. Note that the number density is taken inside the average as the volume of the box changes in the course of simulation.

The structure of the phase parallel to the director is analysed by measuring $g_{\parallel}(R_{\parallel})$. The parallel positional correlation function $g_{\parallel}(R_{\parallel})$ gives the probability of finding a particle at a distance of $R_{\parallel}$, when projected onto a plane parallel to the director. More details on correlation functions are given in Appendix D.

$$g_{\parallel}(R_{\parallel}) = \frac{1}{N} \left\langle \frac{1}{\rho L_x L_y} \sum_{i=1}^{N} \sum_{j \neq i}^{N} \delta(R_{\parallel} - R_{ij}.\hat{n}) \right\rangle \tag{6.12}$$

where L_x and L_y are the dimensions of the simulation box mutually orthogonal to the director. δ is the Dirac δ function and R_{ij} is the vector joining the centres of helices i and j. Peaks in $g_{\parallel}(R_{\parallel})$ suggest layers in the structure. Both these correlation functions help to distinguish Isotropic and Nematic (both correlation functions are liquid like); Smectic (peaks in $g_{\parallel}(R_{\parallel})$, $g_{\perp}(R_{\perp})$ liquid like); columnar (absence of peaks in $g_{\parallel}(R_{\parallel})$ and $g_{\perp}(R_{\perp})$ solid like); crystal (both $g_{\parallel}(R_{\parallel})$ and $g_{\perp}(R_{\perp})$ solid like). In addition to these, $g^{\hat{\mathbf{w}}}_{1,\parallel}(R_{\parallel})$ discussed in Chapter 3 is used to identify screw-like order.

6.3 Types of smectic phases observed

Depending on the shape of the helical particle and the density of the system, we see mainly three different arrangements in smectic region. Each case is explained in detail by discussing various order parameters and correlation functions.

6.3.0.1 smectic A with screw like order ($Sm^*_{A,S}$)

The screw-like order combined with the layer ordering results in a new chiral smectic phase. This smectic phase is characterized by random positional ordering inside the layer along with screw like order. This phase can be distinguished with the help of order parameters τ_1 and $\langle P_{1,c}\rangle$. Additional insight is obtained by looking at the snapshots and the correlation functions $g^{\hat{\mathbf{w}}}_{1,||}(R_{||})$, $g_{||}(R_{||}$ and $g_{\perp}(R_{\perp})$. This phase is globally uniaxial with main director perpendicular to the layers and generally preceded by screw nematic.

6.3.0.2 smectic B with screw like order ($Sm^*_{B,S}$)

This phase is characterized by the hexagonal positional order with in the layer along with screw like order. The phase is exhibited by those helices having significant twist in their helical shape. Depending on the shape of the helix, we see transition form $Sm^*_{A,S}$ to $Sm^*_{B,S}$ or N^*_S to $Sm^*_{B,S}$. This phase can be distinguished with the help of order parameters $\langle\psi_6\rangle$, τ_1, and $\langle P_{1,c}\rangle$ and correlation functions $g^{\hat{w}}_{1,||}(R_{||})$, $g_{||}(R_{||}$ and $g_{\perp}(R_{\perp})$.

6.3.0.3 smectic B with polar order ($Sm_{B,P}$)

This smectic phase is characterized by a hexagonal positional order with in the layer along with polar order in each layer. In this phase, screw like order is absent. Each layer possess hexagonal arrangement and behaves independently. Polar order develops with C_2 axis of all particles pointing in the same direction. This essential difference between the structure of the $Sm^*_{B,S}$ and the $Sm^*_{B,p}$ phase is summarized in the figure 6.3. While in $Sm^*_{B,s}$, helices are azimuthally correlated within each plane and screw-like correlated between different planes, in $Sm_{B,p}$ phase only intra plane azimuthal correlation is present, with different layers being uncorrelated both positionally and orientationally.

6.4 Results and Discussion

I present the equation of states for three different helices going from a straightest to a curliest helical shape, explaining the onset of the screw like ordering at higher densities for each case. In section 6.4.4, I present the full phase diagrams of helices with $r = 0.1$, 0.2 and 0.4.

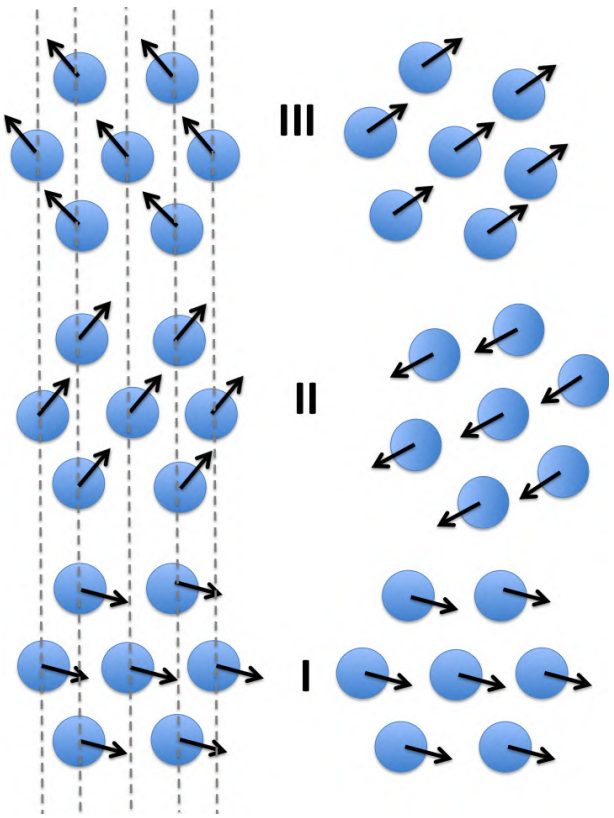

FIGURE 6.3: Cartoon of the smectic B phases discussed in the text. Circles represent transversal sections through the center of helices and arrows the corresponding $\hat{\mathbf{w}}$ vectors. I, II, III indicate adjacent layers. Left: $Sm^*_{B,S}$ phase, with through-layers positional correlation (AAA strucutre, highlighted by the dashed lines and screw like orientational correlation of $\hat{\mathbf{w}}$ vectors. Right: $Sm_{B,p}$ phase, with in-layer correlation of $\hat{\mathbf{w}}$ vectors and neither positional nor orientational correlation between layers.

6.4.1 Equation of state for r = 0.2, p = 8

Helix with r = 0.2, p = 8 is the straightest one with still having effective curliness to account for screw like order. Figure 6.4 shows the equation of state of this system in reduced pressure P^* versus η plane. Different order parameters and correlation functions are used to distinguish the phases as explained in section 6.3. Different phases are shown using different colours. The same colour convention is followed in showing all order parameters. We see I,N,N^*_S,$Sm^*_{A,S}$,$Sm_{B,p}$ and crystal-like structures with increase in η.

$I - N$ and $N - N^*_S$ transition

The onset of nematic ordering and screw-like Nematic ordering is signalled by a jump in nematic order parameter $\langle P_2 \rangle$ at $\eta \approx 0.23$ and screw-like order parameter $\langle P_{1,C} \rangle$ at $\eta \approx 0.4$ as shown in figures 6.5 and 6.6. These transitions are discussed in detail in Chapter5.

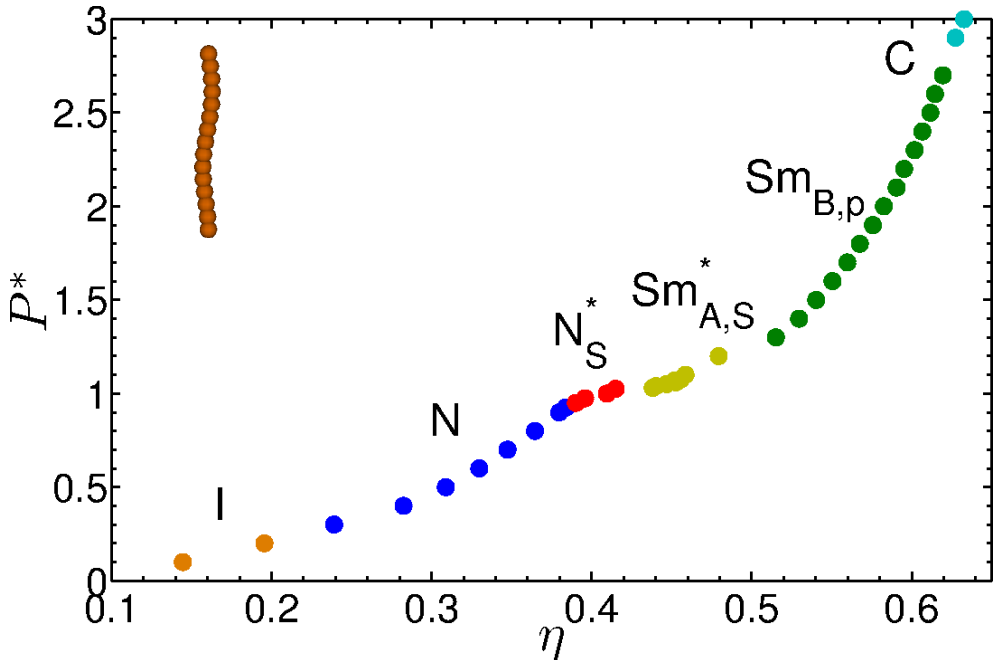

FIGURE 6.4: Equation of state for the system of helices having r = 0.2, p = 8. Different colours indicate different phases. I - isotropic; N - nematic; N_S^* - screw-nematic; $Sm^*_{A,S}$ - screw-smectic A; $Sm_{B,p}$ - polar-smectic B; C - compact phase

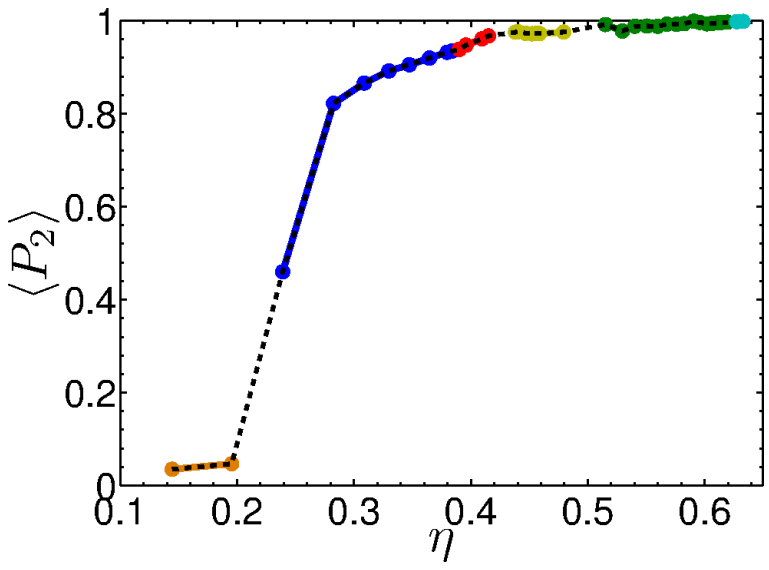

FIGURE 6.5: Nematic order parameter $\langle P_2 \rangle$ as a function of volume fraction η for helices with r = 0.2 and p = 8. Points are plotted in different colours to indicate different phases.

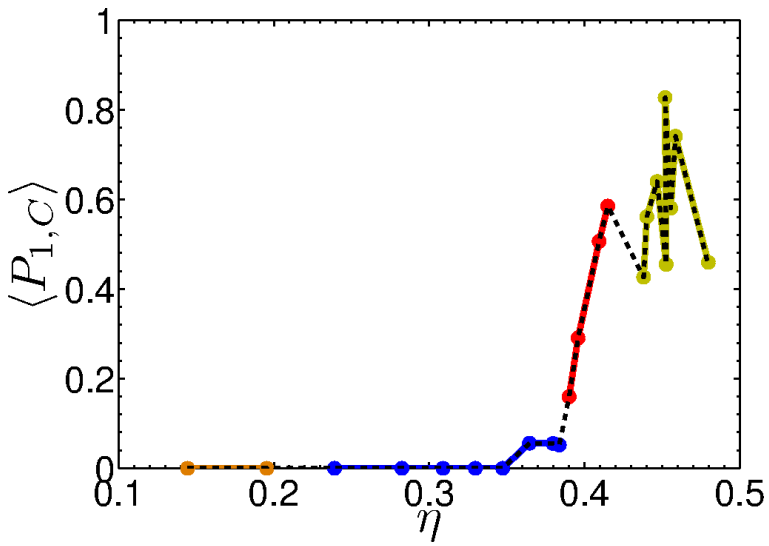

FIGURE 6.6: Screw-like order parameter $\langle P_{1,c} \rangle$ for helices with r = 0.2 and p = 8. Points are plotted in different colours to indicate different phases.

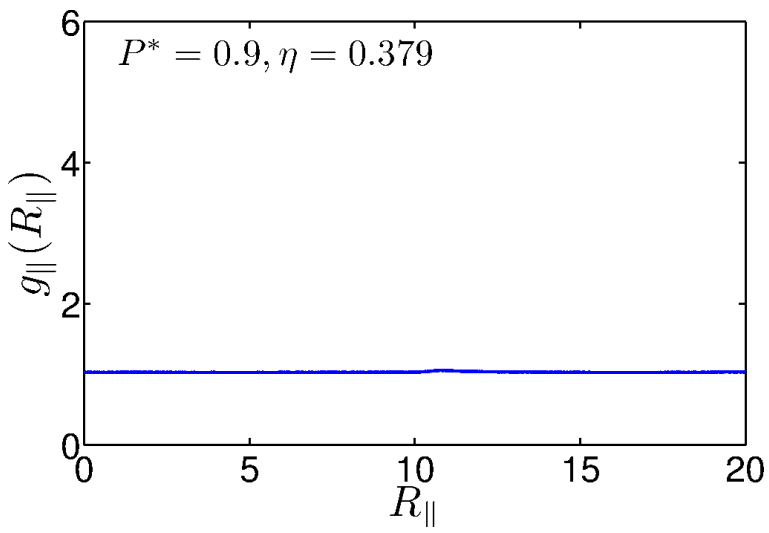

FIGURE 6.7: The parallel correlation function $g_{\parallel}(R_{\parallel})$ for helices with r = 0.2 and p = 8, calculated at $\eta = 0.375$, $P^* = 0.9$ in Nematic phase.

The correlation functions $g_{\parallel}(R_{\parallel})$ and $g^{\hat{\mathbf{w}}}_{1,\parallel}(R_{\parallel})$ at $\eta = 0.379$ are flat (no correlation) as shown in figures 6.7 and 6.8. From these figures it is evident that smectic and screw-like orders are absent at $\eta = 0.379$. Figure 6.12 is the corresponding snapshot(N) coloured according to the local tangent.

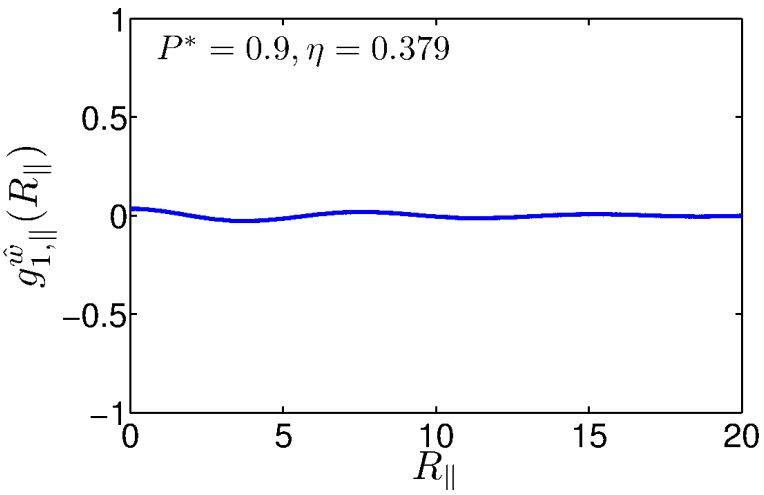

FIGURE 6.8: The screw-like parallel orientational correlation function $g^{\hat{w}}_{1,\|}(R_\|)$ for helices with r = 0.2 and p = 8, calculated at $\eta = 0.379$, $P^* = 0.9$ in Nematic phase, showing no screw like order.

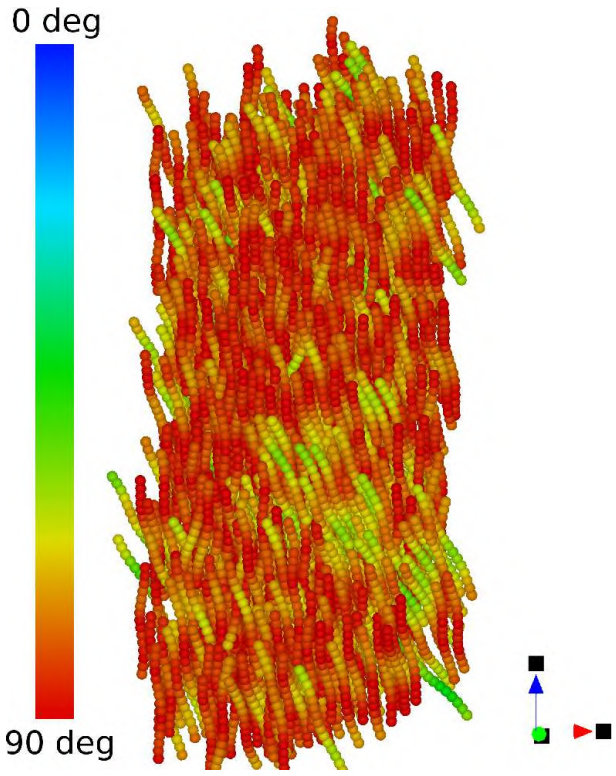

FIGURE 6.9: Snapshot of the system of helices having r = 0.2, p = 8 at $\eta = 0.379$ in nematic phase. The colouring is done for each bead of the helix separately according to the local tangent at that bead.

Figures 6.10 and 6.11 show correlation functions $g_\|(R_\|)$ and $g^{\hat{\mathbf{w}}}_{1,\|}(R_\|)$ at $\eta = 0.409$. Figure 6.10 shows very small peaks indicating an incipient smectic order which sets in gradually at higher pressures. These figures confirm screw-like ordering with no perfect layering. Figure 6.12 is the corresponding snapshot(N^*_S) with a hint of colour stripes.

$N^*_S - Sm^*_{A,S}$ **transition**

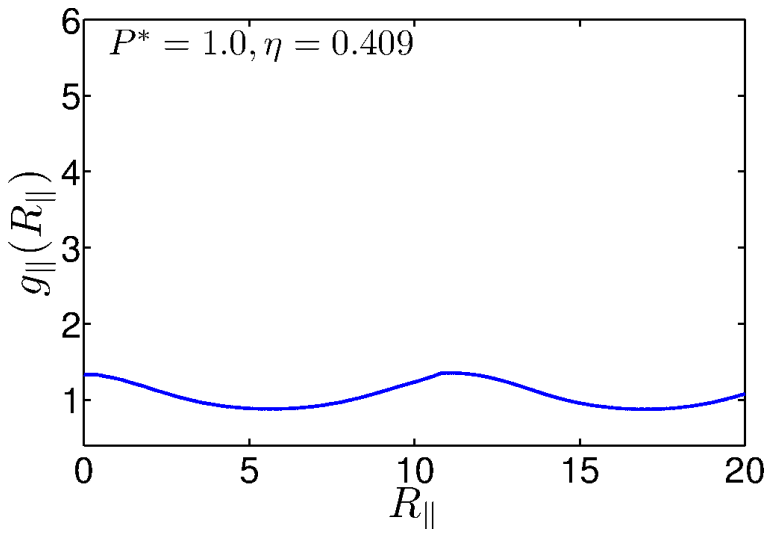

FIGURE 6.10: The parallel correlation function $g_{\|}(R_{\|})$ for helices with r = 0.2 and p = 8, calculated at $\eta = 0.409$, $P^* = 1.0$ in screw-nematic phase.

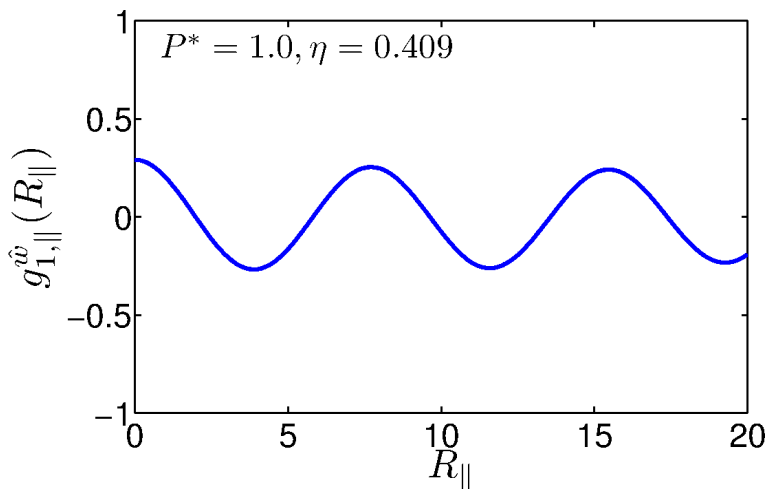

FIGURE 6.11: The screw-like parallel orientational correlation function $g^{\hat{w}}_{1,\|}(R_{\|})$ for helices with r = 0.2 and p = 8, calculated at $\eta = 0.409$, $P^* = 1.0$ in screw-nematic phase

We see a transition from N^*_S to $Sm^*_{A,S}$ at $\eta \approx 0.44$. The onset of smectic ordering is marked by an upswing in τ_1 as shown in figure 6.13. Figure 6.6 illustrates the signature of screw-like ordering in smectic region. The non monotonic behaviour of $P_{1,C}$ after η 0.42 is due to any slight deviation in the periodicity of the screw-like order because of the formation of layers.

Broad peaks at an interval of $R_{\|} \approx 12$ in $g_{\|}(R_{\|})$ correlation function at $\eta = 0.458$, shown in figure 6.14 confirms the smectic order. Here we can notice the periodicity of layers (≈ 12) is slightly higher than the effective length of the helix which is 10.88. This periodicity is different to the periodicity observed in $g^{\hat{w}}_{1,\|}(R_{\|})$ shown in figure 6.15, which corresponds to the helix pitch p = 8. The presence of both periodicities can be seen in the snapshot shown in figure 6.17. Thus the screw like order combines with layering,

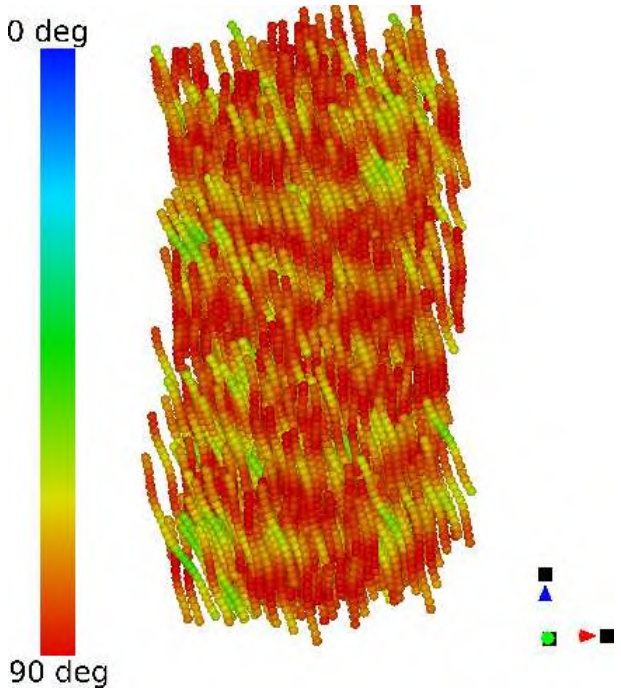

FIGURE 6.12: Snapshot of the system of helices having r = 0.2, p = 8 at $\eta = 0.409$, $P^* = 1.0$ in screw-nematic phase. The colouring is done for each bead of the helix separately according to the local tangent at that bead. Regular colour stripes indicate the phase as special chiral screw-nematic

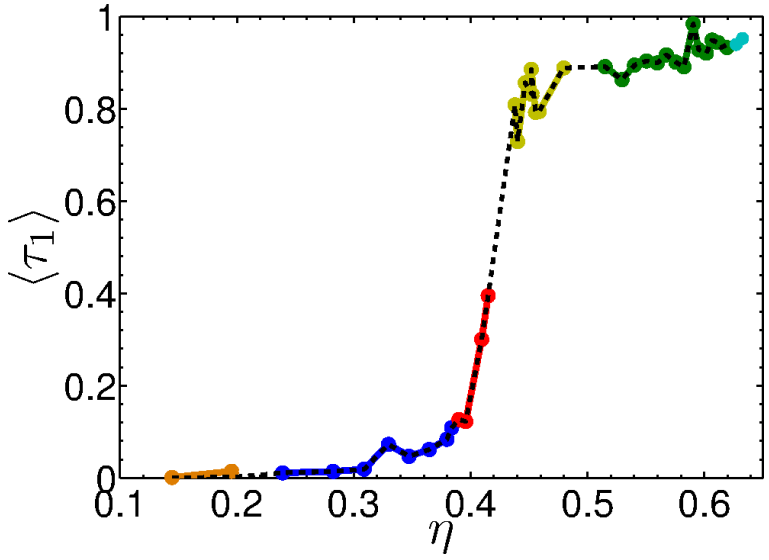

FIGURE 6.13: smectic order parameter $\langle \tau_1 \rangle$ as a function of volume fraction η for helices with r = 0.2 and p = 8. Points are plotted in different colours to indicate different phases.

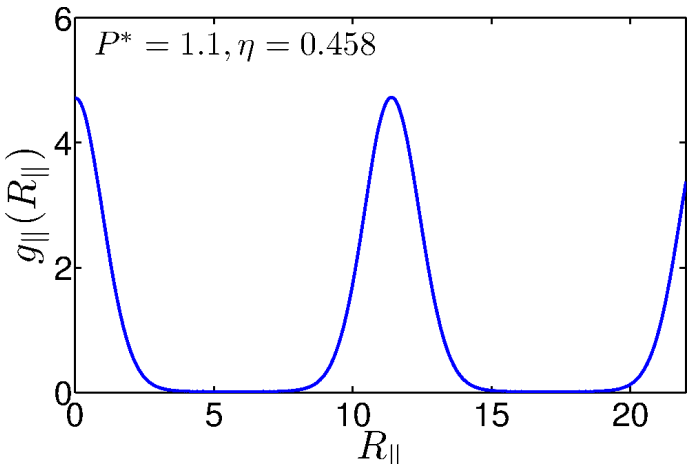

FIGURE 6.14: The parallel correlation function $g_{\|}(R_{\|})$ for helices with r = 0.2 and p = 8, calculated at $\eta = 0.458$, $P^* = 1.1$, in screw-smectic A.

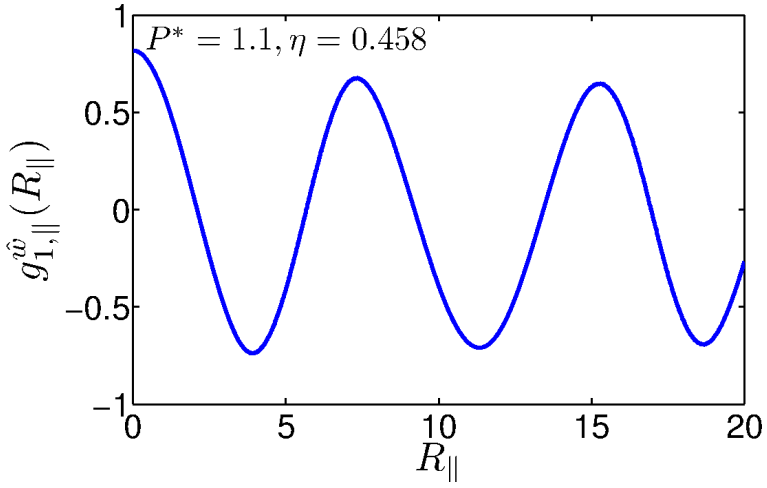

FIGURE 6.15: The screw orientational parallel correlation function $g^{\hat{\mathbf{w}}}_{1,\|}(R_{\|})$ for helices with r = 0.2 and p = 8, calculated at $\eta = 0.458$, $P^* = 1.1$, in screw-smectic A.

giving rise to a new smectic chiral phase. Figure 6.16 shows $g_{\perp}(R_{\perp})$ which indicates liquid like behaviour with in the layer.

$Sm^*_{A,S} - Sm_{B,p}$ transition

At $\eta \approx 0.51$, the correlation function $g_{\perp}(R_{\perp})$ in figure 6.19 provide an indication of translation order . $g_{\perp}(R_{\perp})$ exhibits well developed characteristic double peaked structure, with maximum at $\sqrt{3}\sigma$ and 2σ, σ being the position of the main, nearest-neighbour peak. This indicates that hexatic order sets in with in each single layer. This is further supported by the high value of hexatic order parameter as shown in figure 6.20 and the fact that average number of nearest neighbours $\langle n \rangle$ tends to 6 as shown in figure 6.21. The correlation function $g^{\hat{w}}_{1,\|}(R_{\|})$ in figure 6.18 shows the absence the periodicity equal to helical pitch but shows the presence of azimuthal correlation with in the layer. This

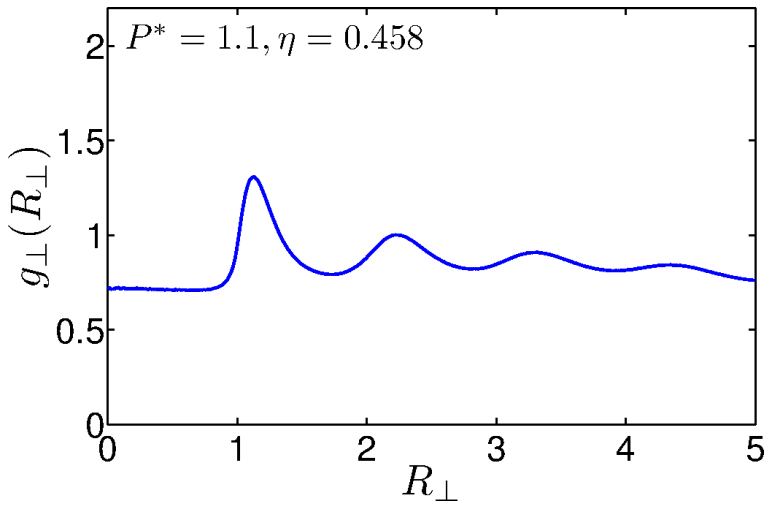

FIGURE 6.16: The perpendicular correlation function $g_\perp(R_\perp)$ for helices with r = 0.2 and p = 8, calculated at $\eta = 0.458$, $P^* = 1.1$, in screw-smectic A.

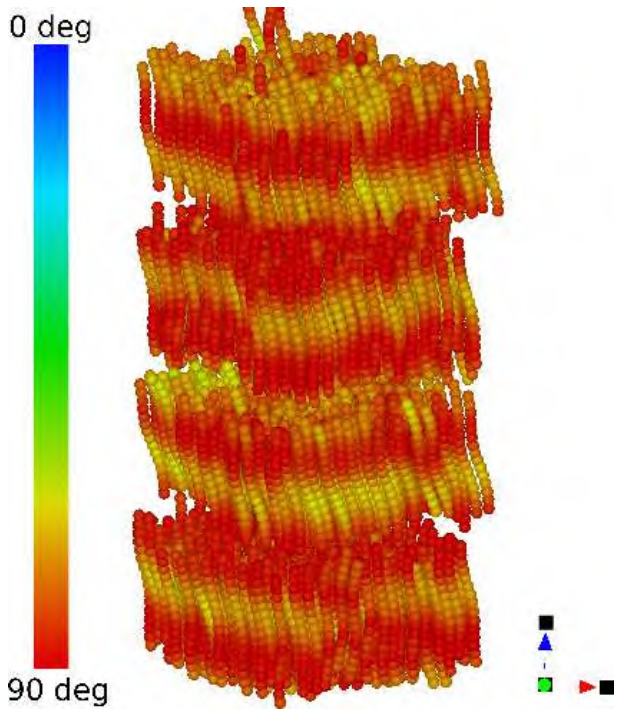

FIGURE 6.17: Snapshot of the system of helices having r = 0.2, p = 8 at $\eta = 0.458$ in screw-smectic A phase. The colouring of beads is done according to the local tangent of the helix.

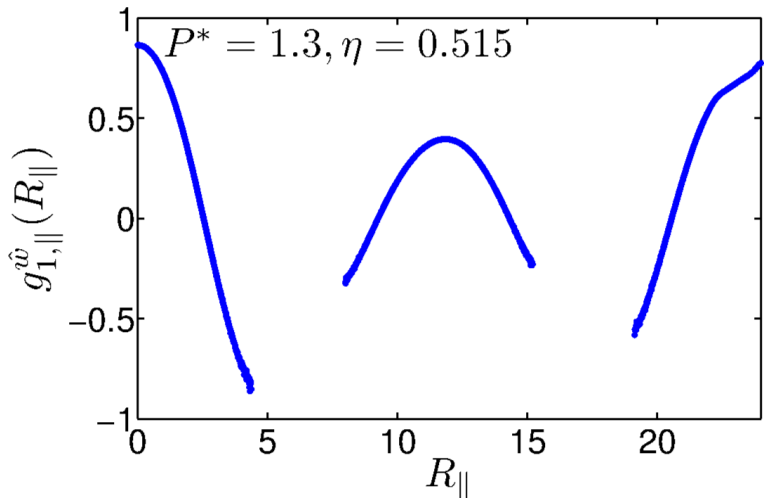

FIGURE 6.18: The screw orientational parallel correlation function $g^{\hat{\mathbf{w}}}_{1,\parallel}(R_\parallel)$ for helices with r = 0.2 and p = 8, calculated at $\eta = 0.515$, $P^* = 1.3$, in polar smectic B.

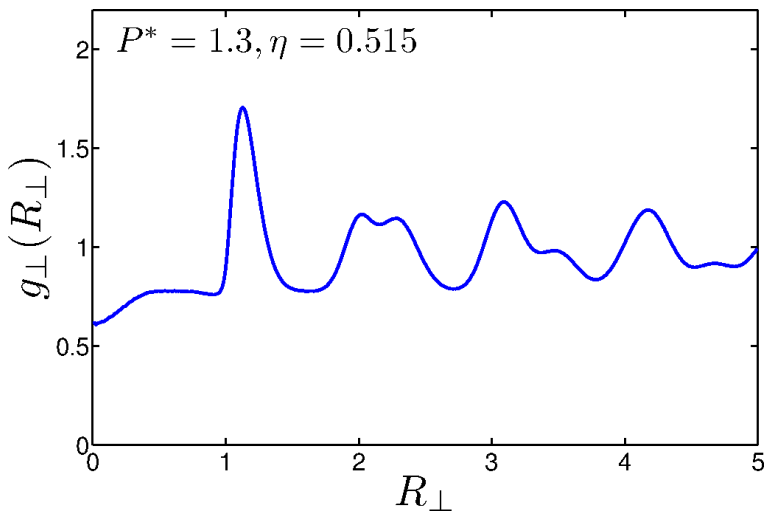

FIGURE 6.19: The perpendicular correlation function $g_\perp(R_\perp)$ for helices with r = 0.2 and p = 8, calculated at $\eta = 0.515$, $P^* = 1.3$, in polar smectic B.

is different to the case shown in $Sm^*_{A,S}$. Here the layers are are uncorrelated from each other, developing polarity with in layers. Note that the gaps in $g^{\hat{w}}_{1,\parallel}(R_\parallel)$ in figure 6.18 are due to the non-availability of particles with those particular $R_\parallel$ values. Snapshots shown in figures 6.22 and 6.33 are in visual support to hexatic order combined with polarity with in layers. Snapshot shown in figure 6.33 is obtained by colouring helices according to the orientation of a fixed C_2 axis.

6.4.2 Equation of state for r = 0.2, p = 4

On increasing the helical twist, unconventional phases become more and more pronounced. By keeping the radius fixed at r = 0.2 and decreasing pitch from 8 to 4, we increase the number of turns in helix from 1.23 to 2.38. The equation of state is

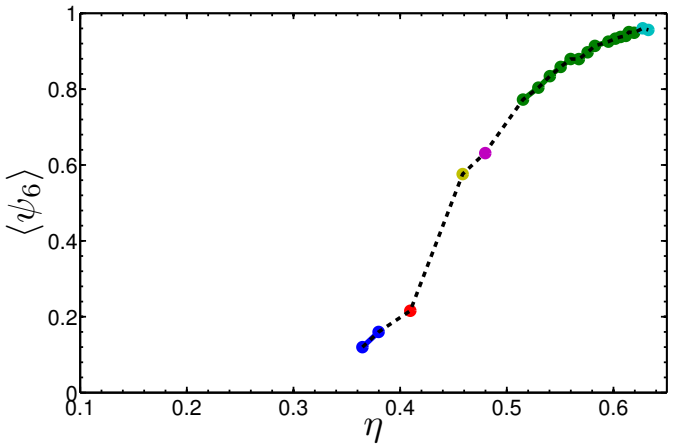

FIGURE 6.20: Hexatic order parameter $\langle\psi_6\rangle$ as a function of volume fraction η for helices with r = 0.2 and p = 8. Points are plotted in different colours to indicate different phases.

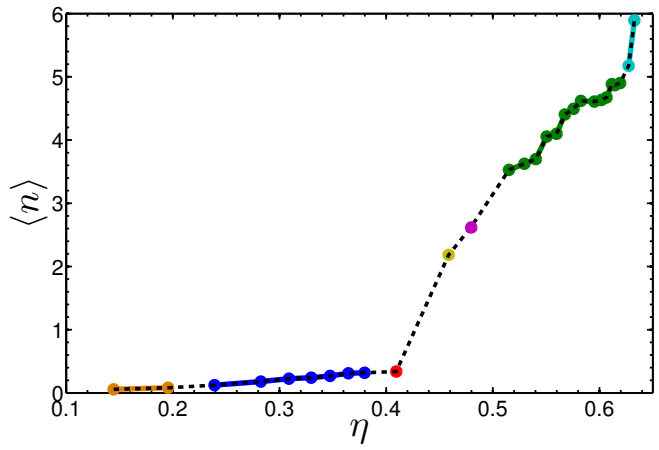

FIGURE 6.21: Average number of nearest neighbours $\langle n\rangle$ as a function of volume fraction η for helices with r = 0.2 and p = 8. Points are plotted in different colours to indicate different phases.

shown in figure 6.26. With increase in η we see I, N, N_S^*, $Sm_{A,S}^*$, $Sm_{B,S}^*$ and crystal like structures. Corresponding orderparameters are reported in figures 6.27 to 6.31.

In this case, also the higher density smectic phases exhibit screw-like order. Figure 6.28 show $P_{1,c}$ being high through out entire smectic region and drops only at the onset of compact phase C. Thus all smectic phases exhibit screw-like order. However SmB is distinguished from SmA by $g_\perp(R_\perp)$ and ψ_6.

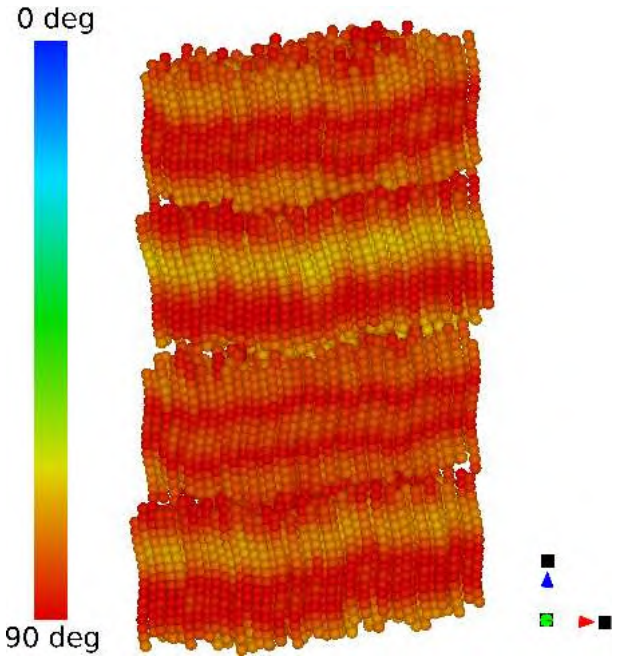

FIGURE 6.22: Snapshot of the system of helices having r = 0.2, p = 8 at $\eta = 0.458$ in screw-smectic A phase. The colouring of beads is done according to the local tangent of the helix.

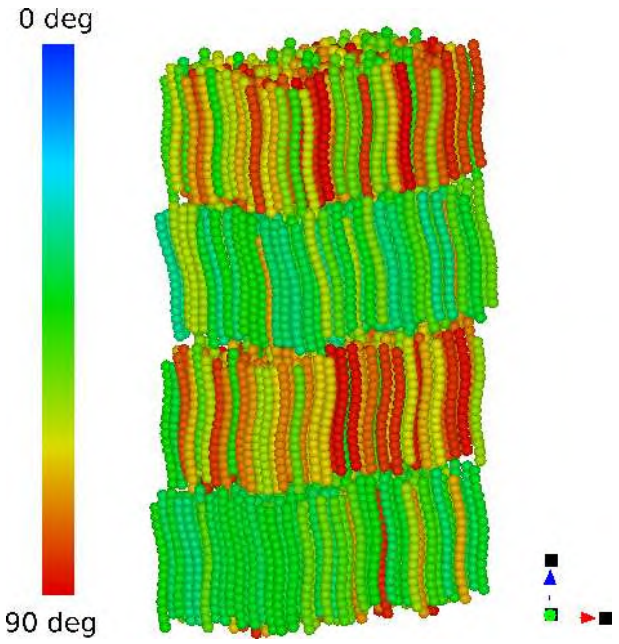

FIGURE 6.23: Snapshot of the system of helices having r = 0.2, p = 8 at $\eta = 0.458$ in polar-smectic B phase. The colouring is done according to the C_2 axes of the helices.

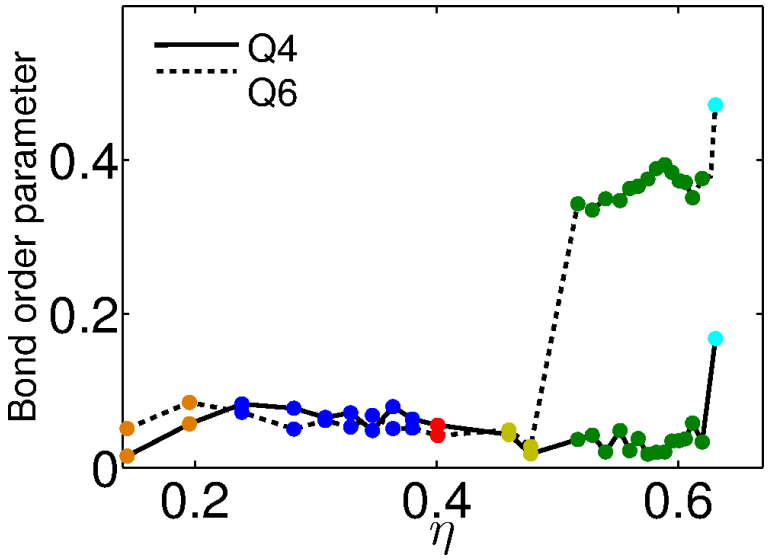

FIGURE 6.24: Q4 and Q6 bond order parameters as a function of volume fraction η for helices with r = 0.2 and p = 8. Points are plotted in different colours to indicate different phases.

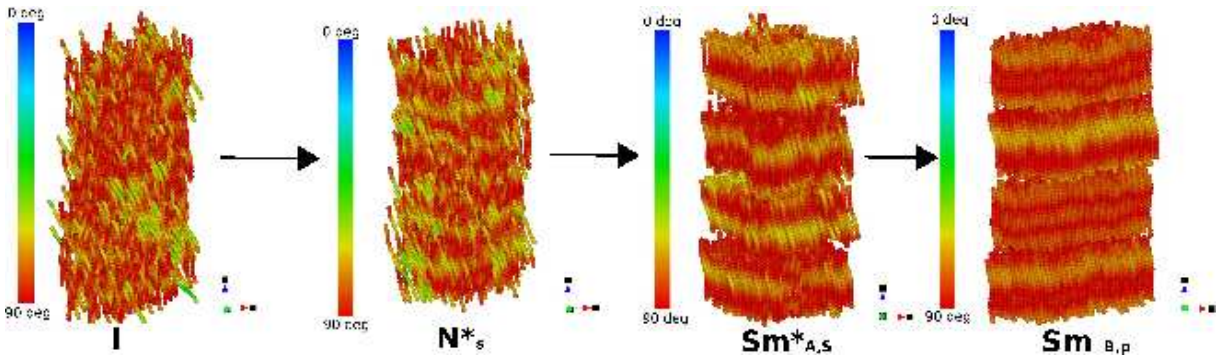

FIGURE 6.25: Figure showing the sequence of phases and their representative snapshots in the case of helices with r = 0.2 and p = 8.

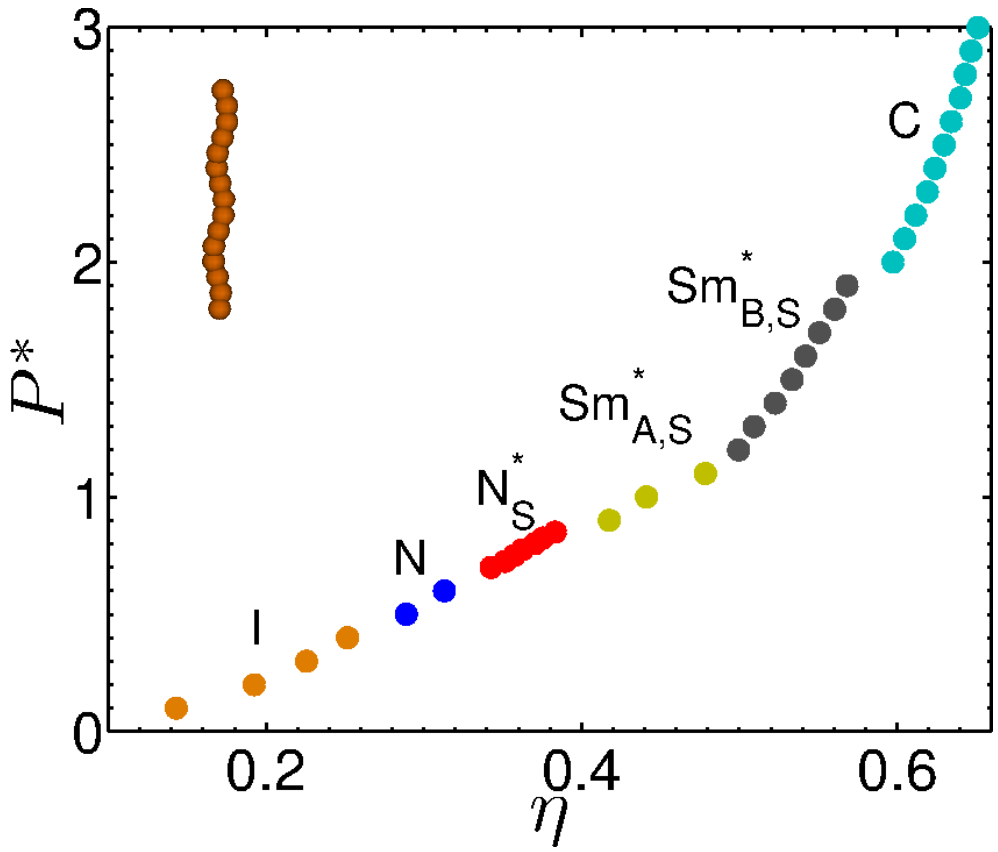

FIGURE 6.26: Equation of state for the system of helices having r = 0.2, p = 4. Different colours indicate different phases. I - isotropic; N - nematic; N^*_S - screw-nematic; $Sm^*_{A,S}$ - screw-smectic; $Sm_{B,S}$ - screw-smectic B; C - compact phase

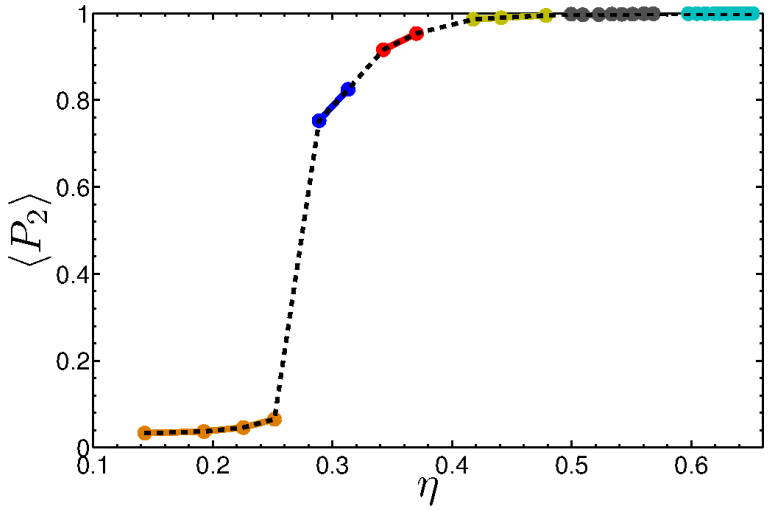

FIGURE 6.27: Nematic order parameter $\langle P_2 \rangle$ as a function of volume fraction η for helices with r = 0.2 and p = 4.

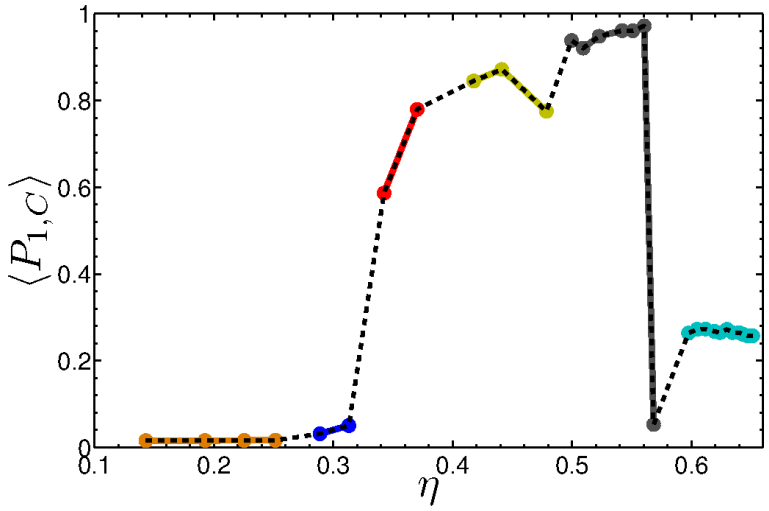

FIGURE 6.28: Screw-like order parameter $\langle P_{1,c} \rangle$ as a function of volume fraction η for helices with r = 0.2 and p = 4.

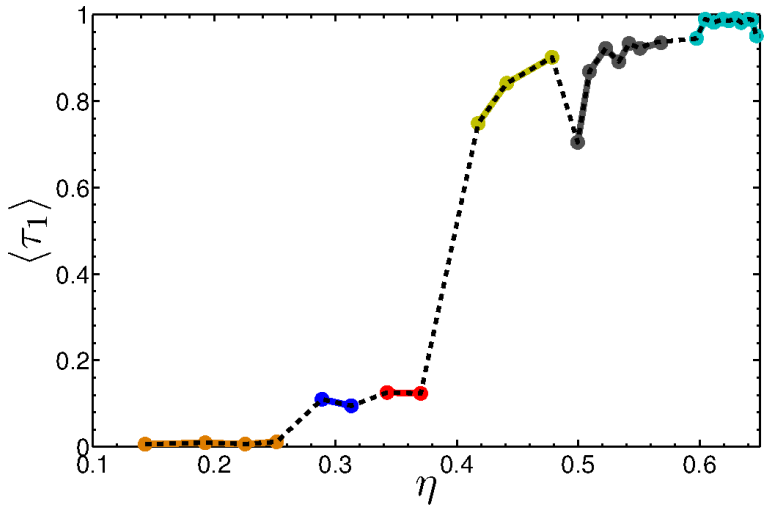

FIGURE 6.29: Smectic order parameter $\langle \tau_1 \rangle$ as a function of volume fraction η for helices with r = 0.2 and p = 4.

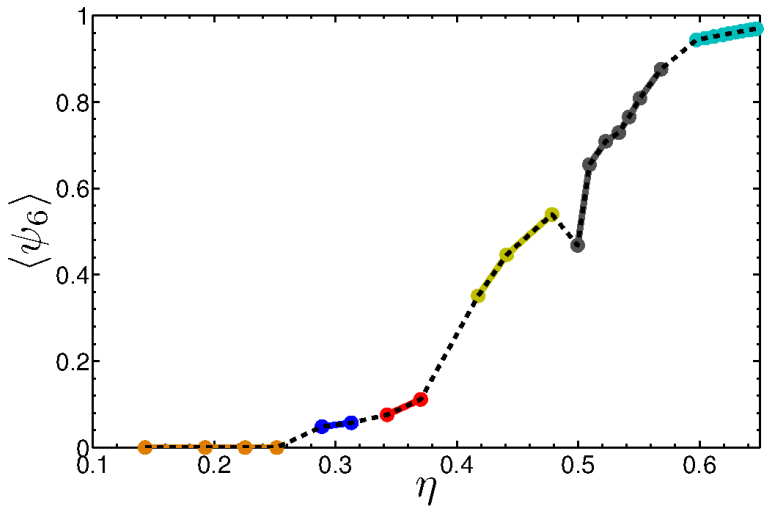

FIGURE 6.30: Hexatic order parameter $\langle\psi_6\rangle$ as a function of volume fraction η for helices with r = 0.2 and p = 4.

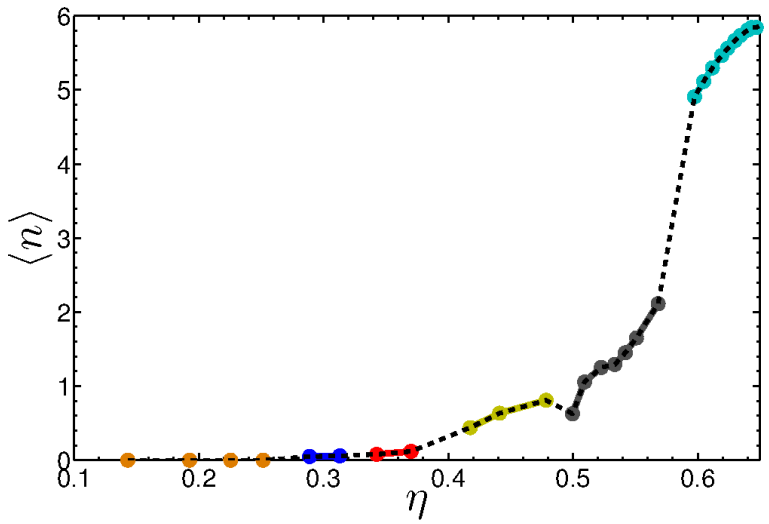

FIGURE 6.31: Average number of nearest neighbours $\langle n \rangle$ as a function of volume fraction η for helices with r = 0.2 and p = 4.

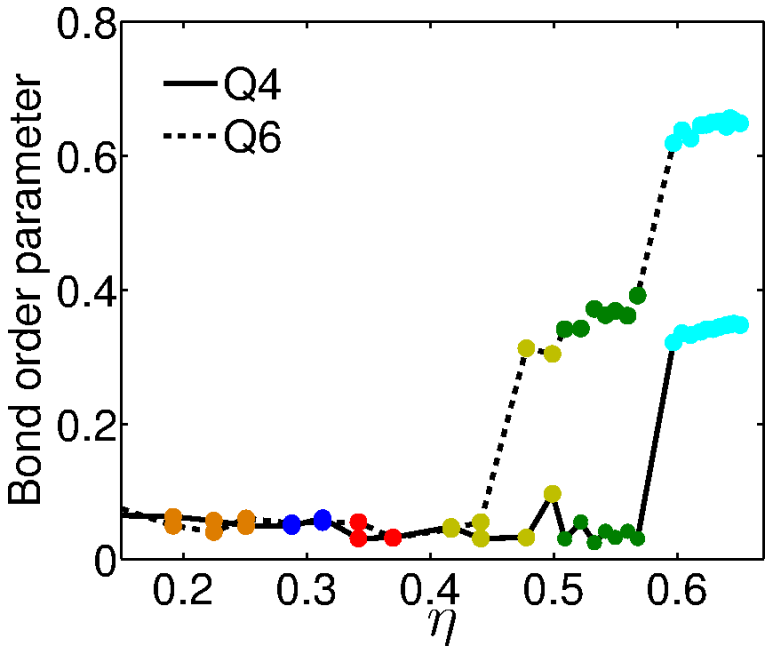

FIGURE 6.32: Average Q4 and Q6 bond order parameters as a function of volume fraction η for helices with r = 0.2 and p = 4.

6.4.3 Equation of state for r = 0.4, p = 4

Helix with r = 0.4 and p = 4 is one of the curliest helix investigated. The phase behaviour has important differences compared to those reported in figures 6.4 and 6.26.From figure 6.34 we can see only two intermediate high density liquid crystal phases N_S^* and $Sm_{B,S}^*$. A direct first order $I - N_S^*$ transition is exhibited without intermediate N phase.Other novel feature is the direct transition from N_S^* to $Sm_{B,S}^*$.

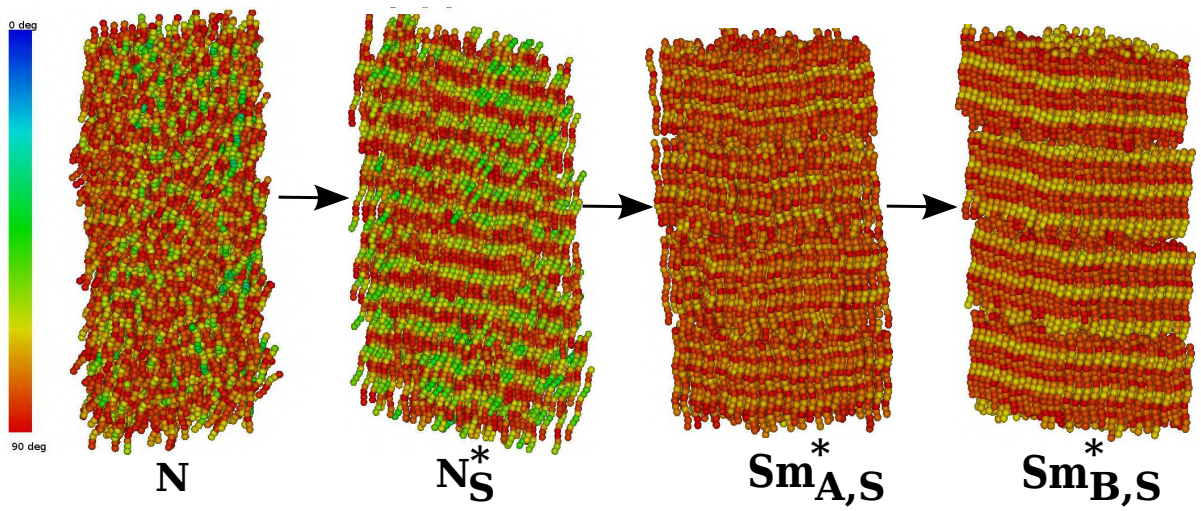

FIGURE 6.33: Figure showing the sequence of phases and their representative snapshots in the case of helices with r = 0.2 and p = 4.

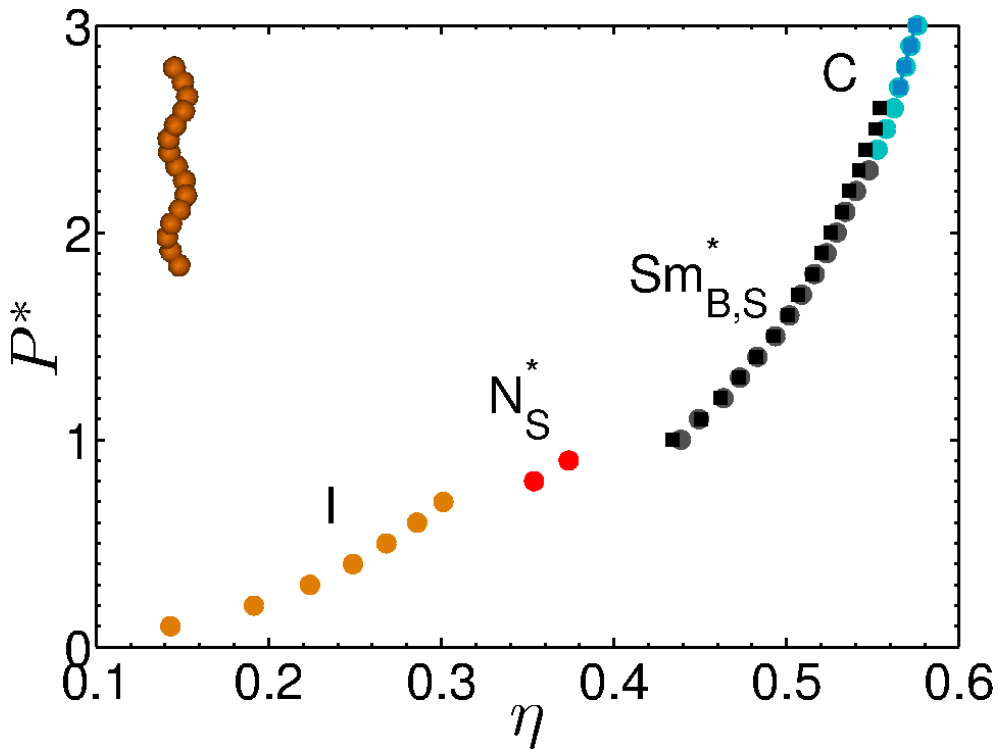

FIGURE 6.34: Equation of state for the system of helices having r = 0.4, p = 4. Different colours indicate different phases. I - isotropic; N_S^* - screw-nematic; $Sm_{B,S}$ - screw-smectic B; C - compact phase

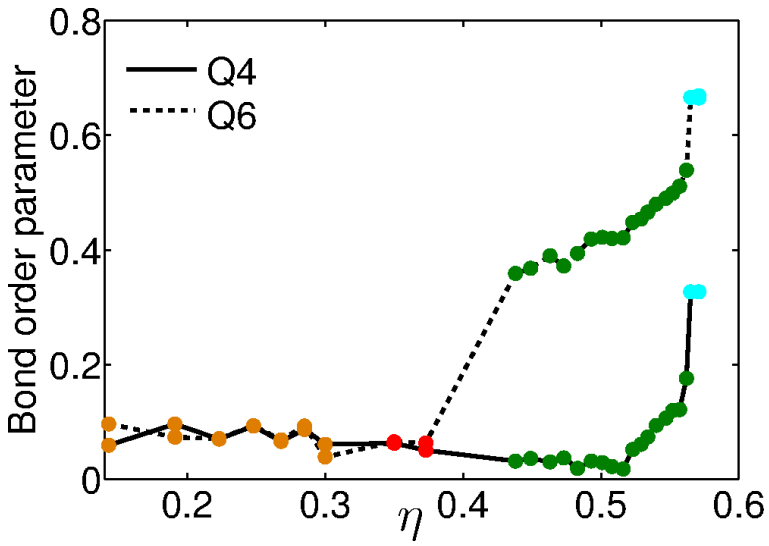

FIGURE 6.35: Average Q4 and Q6 bond order parameters as a function of volume fraction η for helices with r = 0.4 and p = 4.

Figure 6.36 shows $g_{\parallel}(R_{parallel})$ at $\eta = 0.493$ indicating layers with a periodicity close to effective length of the helix ≈ 9.47. Screw like ordering is evidenced by $g^{\hat{\mathbf{w}}}_{1,\parallel}(R_{\parallel})$ and high value of $\langle P_{1,C} \rangle$. Hexagonal order with in the plane is inferred from the double peaked structure of $g_{\perp}(R_{\perp})$ which is shown in figure 6.37. Red dotted line in figure 6.37 corresponds to $g_{\perp}(R_{\perp})$ computed for a single layer. Interesting feature in this case is the absence of first peak at $R_{\perp} \approx 0$ when calculation of $g_{\perp}$ is restricted to single layer and conversely present when carried over all layers. This clearly indicates the AAA type of arrangement, where a helix belonging to a given layer gets stacked on with the one immediately on its top and thus forming a global helix spanning the whole simulation box. It is important to mention at this stage that starting configurations may have a crucial role at high densities. At low densities (Isotropic and Nematic), a different initial condition would result in almost same phase behaviour. However this is not necessarily true at higher densities. It is instructive to dwell on effect of starting configuration on phase diagram at high densities. Figure 6.34 also shows a compression curve plotted with darker points. I remind here that all the results are obtained by starting from a very compact configuration obtained from ISSM method discussed in Chapter3. While the compression is started by taking the smectic configuration which again obtained from compact configuration. All the results in compression are obtained by starting with an equilibrated structure at immediate lower pressure. We can notice a small hysteresis region indicating the uncertainty of finding true coexistence pressure.

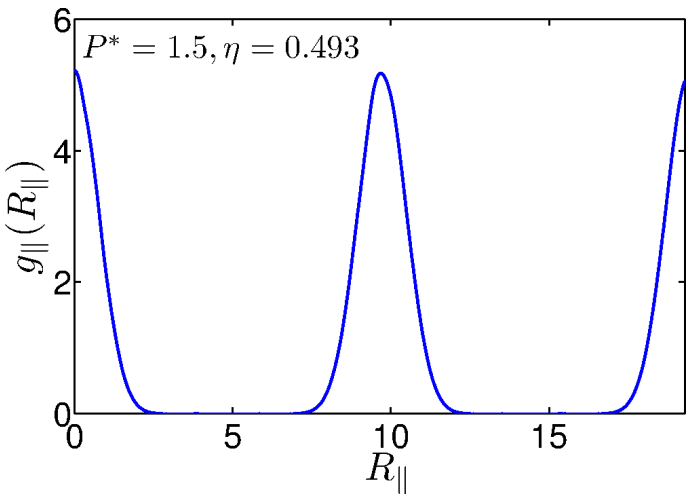

FIGURE 6.36: The parallel correlation function $g\|(R_{\|})$ for helices with r = 0.4 and p = 4, calculated at $\eta = 0.493$, $P^* = 1.5$, in screw smectic B phase.

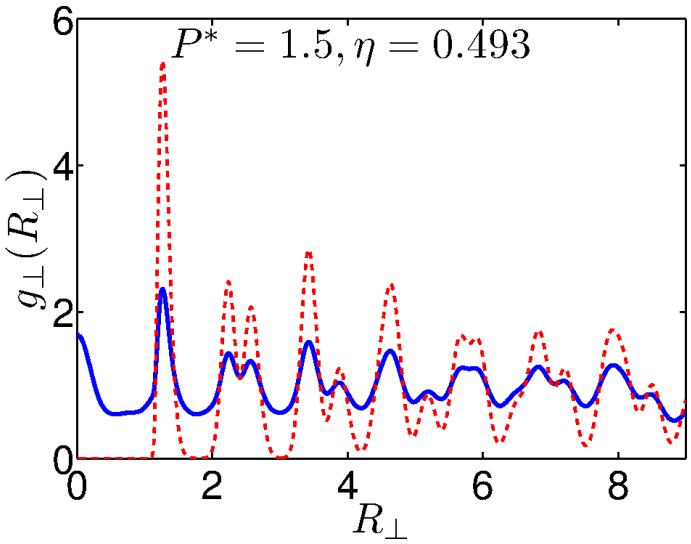

FIGURE 6.37: The parallel correlation function $g\perp(R_{\perp})$ for helices with r = 0.4 and p = 4, calculated at $\eta = 0.493$, $P^* = 1.5$, in screw-smectic B phase.

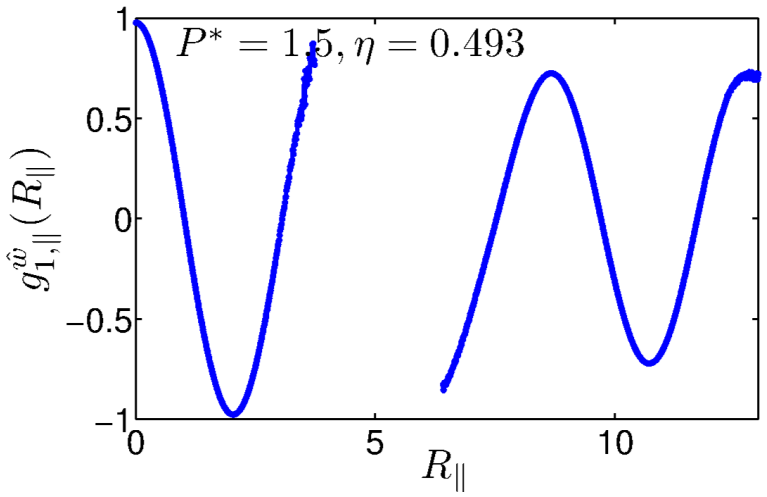

FIGURE 6.38: The screw orientational parallel correlation function $g^{\hat{\mathbf{w}}}_{1,\|}(R_{\|})$ for helices with r = 0.4 and p = 4, calculated at $\eta = 0.493$, $P^* = 1.5$, in screw smectic B phase.

6.4.4 Phase diagrams showing the effect of radius and pitch on smectic phases

6.4.4.1 Phase diagram for r = 0.1

Figure 6.39 shows full phase diagram corresponding to r = 0.1 and pitch varying from 2 to 8. We can see 4 different coloured regions indicating I,N, SmA and Sm B. Going from low to high volume fractions yellow region indicate Isotropic; blue indicate Nematic; Light green indicate smectic A and Dark green indicate smectic B. As mentioned before, the boundaries are not exact and need further studies to find coexistence regions. We did not find SmB - Compact phase C transition with in the region of interest. We observed no specific helical shape effects on the phase diagram for r = 0.1. Nevertheless there is partial screw like order that is emerging for lower pitch values and only at higher densities (in SmB region). This can be seen in the surface plot of $P_{1,C}$ for r = 0.1 in figure 6.40, plotted in η and pitch plane. Notice the value of $P_{1,C}$ corresponding to the colour shown in the colour bar next to the figure. It is clear that the $P_{1,C}$ value is close to zero every where except in the high density region. The maximum value of $P_{1,C}$ found in case of r = 0.1 is 0.5. The irregular patterns in the surface could be due to the possible deviation in the periodicity of the screw-like order because of the formation of layers.

6.4.4.2 Phase diagram for r = 0.2

Figure 6.41 shows full phase diagram in case of r = 0.2 and p = 2 to 8. This figure is an extended phase diagram to that shown in Chapter 3. Going from low to high density we see isotropic, nematic, screw-nematic, screw-smectic A and screw-smectic B, polar-smectic B and finally compact phases. The remarkable difference with the phase diagram of r = 0.1 is the presence of strong screw like order. In Chapter 3, we discussed about the second order $N - N_S^*$ transition. In this figure we can notice that screw like order propagates from Nematic to smectic A region for all pitch values. However propagation of screw like order in Sm_A to Sm_B transition is not uniform for all pitch values. For low pitch values, we see $Sm_{A,S}^*$ to $Sm_{B,S}^*$ transition and then $Sm_{B,S}^*$ to compact phase. Where as for high pitch values like 6,7 and 8 screw like order gradually decreases in smectic B region increasing the polarity in layers. In this region the screw-like correlation between the layers is lost and behave independently. The grey shade in smectic region shows the polar smectic B phase. Figure 6.42 clarifies the overall spread of screw-like order. We can notice significant value of $P_{1,c}$ for low pitch values and gradual decrease in going to higher pitches. The absence of screw-like order at high density for pitches 6, 7 and 8 can be seen clearly in the figure.

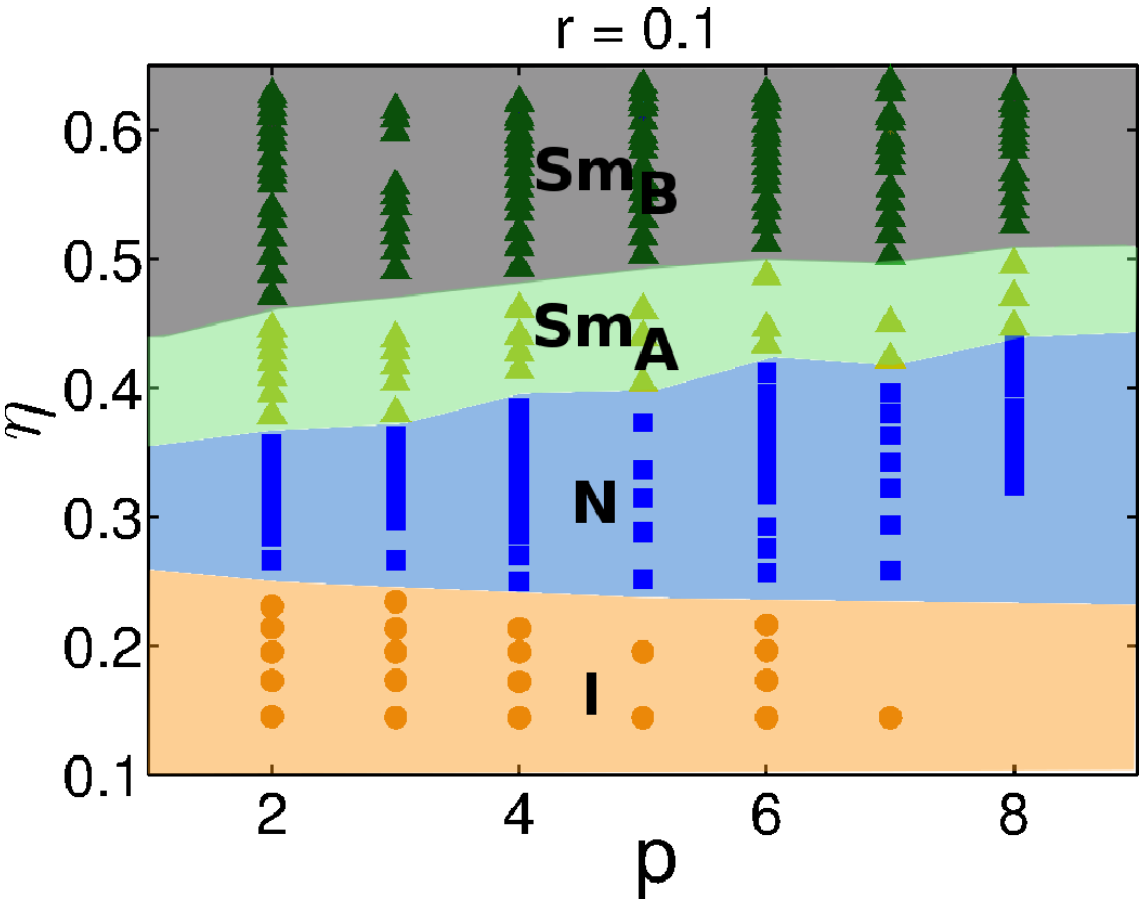

FIGURE 6.39: Full phase diagram of the helices with r = 0.1 shown in the plane of volume fraction η and pitch of the particle. Points plotted as circles indicate Isotropic phase; squares indicate Nematic; triangles indicate smectic phase. Different colours indicate different phases observed. Yellow - Isotropic; Blue - Nematic; Light green - smectic A; Dark green - smectic B

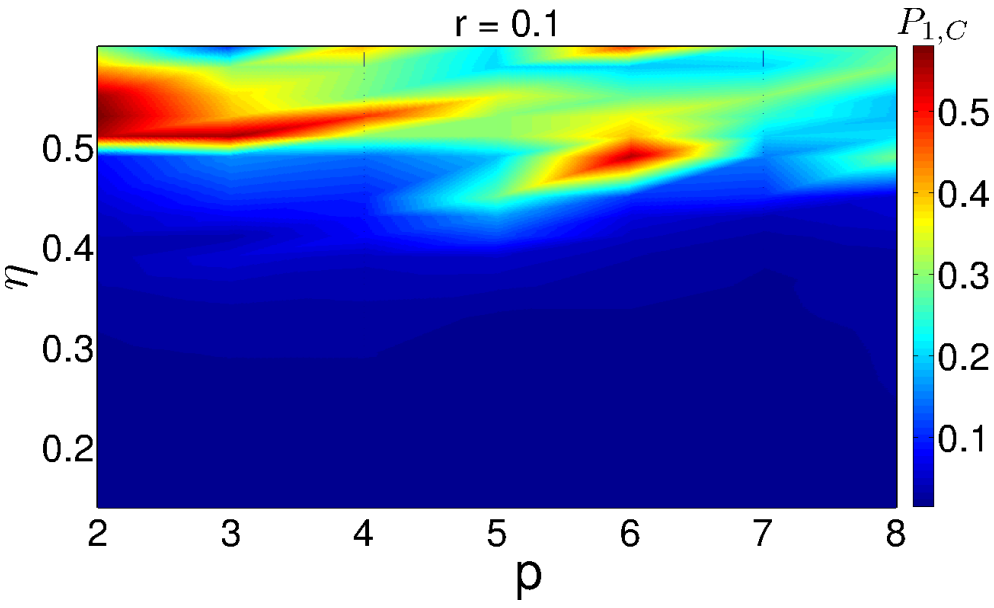

FIGURE 6.40: Surface plot of screw-like order parameter $P_{1,c}$ plotted in the plane of η and pitch of the helix for r = 0.1 .

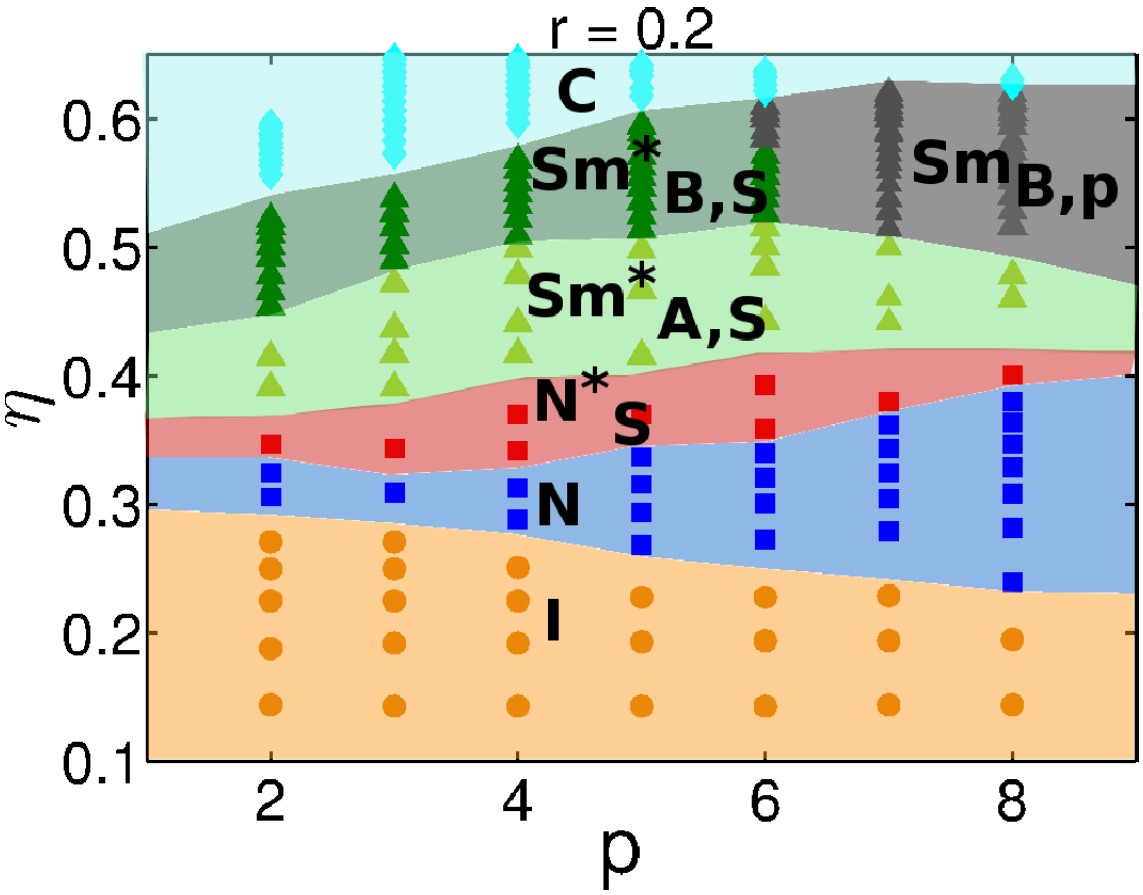

FIGURE 6.41: Full phase diagram of helices with r = 0.2 shown in the plane of volume fraction η and pitch of the particle. Points plotted as circles indicate Isotropic phase; squares indicate Nematic; triangles indicate smectic phase and diamonds indicate crystal like structure. Different colours indicate different phases observed. Each colour is labelled by the phase observed.

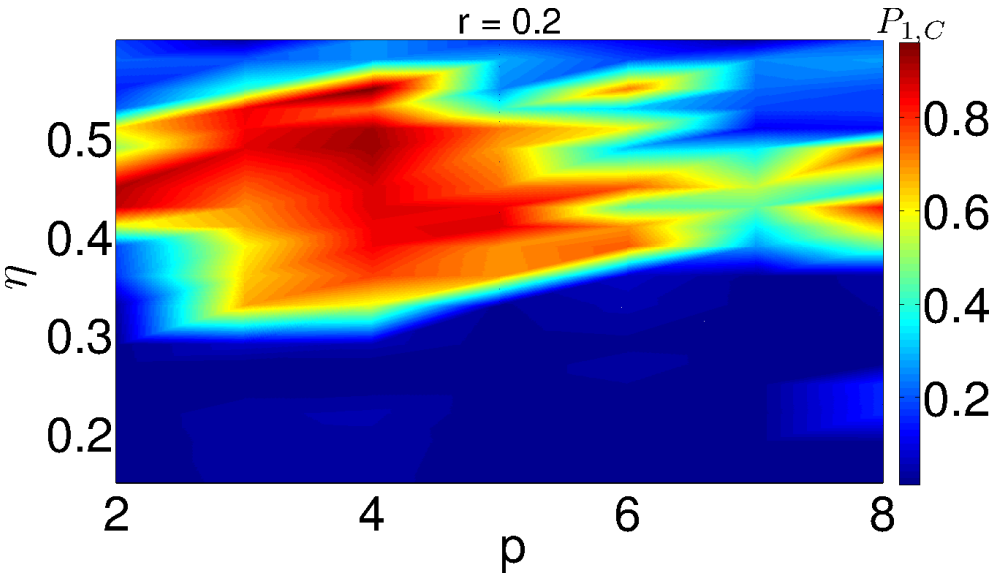

FIGURE 6.42: Surface plot of screw-like order parameter $P_{1,c}$ plotted in the plane of η and pitch of the helix for r = 0.2.

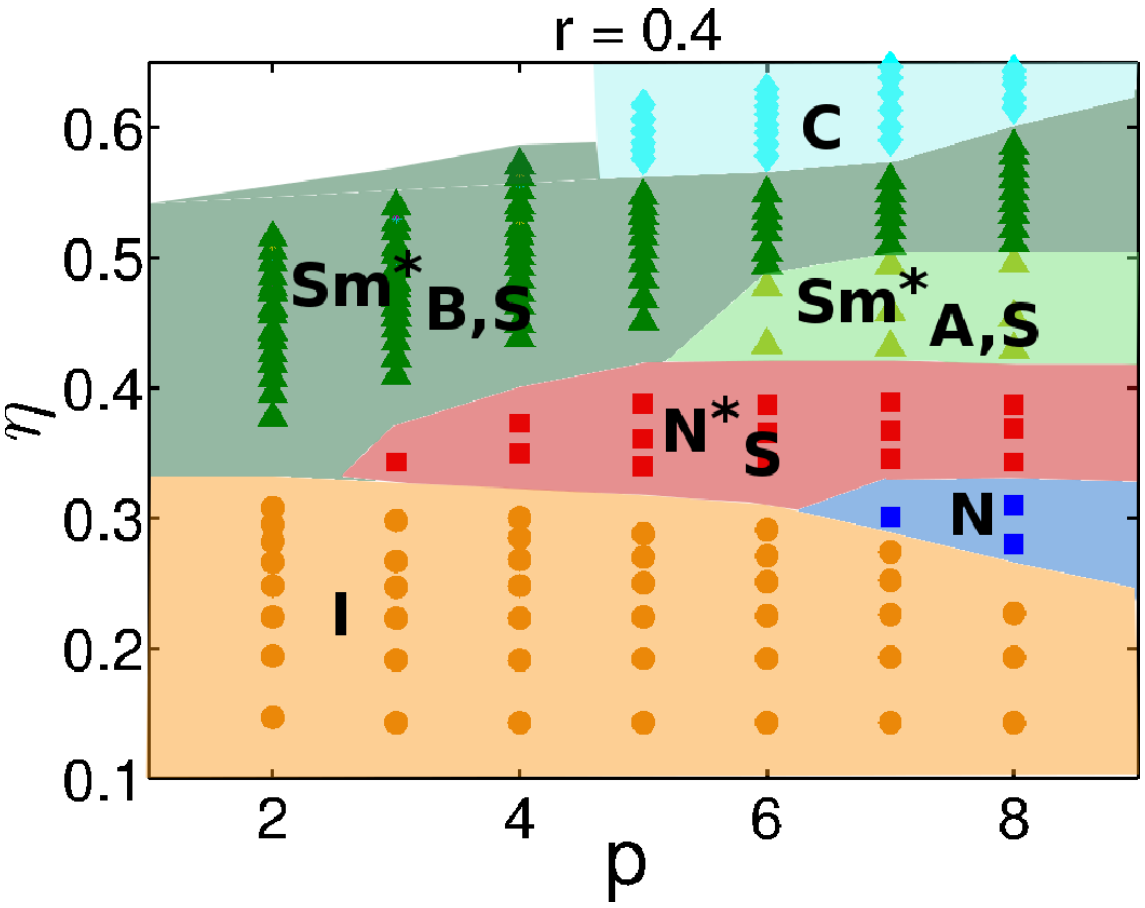

FIGURE 6.43: Full phase diagram of helices with r = 0.4 shown in the plane of volume fraction η and pitch of the particle. Points plotted as circles indicate Isotropic phase; squares indicate Nematic; triangles indicate smectic phase and diamonds indicate crystal like structure. Different colours indicate different phases observed. Each colour is labelled by the phase observed.

6.4.4.3 Phase diagram for r = 0.4

Figure 6.43 show full phase diagram corresponding to r = 0.4. The phase diagram has interesting features in case of r = 0.4 because of the aspect ratio. The aspect ratio of helix goes from 4.01 to 5.85 by increasing pitch form 2 to 8. In this region, the phase behaviour reflects the combined effect of aspect ratio and pitch of the particle. At higher pitches we see a general trend of $I, N_S^*, Sm_{A,S}^*$ and Compact phases. With the decrease in the pitch, there is an increase in the helical twist. This causes a direct $I - N_S^*$ transition with no conventional Nematic. This has been discussed in detail in 3. In smectic region, for pitch p = 5, smectic B appears more stable showing $I - N_S^* - Sm_{B,S}^* - C$ transitions. With further decrease we see a direct $I - Sm_{B,S}^*$ transition. Figure 6.44 shows how the screw like order extends to all pitches.

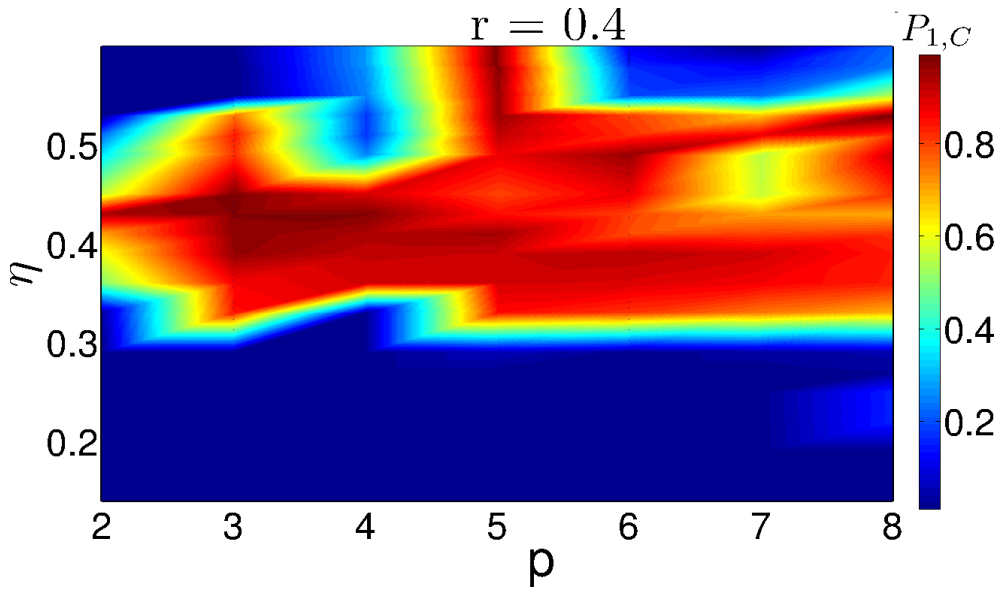

FIGURE 6.44: Surface plot of screw-like order parameter $P_{1,c}$ plotted in the plane of η and pitch of the helix for r = 0.4.

6.4.5 Evidence of Columnar phase after smectics?

As mentioned before simulations at high densities have a strong dependence on the initial configuration. The initial condition plays a major role in deciding the phase. For certain shapes, the expansion starting from a dilute smectic configuration resulted in a columnar phase. However the smectic configuration is obtained by starting from a compact configuration obtained from ISSS method. The phase behaviour is different along the compression curve. Let us consider one such shape with $r = 0.3$ and $p = 3$. Simulations starting from a dilute $Sm^*_{A,S}$ develop hexagonal order with increasing *eta*. The interesting behaviour at this point is the drop in smectic order parameter while screw-like order and hexagonal order still persists. This phase can be described as hexagonal columnar. With the increase in volume fraction, smectic order parameter rises slowly resulting in a smectic C with screw like order and hexagonal order. Though the layers formed in $Sm^*_{C,S}$ are not perfect. This could be due to the weak stability of this phase.

Figure 6.45 shows the drop in smectic order parameter after $\eta = 0.42$. At $\eta = 0.5$, we see a steady increase in order parameter. Figure 6.46 shows how the parallel correlation is lost with increase in volume fraction. Correlation function $g_\perp$ in figure 6.47 indicate the hexatic order in the system. Correlation function $g^{\hat{\mathbf{w}}}_{1,\|}$ shown in the figure 6.48 indicate the screw like order in the system. Figure 6.51 shows the snapshot with regular stripes indicating the screw like order in the system. Figure 6.50 shows the snapshot coloured according to their position to show the de-localisation of layers.

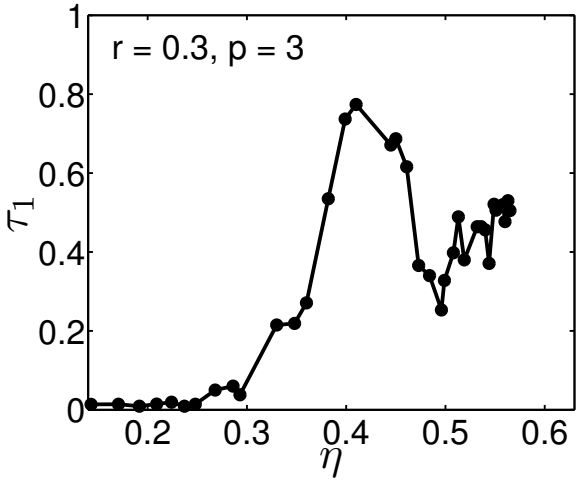

FIGURE 6.45: smectic order parameter $\langle P_{1,c} \rangle$ as a function of volume fraction η for helices with r = 0.3 and p = 3.

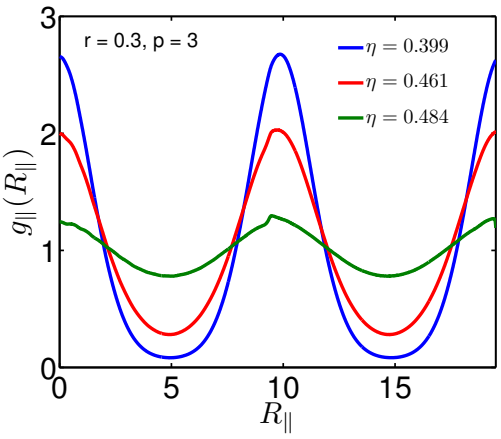

FIGURE 6.46: The parallel correlation functions $g\perp(R_\perp)$ for helices with r = 0.3 and p = 3, calculated at $\eta = 0.399; 0.461; 0.484$.

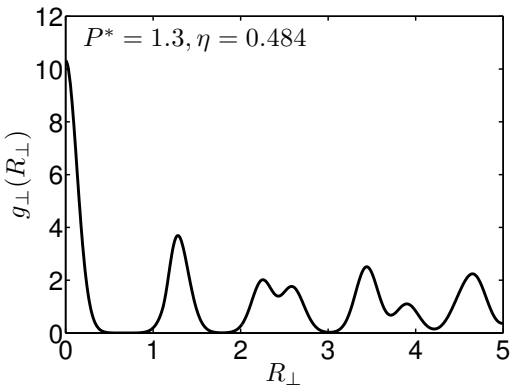

FIGURE 6.47: The perpendicular correlation function $g\perp(R_\perp)$ for helices with r = 0.3 and p = 3, calculated at $\eta = 0.484$.

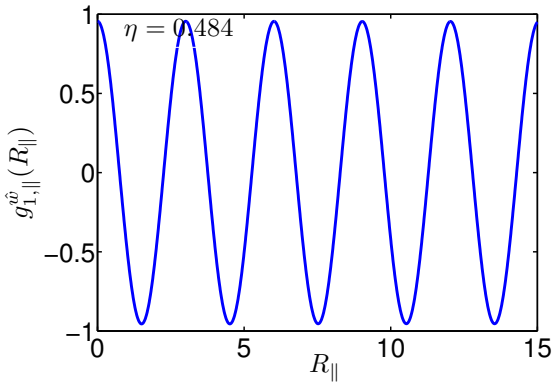

FIGURE 6.48: The screw orientational parallel correlation function $g^{\hat{\mathbf{w}}}_{1,\parallel}(R_\parallel)$ for helices with r = 0.3 and p = 3, calculated at $\eta = 0.484$, $P^* = 1.3$, in screw smectic B phase.

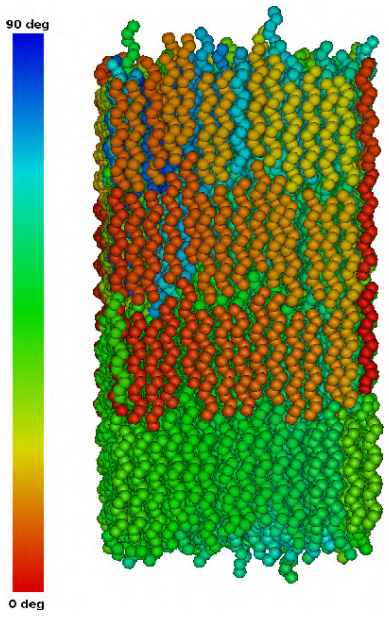

FIGURE 6.49: Snapshot of the system of helices having r = 0.3, p = 3 at $\eta = 0.399$ in $Sm^*_{B,S}$ phase. The colouring is done according to the position of the helices.

Presented are the preliminary results. This result is in support of the experimental result on semi flexible virus by Grelet *etal*. This work shows an evidence of columnar phase after smectic B in case of semi-flexible virus [88]. In this case, $Sm_B - col$ transition is found to be independent of rod flexibility.

6.5 Conclusions

In this work we have studied the self assembly properties of systems of hard helices as a function of helix shape. We found a rich and unconventional polymorphism which is striking contrast to hard spherocylinder phase behaviour. Helices which are rod-like show phase behaviour similar to hard rods with an additional hexagonal order in smectic

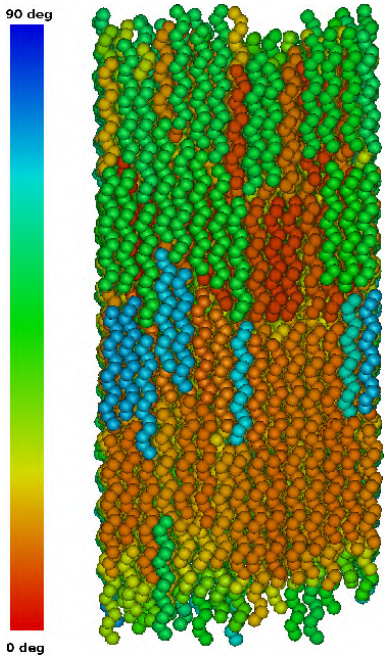

FIGURE 6.50: Snapshot of the system of helices having r = 0.3, p = 3 at $\eta = 0.484$ in columnar phase phase. The colouring is done according to the position of the helices.

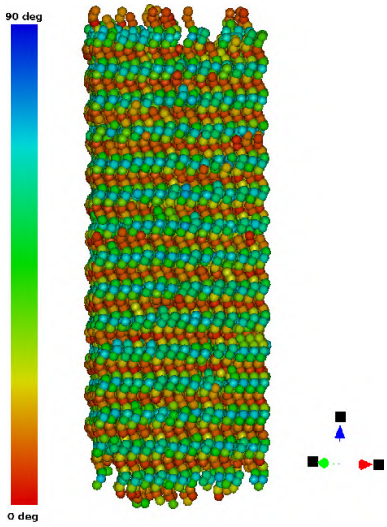

FIGURE 6.51: Snapshot of the system of helices having r = 0.3, p = 3 at $\eta = 0.484$ in columnar phase. The colouring is done according to the local tangent of the helices.

phase. With the increase in the radius of helix, we see a rich phase diagram with different phases. With increase in the density, a smectic A phase with screw like order can appear. Helices lying in the interlayer regions provide a bridge between adjacent layers which allows to keep the the screw like organization. As the density increases, we see two types of smectic phases depending on the shape of the helix. For less curly helices, screw-like order vanishes bringing a polar order in the smectic phase. On other hand, the highly twisted helices undergo a transition to smectic B with screw-like order.

Chapter 7

Summary

Helix shape plays a prominent role in biological activities. Many particles like DNA, RNA and virus particles acquire helical shape. Though the helical shape is ubiquitous in nature, little is known about the role of helical shape in liquid crystal organization. Our work on hard helical particles answers few questions like the effect of helical shape on the liquid crystal phase diagram. Our work clearly explains the physical mechanism behind the liquid crystalline phase of helical flagella [5]. We have studied the phase behaviour of different helical shapes varying radius and pitch of the helix. We found a rich polymorphism showing new chiral phases in nematic and smectic region. Here I give a brief report on each chapter and the results obtained.

In Chapter 3, I present the results on isotropic-nematic transition of hard helical particles. We found that the location of the isotropic-nematic transition depends on the shape of the helix. Unlike spherocylinder, same aspect ratio can be achieved with different helical parameters. So the approximation of helix to a spherocylinder gives deviation in the results. We found that the results from Onsager theory deviates from Monte Carlo results and this deviation increases with increase in the helicity. Compared to Monte Carlo results, results from Onsager theory underestimates the pressure value.

In Chapter 4, I present the details and implementation of Isopointal set structural Search method (ISSM). In this work, we obtained the maximum packing densities of different shapes of helices. Except few helices with pitch equal to 1, all helical shapes prefer hexagonal arrangement with one particle per unit cell. The method is based on the simulation annealing techniques and gives best compact strucutre in a plane. Neither curly nor slender helices are giving best packing. The intermediate helices are giving highest packing fraction. However, the planar density is found to be the same for all helices after the crossover. Packing fraction variations after the crossover are occuring

due to difference in the height of the particles. The configuration thus obtained are used to construct intial configuration to for the expansion using NPT Monte Carlo simulation.

Chapter 5 consists of important results on the new phase that is observed in nematic region. The origin of this new chiral nematic phase is due to the coupled translational and rotational motion of helices. Unlike the long axis in cholesteric phase, the C_2 symmetry axis of the helix which is perpendicular to the long-axis spirals around the nematic director. This is purely entropy driven and always occurs at the high density end of the nematic phase. We have characterized this new phase using lowest rank order parameter $P_{1,C}$ and correlation function $g^{\hat{\mathbf{w}}}_{1,||}$. We found either first order isotropic to screw nematic or second order nematic to screw-nematic transition depending on the geometry of the helix.

In Chapter 6, I present high density liquid crystal phases of helical particles. We found rich and unconventional polymorphism in the smectic region of th ephase diagram. We found three different smectic phases depending on the density and the geometry of the helical particle. We found smectic A with screw like order, smectic B with screw like order and smectic B with polar order. Part of the helices lying in the layer gap provide the information of the C_2 axis orientation from the layer below to the next layer. I present the phase diagrams in density - pitch plane for different values of radius ranging from r = 0.1 to 0.4. On an other hand, we found a stable columnar phase starting from a dilute smectic phase for few geometries of helix. Further investigation in characterizing these phases.

Appendix A

Relation between the length and number of turns of the helix

Consider a helix as parametrized by an angular coordinate $0 \leq \zeta \leq 2\pi n_p$ where n_p is the number of different turns (i.e. pitches). In Cartesian coordinates, its representation with respect to an origin of the helix is identified as the vector

$$r(\zeta) = r\cos(\zeta)\hat{\mathbf{e}_x} + r\sin(\zeta)\hat{\mathbf{e}_y} + p\frac{\zeta}{2\pi}\hat{\mathbf{e}_z} \tag{A.1}$$

Here r and p are the radius and the pitch of the helix, respectively. Then we have

$$\frac{\partial}{\partial\zeta}r(\zeta) = -rsin(\zeta)\hat{\mathbf{e}_x} + r\cos(\zeta)\hat{\mathbf{e}_y} + \frac{p}{2\pi}\hat{\mathbf{e}_z} \tag{A.2}$$

On recalling that the tangent unit vector has the form

$$\hat{\mathbf{T}}(s) = \frac{\partial}{\partial s}r(s) \tag{A.3}$$

where

$$\frac{\partial}{\partial s}r(s) = \frac{1}{s\prime(s)}\frac{\partial}{\partial\zeta}R(\zeta) \tag{A.4}$$

we then have that the condition

$$\hat{\mathbf{T}}(s).\hat{\mathbf{T}}(s) = \frac{\partial}{\partial s}r(s).\frac{\partial}{\partial s}r(s) = 1 \tag{A.5}$$

leads to

$$(s\prime)^2 = r^2 + \frac{p^2}{4\pi^2} \tag{A.6}$$

This can be integrated to get the total length of the string (the backbone of the helix)

$$L = \int_0^{2\pi n_p} d\zeta \sqrt{r^2 + \frac{p^2}{4\pi^2}} = n_p \sqrt{p^2 + (2\pi r)^2} \tag{A.7}$$

Note that this is, in general, different from the "euclidean length" $\Lambda = n_p P$ that corresponds to the length of the associated spherocylinder. If we slice the angular variable ζ in $n_{sp} - 1$ pieces, n_{sp} being the number of spheres of diameter D forming the helix, we then have $L = (n_{sp} - 1)\Delta\zeta D$, with the angular amplitude of each slice is given by

$$\Delta\zeta = \frac{n_p}{D(n_{sp} - 1)} \sqrt{p^2 + (2\pi r)^2} \tag{A.8}$$

Hence if one assumes D as the unit of lengths, the geometry of the helix requires inputs : r, p, n_{sp} and n_p (or alternatively , Λ).

Appendix B

Checking for the overlap between two rigid helices

Condider two helical particles denoted by 1, 2 with their center of masses lying at (X_1,Y_1,Z_1) and (X_2,Y_2,Z_2) and direction vectors of their long axes being $\mathbf{U_1}$ and $\mathbf{U_2}$. The alogrithm of the overlap check is as follows:

• The distance between the centres $\mathbf{r_{12}}$ is given by

$$\mathbf{r_{12}} = \sqrt{(X_2 - X_1)^2 + (Y_2 - Y_1)^2 + (Z_2 - Z_1)^2} \tag{B.1}$$

If $\mathbf{r_{12}}$ is greater than the length of the helix $L+D$, then there is no overlap in the helices. Else the shortest distance between the long axes of the helices has to be found to check the overlap.

• Shortest distance between the long axes of the helix:

let x be the shortest distance between the axes and can be written as

$$x = r_{12} + \mu U_2 - \lambda U_1 \tag{B.2}$$

The values of λ and μ giving the shortest distance lie in any of the four quardrants in (λ, μ) plane and lie within the interval $[-L/2, L/2]$. The values are obtained by minimising the function x^2 [58] .

• If distanc x is greater than the width of the helix (2r+D), then there is no overlap in the helices. Else the overlap has to be checked bead by bead.

Appendix C

Definition of the Frenet frame

The helix axis can be described by a curve $\mathbf{R}(s)$ parameterized by its arc length s. In dealing with such curved objects it proves convenient to introduce suitable curvilinear coordinates to perform the calculations in a more efficient way and this is achieved by introducing a particular Frenet frame of unit vectors $\{\hat{\mathbf{T}}(s), \hat{\mathbf{N}}(s), \hat{\mathbf{B}}(s)\}$ for the tangent, normal and binormal respectively, as follows

$$\begin{aligned} \hat{\mathbf{T}}(s) &= \frac{\mathbf{R}'(s)}{\|\mathbf{R}'(s)\|} \\ \hat{\mathbf{N}}(s) &= \frac{\hat{\mathbf{T}}'(s)}{\|\hat{\mathbf{T}}'(s)\|} \\ \hat{\mathbf{B}}(s) &= \hat{\mathbf{T}}(s) \times \hat{\mathbf{N}}(s) \end{aligned} \tag{C.1}$$

where the prime denotes the derivative with respect to the argument. The Frenet coordinates satisfies the Frenet-Serret equations

$$\begin{aligned} \frac{\partial \hat{\mathbf{T}}(s)}{\partial s} &= \kappa(s)\,\hat{\mathbf{N}}(s) \\ \frac{\partial \hat{\mathbf{N}}(s)}{\partial s} &= -\kappa(s)\,\hat{\mathbf{T}}(s) + \tau(s)\,\hat{\mathbf{B}}(s) \\ \frac{\partial \hat{\mathbf{B}}(s)}{\partial s} &= -\tau(s)\,\hat{\mathbf{N}}(s) \end{aligned} \tag{C.2}$$

which automatically define the curvature $\kappa(s)$ and the torsion $\tau(s)$ from the first and the last equations of (C.3). Note that it is convention to choose $\kappa(s)$ to be positive by absorbing the sign in the direction of the normal vector $\hat{\mathbf{N}}(s)$.

Appendix D

Correlation functions of various nature

Consider a system of N helices in a volume $V = L^3$ so that $\rho = N/V$ is the their density. Let $\widehat{\mathbf{u}}_i(\omega_i)$ and $\widehat{\mathbf{u}}_j(\omega_j)$ be the unit vectors associated with the orientations of helices i and j, and let $\widehat{\mathbf{r}}_{ij}(\omega)$ the unit vector associated with the center-to-center separation $\mathbf{r}_{ij} = \mathbf{r}_i - \mathbf{r}_j$. They are individuated by solid angles ω_i,ω_j, and ω respectively. We expect the pair-potential to be of the form

$$\phi\left(ij\right) = \phi\left(\mathbf{r}_{ij}, \widehat{\mathbf{u}}_i, \widehat{\mathbf{u}}_j\right) \tag{D.1}$$

We further introduce the nematic vector $\widehat{\mathbf{n}}$. This then suggests the decoupling

$$\mathbf{r}_{ij} = \mathbf{r}_{ij}^{\parallel} + \mathbf{r}_{ij}^{\perp} = \left(\mathbf{r}_{ij} \cdot \widehat{\mathbf{n}}\right)\widehat{\mathbf{n}} + \left|\mathbf{r}_{ij} \times \widehat{\mathbf{n}}\right|\widehat{\mathbf{r}}_{ij}^{\perp} \tag{D.2}$$

D.1 Parallel and perpendicular correlation functions

In analogy with the procedure for the computation of the radial distribution function $g(r)$ [47], we proceed as follows.

$$\left\langle \sum_{i<j} \delta\left(r_{\parallel} - \left(\mathbf{r}_{ij} \cdot \widehat{\mathbf{n}}\right)\right) \right\rangle = \frac{1}{Z_N} \int \left[\prod_{l=1}^{N} d^3\mathbf{r}_l \frac{d\omega_l}{4\pi}\right] \sum_{i<j} \delta\left(r_{\parallel} - \left(\mathbf{r}_{ij} \cdot \widehat{\mathbf{n}}\right)\right) e^{-\beta \sum_{l<m} \phi(lm)} \tag{D.3}$$

where Z_N is the usual configurational partition function. Because of the symmetry among the helices, and using the definition

$$\rho\left(12\right)=\rho^2 g\left(12\right) \quad = \quad \frac{N\left(N-1\right)}{Z_N}\int\left[\prod_{l\geq 3} d^3\mathbf{r}_l \frac{d\omega_l}{4\pi}\right] e^{-\beta\sum_{l<m}\phi(lm)} \tag{D.4}$$

equation (D.3) can then be reduced to

$$\left\langle \sum_{i<j}\delta\left(r_{\parallel}-\left(\mathbf{r}_{ij}\cdot\widehat{\mathbf{n}}\right)\right)\right\rangle \quad = \quad \int d^3\mathbf{r}_1\, d^3\mathbf{r}_2 \int \frac{d\omega_1}{4\pi}\,\frac{d\omega_2}{4\pi}\,\delta\left(r_{\parallel}-\left(\mathbf{r}_{ij}\cdot\widehat{\mathbf{n}}\right)\right)\rho^2 g\left(12\right) \tag{D.5}$$

The factor $N(N-1)$ appearing in eq(D.4) clearly accounts for all ordered pairs of helices. We further note that

$$\int d^3\mathbf{r}_1\, d^3\mathbf{r}_2 \quad = \quad V\int d^3\mathbf{r}_{12} = V\int_0^L dr_{12}^{\parallel}\int d^2\mathbf{r}_{12}^{\perp} \tag{D.6}$$

and introduce the short-hand notation

$$\left\langle \ldots\right\rangle_{\omega} \quad = \quad \frac{1}{4\pi}\int d\omega\ldots \tag{D.7}$$

Then, eq.(D.5) becomes

$$\left\langle \sum_{i<j}\delta\left(r_{\parallel}-\left(\mathbf{r}_{ij}\cdot\widehat{\mathbf{n}}\right)\right)\right\rangle \quad = \quad V\rho^2\int_0^L dr_{12}^{\parallel}\delta\left(r_{\parallel}-r_{12}^{\parallel}\right)\int d^2\mathbf{r}_{12}^{\perp}\left\langle g\left(r_{12}^{\parallel},\mathbf{r}_{12}^{\perp},\omega_1,\omega_2\right)\right\rangle_{\omega_1,\omega_2} \tag{D.8}$$

One can then identify the parallel correlation function as an average over the perpendicular component (of area πL^2)

$$g_{\parallel}\left(r_{\parallel}\right) \quad = \quad \frac{1}{\pi L^2}\int d^2\mathbf{r}_{12}^{\perp}\left\langle g\left(r_{12}^{\parallel},\mathbf{r}_{12}^{\perp},\omega_1,\omega_2\right)\right\rangle_{\omega_1,\omega_2} \tag{D.9}$$

so that, we get from eqs.(D.8) and (D.9)

$$g_{\parallel}\left(r_{\parallel}\right) \quad = \quad \frac{1}{\pi N\rho L^2}\left\langle \sum_{i<j}\delta\left(r_{\parallel}-\left(\mathbf{r}_{ij}\cdot\widehat{\mathbf{n}}\right)\right)\right\rangle \tag{D.10}$$

This expression should correspond to eq.(9) in Ref.[87].

With a similar procedure, we consider the perpendicular component. Here we find

$$\left\langle \sum_{i<j}\delta\left(r_{\perp}-\left|\mathbf{r}_{ij}\times\widehat{\mathbf{n}}\right|\right)\right\rangle \quad = \quad V\int d^3\mathbf{r}_{12}\delta\left(r_{\perp}-\left|\mathbf{r}_{12}\times\widehat{\mathbf{n}}\right|\right)\rho^2\left\langle g\left(r_{12}^{\parallel},\mathbf{r}_{12}^{\perp},\omega_1,\omega_2\right)\right\rangle_{\omega_1,\omega_2} \tag{D.11}$$

With the definition of perpendicular correlation function

$$g_{\perp}\left(r_{\perp}\right) = \frac{1}{L}\int dr_{12}^{\parallel}\left\langle g\left(r_{12}^{\parallel},\mathbf{r}_{12}^{\perp},\omega_1,\omega_2\right)\right\rangle_{\omega_1,\omega_2} \tag{D.12}$$

one then gets from eq.(D.11)

$$g_{\perp}\left(r_{\perp}\right) = \frac{1}{2\pi N\rho r_{\perp}L}\left\langle\sum_{i<j}\delta\left(r_{\perp}-\left|\mathbf{r}_{ij}\times\widehat{\mathbf{n}}\right|\right)\right\rangle \tag{D.13}$$

that is the analog of eq.(10) in Ref.[87].

D.2 Coefficients of rotational invariants

The general expansion of $g(12)$ in rotational invariants for a linear molecule in an arbitrary frame is given by [89]

$$g\left(12\right)=g\left(\mathbf{r}_{12},\omega_1,\omega_2\right) = \sum_{l_1l_2l}g^{l_1l_2l}\left(r_{12}\right)\Phi^{l_1l_2l}\left(\omega_1,\omega_2,\omega\right) \tag{D.14}$$

where $g^{l_1l_2l}(r_{12})$ are the seeked coefficients, and the rotational invariants have the form

$$\Phi^{l_1l_2l}\left(\omega_1,\omega_2,\omega\right)\sum_{m_1m_2m}C\left(l_1l_2l;m_1m_2m\right)Y_{l_1m_1}\left(\omega_1\right)Y_{l_2m_2}\left(\omega_2\right)Y_{lm}^{*}\left(\omega\right) \tag{D.15}$$

Here $C(l_1l_2l;m_1m_2m)$ are the Clebsh-Gordan coefficients and $Y_{lm}\left(\omega\right)$ the usual spherical harmonics of order lm. We further note that

$$g^{l_1l_2l}\left(r_{12}\right) = h^{l_1l_2l}\left(r_{12}\right)+\delta_{l_10}\delta_{l_20}\delta_{l0} \tag{D.16}$$

Using the expansion (D.14) and the normalization condition

$$\left\langle\Phi^{l_1l_2l}\left(\omega_1,\omega_2,\omega\right)\Phi^{l_1'l_2'l}\left(\omega_1,\omega_2,\omega\right)\right\rangle_{\omega_1,\omega_2} = \delta_{l_1l_1'}\delta_{l_2l_2'}\delta_{ll'}\left\langle\left[\Phi^{l_1l_2l}\left(\omega_1,\omega_2,\omega\right)\right]^2\right\rangle_{\omega_1,\omega_2} \tag{D.17}$$

so that, one obtains from (D.14) and (D.17)

$$g^{l_1l_2l}\left(r_{12}\right) = \frac{\left\langle g\left(\mathbf{r}_{12},\omega_1,\omega_2\right)\Phi^{l_1l_2l}\left(\omega_1,\omega_2,\omega\right)\right\rangle}{\left\langle\left[\Phi^{l_1l_2l}\left(\omega_1,\omega_2,\omega\right)\right]^2\right\rangle_{\omega_1,\omega_2}} \tag{D.18}$$

Consider now the simplest non-trivial rotational invariant

$$\Phi^{110}\left(\omega_1,\omega_2,\omega\right) = \widehat{\mathbf{u}}_1(\omega_1)\cdot\widehat{\mathbf{u}}_2(\omega_2) \tag{D.19}$$

Then we have

$$\begin{aligned}
\left\langle \sum_{i<j} \delta\left(r-r_{ij}\right) \Phi^{110}\left(\omega_1, \omega_2, \omega\right)\right\rangle &= \frac{1}{Z_N} \int\left[\prod_{l=1}^{N} d^3 \mathbf{r}_l \frac{d \omega_l}{4 \pi}\right] \sum_{i<j} \delta\left(r-r_{ij}\right) \Phi^{110}\left(\omega_i, \omega_j, \omega\right) e^{-\beta \sum_{l<m} \phi(lm)} \\
&= \frac{N(N-1)}{Z_N} \int\left[\prod_{l=1}^{N} d^3 \mathbf{r}_l \frac{d \omega_l}{4 \pi}\right] \delta\left(r-r_{12}\right) \Phi^{110}\left(\omega_1, \omega_2, \omega\right) e^{-\beta \sum_{l<m} \phi} \\
&= \int d^3 \mathbf{r}_1 d^3 \mathbf{r}_2 \int \frac{d \omega_1}{4 \pi} \frac{d \omega_2}{4 \pi} \delta\left(r-r_{12}\right) \Phi^{110}\left(\omega_1, \omega_2, \omega\right) \rho(12) \\
&= \rho N 4 \pi \int_0^{+\infty} d r_{12} r_{12}^2 \delta\left(r-r_{12}\right)\left\langle \Phi^{110}\left(\omega_1, \omega_2, \omega\right) g\left(r_{12}, \omega_1, \omega_2, \omega\right)\right\rangle
\end{aligned}$$

Use of eqs.(D.17) and (D.18), along with the result [90]

$$\left\langle\left[\Phi^{110}\left(\omega_1, \omega_2, \omega\right)\right]^2\right\rangle_{\omega_1, \omega_2} = \frac{1}{3} \tag{D.21}$$

along with eq.(D.16), leads to

$$g^{110}(r)=h^{110}(r) = \frac{3}{4 \pi N \rho r^2}\left\langle \sum_{i<j} \delta\left(r-r_{ij}\right) \Phi^{110}\left(\omega_1, \omega_2, \omega\right)\right\rangle \tag{D.22}$$

that coincides with eq.(9b) of Ref.[91].

The same procedure applies for all other rotational invariants. For instance

$$\Phi^{112}\left(\omega_1, \omega_2, \omega\right) = 3\left(\widehat{\mathbf{u}}_1(\omega_1) \cdot \widehat{\mathbf{r}}_{12}(\omega)\right)\left(\widehat{\mathbf{u}}_2(\omega_2) \cdot \widehat{\mathbf{r}}_{12}(\omega)\right)-\widehat{\mathbf{u}}_1(\omega_1) \cdot \widehat{\mathbf{u}}_2(\omega_2) \tag{D.23}$$

The analog of (D.21) is now

$$\left\langle\left[\Phi^{112}\left(\omega_1, \omega_2, \omega\right)\right]^2\right\rangle_{\omega_1, \omega_2} = \frac{2}{3} \tag{D.24}$$

so that

$$g^{112}(r)=h^{112}(r) = \frac{3}{8 \pi N \rho r^2}\left\langle \sum_{i<j} \delta\left(r-r_{ij}\right) \Phi^{112}\left(\omega_1, \omega_2, \omega\right)\right\rangle \tag{D.25}$$

that is eq.(9c) of Ref. [91]. Finally, for [90]

$$\Phi^{220}\left(\omega_1, \omega_2, \omega\right) = 1-3 T_1^2 T_2^2-3 T_3^2-6 T_1 T_2 T_3 \tag{D.26}$$

where we have introduced the following short-hand notations [90]

$$T_1 = \widehat{\mathbf{u}}_1(\omega_1) \cdot \widehat{\mathbf{r}}_{12}(\omega) \tag{D.27}$$

$$T_2 = \widehat{\mathbf{u}}_2(\omega_2) \cdot \widehat{\mathbf{r}}_{12}(\omega) \tag{D.28}$$

$$T_3 = \widehat{\mathbf{u}}_1(\omega_1) \cdot \widehat{\mathbf{u}}_2(\omega) - \left(\widehat{\mathbf{u}}_1(\omega_1) \cdot \widehat{\mathbf{r}}_{12}(\omega)\right)\left(\widehat{\mathbf{u}}_2(\omega_2) \cdot \widehat{\mathbf{r}}_{12}(\omega)\right) \tag{D.29}$$

one finds, following the same steps, along with the use of Ref. [90]

$$\left\langle \left[\Phi^{220}\left(\omega_1, \omega_2, \omega\right)\right]^2 \right\rangle_{\omega_1,\omega_2} = \frac{4}{5} \tag{D.30}$$

$$g^{220}(r) = h^{220}(r) = \frac{5}{16\pi N \rho r^2} \left\langle \sum_{i<j} \delta\left(r - r_{ij}\right) \Phi^{220}\left(\omega_1, \omega_2, \omega\right) \right\rangle \tag{D.31}$$

Again, this coincides with eq.(9d) of Ref. [91].

These are also the coefficients computed in Refs. [82, 83] (albeit with different notations).

Bibliography

[1] Michi Nakata, Giuliano Zanchetta, Brandon D. Chapman, Christopher D. Jones, Julie O. Cross, Ronald Pindak, Tommaso Bellini, and Noel A. Clark. End-to-end stacking and liquid crystal condensation of 6– to 20–base pair dna duplexes. *Science*, 318(5854):1276–1279, 2007. doi: 10.1126/science.1143826. URL http://www.sciencemag.org/content/318/5854/1276.abstract.

[2] Cristiano De Michele, Tommaso Bellini, and Francesco Sciortino. Self assembly of bifunctional patchy particles with anisotropic shape into polymers chains: Theory, simulations, and experiments. *Macromolecules*, 45(2):1090–1106, 2012. doi: 10.1021/ma201962x. URL http://dx.doi.org/10.1021/ma201962x.

[3] Alexei A. Kornyshev, Dominic J. Lee, Sergey Leikin, and Aaron Wynveen. Structure and interactions of biological helices. *Rev. Mod. Phys.*, 79:943–996, Aug 2007. doi: 10.1103/RevModPhys.79.943. URL http://link.aps.org/doi/10.1103/RevModPhys.79.943.

[4] Alexei A. Kornyshev and Sergey Leikin. Helical structure determines different susceptibilities of dsdna, dsrna, and tsdna to counterion induced condensation. *Biophysical Journal*, 104(9):2031 – 2041, 2013. ISSN 0006-3495. doi: http://dx.doi.org/10.1016/j.bpj.2013.03.033. URL http://www.sciencedirect.com/science/article/pii/S000634951300372X.

[5] Edward Barry, Zach Hensel, Zvonimir Dogic, Michael Shribak, and Rudolf Oldenbourg. Entropy-driven formation of a chiral liquid-crystalline phase of helical filaments. *Phys. Rev. Lett.*, 96:018305, Jan 2006. doi: 10.1103/PhysRevLett.96.018305. URL http://link.aps.org/doi/10.1103/PhysRevLett.96.018305.

[6] P.G. de Gennes and J. Prost. *The Physics of Liquid Crystals*. Clarendon Press, Oxford, 1993.

[7] S. Chandrasekhar. *Liquid crystals*. Cambridge University Press, Newyork, 2nd edition, 1992.

[8] F. Reinitzer. *Chem.*, 9:421.

[9] K. Hiltrop. *Phase Chirality of micellar lyotropic liquid crystals*. Springer, Germany, 2001.

[10] Danqing Liu and Dirk J. Broer. Liquid crystal polymer networks: Preparation, properties, and applications of films with patterned molecular alignment. *Langmuir*, 30(45):13499–13509, 2014. doi: 10.1021/la500454d. URL http://dx.doi.org/10.1021/la500454d. PMID: 24707811.

[11] Alejandro D. Rey. Liquid crystal models of biological materials and processes. *Soft Matter*, 6:3402, 2010. doi: 10.1039/b921576j. URL http://pubs.rsc.org/en/content/articlehtml/2010/sm/b921576j.

[12] M.P. Allen and D.J. Tildesley. *Computer Simulation of Liquids*. Clarendon Press, Oxford, 1987.

[13] P. Tarazona, J.A. Cuesta, and Y. Martínez-Ratón. Density functional theories of hard particle systems. In Ángel Mulero, editor, *Theory and Simulation of Hard-Sphere Fluids and Related Systems*, volume 753 of *Lecture Notes in Physics*, pages 247–341. Springer Berlin Heidelberg, 2008. ISBN 978-3-540-78766-2. doi: 10.1007/978-3-540-78767-9_7. URL http://dx.doi.org/10.1007/978-3-540-78767-9_7.

[14] K. C. Chu and W. L. McMillan. Unified landau theory for the nematic, smectic a, and smectic c phases of liquid crystals. *Phys. Rev. A*, 15:1181–1187, Mar 1977. doi: 10.1103/PhysRevA.15.1181. URL http://link.aps.org/doi/10.1103/PhysRevA.15.1181.

[15] Satyendra Kumar. *Liquid crystals Experimental study of physical properties and phase transitions*. Cambridge University Press, Cambridge, 2001.

[16] D. Andrienko. *Introduction to Liquid Crystals*. Cambridge University Press, 2006. URL http://www2.mpip-mainz.mpg.de/~andrienk/teaching/IMPRS/liquid_crystals.pdf.

[17] A. Jakli and A. Saupe. *One and two dimensional fluids*. Taylor and Francis, Florida, 2006.

[18] R. BRUCE KING. Chirality and handedness. *Annals of the New York Academy of Sciences*, 988(1):158–170, 2003. ISSN 1749-6632. doi: 10.1111/j.1749-6632.2003.tb06095.x. URL http://dx.doi.org/10.1111/j.1749-6632.2003.tb06095.x.

[19] V. L. Lorman and B. Mettout. Theory of chiral periodic mesophases formed from an achiral liquid of bent core molecules. *Phys. Rev. E*, 69:061710, Jun 2004. doi: 10.1103/PhysRevE.69.061710. URL http://link.aps.org/doi/10.1103/PhysRevE.69.061710.

[20] S. M. Douglas, H. Dietz, T. Liedl B. Hogberg, F.Graf, and W. H. Shih. Self assembly of dna into nanoscale three dimensional shapes. *Nature*, 459:414, 2009. doi: 10.1038/nature08016. URL http://dx.doi.org/10.1038/nature08016.

[21] N.C. Seeman. Dna in a material world. *Nature*, 421:427–431, 2003. doi: 10.1038/nature01406. URL http://dx.doi.org/10.1038/nature01406.

[22] Tamaki Nakano and Yoshio Okamoto. Synthetic helical polymers: conformation and function. *Chemical reviews*, 101(12):4013–4038, 2001.

[23] Eiji Yashima, Katsuhiro Maeda, Hiroki Iida, Yoshio Furusho, and Kanji Nagai. Helical polymers: synthesis, structures, and functions. *Chemical reviews*, 109(11): 6102–6211, 2009.

[24] H. H. Strey, J. wang, J. Podgornik, A. Rupprecht, L. Yu, A. Parsegian, and E. B. Sirota. *Phys. Rev. Lett.*, 84:3105, 2000.

[25] Elisa Frezza, Alberta Ferrarini, Hima Bindu Kolli, Achille Giacometti, and Giorgio Cinacchi. Left or right cholesterics? a matter of helix handedness and curliness. *Phys. Chem. Chem. Phys.*, 16:16225–16232, 2014. doi: 10.1039/C4CP01816H. URL http://dx.doi.org/10.1039/C4CP01816H.

[26] S. Belli, S. Dussi, M. Dijkstra, and R. van Roij. Density functional theory for chiral nematic liquid crystals. *Phys. Rev. E*, 90:020503, Aug 2014. doi: 10.1103/PhysRevE.90.020503. URL http://link.aps.org/doi/10.1103/PhysRevE.90.020503.

[27] Strzelecka Teresa E, Davidson Michael W, and Rill RandolphL. Multiple liquid crystal phases of dna at high concentrations. *Nature*, 331. doi: 10.1038/331457a0. URL http://dx.doi.org/10.1038/331457a0.

[28] F. Livolant, A. M. Levelut, J. Doucet, and J. P. Benoit. The highly concentrated liquid crystalline phase of dna is columnar hexagonal. *Nature*, 339, 1989. doi: 10.1038/339724a0. URL http://dx.doi.org/10.1038/339724a0.

[29] Eric Grelet and Seth Fraden. What is the origin of chirality in the cholesteric phase of virus suspensions? *Phys. Rev. Lett.*, 90:198302, May 2003. doi: 10.1103/PhysRevLett.90.198302. URL http://link.aps.org/doi/10.1103/PhysRevLett.90.198302.

[30] Zvonimir Dogic and Seth Fraden. Ordered phases of filamentous viruses. *Current Opinion in Colloid andInterface Science*, 11(1):47 – 55, 2006. ISSN 1359-0294. doi: http://dx.doi.org/10.1016/j.cocis.2005.10.004. URL http://www.sciencedirect.com/science/article/pii/S1359029405000981.

[31] Jianxin Tang and Seth Fraden. Magnetic-field-induced isotropic-nematic phase transition in a colloidal suspension. *Phys. Rev. Lett.*, 71:3509–3512, Nov 1993. doi: 10.1103/PhysRevLett.71.3509. URL http://link.aps.org/doi/10.1103/PhysRevLett.71.3509.

[32] Zvonimir Dogic and Seth Fraden. Smectic phase in a colloidal suspension of semi-flexible virus particles. *Phys. Rev. Lett.*, 78:2417–2420, Mar 1997. doi: 10.1103/PhysRevLett.78.2417. URL http://link.aps.org/doi/10.1103/PhysRevLett.78.2417.

[33] Z. Dogic and S. Fraden. Phase behaviour of rod-like viruses and virus-spere mixtures. *Soft Matter*, 2(1), 2006. doi: DOI:10.1002/9783527617067.ch1.

[34] Peter Bolhuis and Daan Frenkel. Tracing the phase boundaries of hard spherocylinders. *The Journal of Chemical Physics*, 106(2):666–687, 1997. doi: http://dx.doi.org/10.1063/1.473404. URL http://scitation.aip.org/content/aip/journal/jcp/106/2/10.1063/1.473404.

[35] D. Frenkel and B. Smit. *Understanding Molecular Simulation: From Algorithms to Applications*. Academic Press, San Diego, 2002.

[36] K. P. N. Murthy. *Monte methods in statistical physics*. University Press, Hyderabad, 2004.

[37] L. E. Reichl. *A Modern Course in Statistical Physics*. University of Texas Press, 1980.

[38] H. Goldstein. *Classical Mechanics*. Addison-Welsey, 1980.

[39] D. Jayasri. *Monte Carlo studies of liquid crystalline system*. LAP Lambert Academic publishers, Germany, 2011.

[40] Nicholas Metropolis, Arianna W. Rosenbluth, Marshall N. Rosenbluth, Augusta H. Teller, and Edward Teller. Equation of state calculations by fast computing machines. *The Journal of Chemical Physics*, 21(6):1087–1092, 1953. doi: http://dx.doi.org/10.1063/1.1699114. URL http://scitation.aip.org/content/aip/journal/jcp/21/6/10.1063/1.1699114.

[41] W. W. Wood. Monte carlo calculations for hard disks in the isothermal isobaric ensemble. *The Journal of Chemical Physics*, 48(1):415–434, 1968. doi: http://dx.doi.org/10.1063/1.1667938. URL http://scitation.aip.org/content/aip/journal/jcp/48/1/10.1063/1.1667938.

[42] McDonald. Npt monte carlo calculations for binary liquid mixtures. *Mol. Phys.*, 423: 41–58, 1972. doi: 10.1080/00268977200100031. URL http://www.tandfonline.com/doi/abs/10.1080/00268977200100031#.VHh3luLrYb8.

[43] R. Eppinga and D. Frenkel. Monte carlo study of the isotropic and nematic phases of infinitely thin hard platelets. *Mol. Phys.*, 52:1303–1334, 1984. doi: 10.1080/00268978400101951. URL http://www.tandfonline.com/doi/abs/10.1080/00268978400101951.

[44] Charles F.F. Karney. Quaternions in molecular modeling. *Journal of Molecular Graphics and Modelling*, 25(5):595 – 604, 2007. ISSN 1093-3263. doi: http://dx.doi.org/10.1016/j.jmgm.2006.04.002. URL http://www.sciencedirect.com/science/article/pii/S1093326306000829.

[45] Franz J Vesely. Angular monte carlo integration using quaternion parameters: a spherical reference potential for ccl_4. *Journal of Computational Physics*, 47(2):291–296, 1982.

[46] William M. Gelbart and Boris Barboy. A van der waals picture of the isotropic-nematic liquid crystal phase transition. *Accounts of Chemical Research*, 13(8): 290–296, 1980. doi: 10.1021/ar50152a007. URL http://dx.doi.org/10.1021/ar50152a007.

[47] J. P. Hansen and I. R. Mc Donald. *Theory of Simple Liquids*. Academic Press, London, 1986.

[48] J. A. Barker and D. Henderson. What is "liquid"? understanding the states of matter. *Rev. Mod. Phys.*, 48:587–671, Oct 1976. doi: 10.1103/RevModPhys.48.587. URL http://link.aps.org/doi/10.1103/RevModPhys.48.587.

[49] P. N. Pusey and W. van Megen. Phase behaviour of concentrated suspensions of nearly hard colloidal spheres. *Nature*, 320:340–342, 1986. doi: 10.1038/320340a0. URL http://dx.doi.org/10.1038/320340a0.

[50] Lars Onsager. The effects of shape on the interaction of colloidal particles. *Annals of the New York Academy of Sciences*, 51(4):627–659, 1949. ISSN 1749-6632. doi: 10.1111/j.1749-6632.1949.tb27296.x. URL http://dx.doi.org/10.1111/j.1749-6632.1949.tb27296.x.

[51] H. Zocher. Über freiwillige strukturbildung in solen. (eine neue art anisotrop flüssiger medien.). *Zeitschrift für anorganische und allgemeine Chemie*, 147(1):91–110, 1925. ISSN 1521-3749. doi: 10.1002/zaac.19251470111. URL http://dx.doi.org/10.1002/zaac.19251470111.

[52] J. D. Bernal F. C. Bawden, N. W. Pirie and I. Fankuchen. Liquid crystalline substances from virus-infected plants. *Nature*, 138:1051, 1936. doi: 10.1038/1381051a0. URL http://www.nature.com/nature/journal/v138/n3503/abs/1381051a0.html.

[53] J. D. Parsons. Nematic ordering in a system of rods. *Phys. Rev. A*, 19:1225–1230, Mar 1979. doi: 10.1103/PhysRevA.19.1225. URL http://link.aps.org/doi/10.1103/PhysRevA.19.1225.

[54] Sin Doo Lee. A numerical investigation of nematic ordering based on a simple hard rod model. *The Journal of Chemical Physics*, 87(8):4972–4974, 1987. doi: http://dx.doi.org/10.1063/1.452811. URL http://scitation.aip.org/content/aip/journal/jcp/87/8/10.1063/1.452811.

[55] vide GJ Vroege and HNW Lekkerkerker. Phase transitions in lyotropic colloidal and polymer liquid crystals. *Reports on Progress in Physics*, 55(8):1241, 1992.

[56] Elisa Frezza, Alberta Ferrarini, Hima Bindu Kolli, Achille Giacometti, and Giorgio Cinacchi. The isotropic-to-nematic phase transition in hard helices: Theory and simulation. *The Journal of Chemical Physics*, 138(16):164906, 2013. doi: http://dx.doi.org/10.1063/1.4802005. URL http://scitation.aip.org/content/aip/journal/jcp/138/16/10.1063/1.4802005.

[57] W Maier and A Saupe. Eine einfache molekulare theorie des nematischen kristallinflussigen zustandes. *Zeitshrift fur Naturforschung*, 13a:564–566, 1958.

[58] Carlos Vega and Santiago Lago. A fast algorithm to evaluate the shortest distance between rods. *Computers and Chemistry*, 18(1):55 – 59, 1994. ISSN 0097-8485. doi: http://dx.doi.org/10.1016/0097-8485(94)80023-5. URL http://www.sciencedirect.com/science/article/pii/0097848594800235.

[59] H. Flyvbjerg and H. G. Petersen. Error estimates on averages of correlated data. *The Journal of Chemical Physics*, 91(1), 1989.

[60] SZABOLCS VARGA and ISTVÁN SZALAI. Modified parsons-lee theory for fluids of linear fused hard sphere chains. *Molecular Physics*, 98(10):693–698, 2000. doi: 10.1080/00268970009483337. URL http://dx.doi.org/10.1080/00268970009483337.

[61] S.C. Glotzer and M.J. Solomon. Anisotropy of buiding blocks and their assembly into complex structures. *Nature Mat.*, 6:557–562, 2007. doi: 10.1038/nmat1949. URL http://dx.doi.org/10.1038/nmat1949.

[62] Joost de Graaf, Laura Filion, Matthieu Marechal, René van Roij, and Marjolein Dijkstra. Crystal-structure prediction via the floppy-box monte carlo algorithm: Method and application to hard (non)convex particles. *The Journal of Chemical Physics*, 137(21):214101, 2012. doi: http://dx.doi.org/10.1063/1.4767529. URL http://scitation.aip.org/content/aip/journal/jcp/137/21/10.1063/1.4767529.

[63] M. Dijkstra. Phase diagrams of shape-anisotropic colloidal particles. *Proceedings of the International School of Physics "Enrico Fermi"*. doi: 10.3254/978-1-61499-278-3-229.

[64] S. Sacanna, M. Korpics, K. Rodriguez, L. Colon Melendez, S. H. Kim, D. J. Pine, and G. R. Yi. Shaping colloids for self-assembly. *Nature Comm.*, 4:1–5, 2013. doi: 10.1038/ncomms2694. URL http://dx.doi.org/10.1038/ncomms2694.

[65] Gerardo Odriozola. Revisiting the phase diagram of hard ellipsoids. *J. Chem. Phys.*, 136, 2012.

[66] Yves Lansac, Prabal K. Maiti, Noel A. Clark, and Matthew A. Glaser. Phase behavior of bent-core molecules. *Phys. Rev. E*, 67:011703, Jan 2003. doi: 10.1103/PhysRevE.67.011703. URL http://link.aps.org/doi/10.1103/PhysRevE.67.011703.

[67] T. S. Hudson and Peter Harrowell. Dense packings of hard spheres of different sizes based on filling interstices in uniform three-dimensional tilings. *The Journal of Physical Chemistry B*, 112(27):8139–8143, 2008. doi: 10.1021/jp802912a. URL http://dx.doi.org/10.1021/jp802912a. PMID: 18553902.

[68] Toby S Hudson and Peter Harrowell. Structural searches using isopointal sets as generators: densest packings for binary hard sphere mixtures. *Journal of Physics: Condensed Matter*, 23(19):194103, 2011. URL http://stacks.iop.org/0953-8984/23/i=19/a=194103.

[69] Frank H. Allen. The Cambridge Structural Database: a quarter of a million crystal structures and rising. *Acta Crystallographica Section B*, 58(3 Part 1):380–388, Jun 2002. doi: 10.1107/S0108768102003890. URL http://dx.doi.org/10.1107/S0108768102003890.

[70] S. M. Woodley and R. Catlow. Crystal structure prediction from first principles. *Nature Materials*, 7:937, 2008.

[71] Hima Bindu Kolli, Elisa Frezza, Giorgio Cinacchi, Alberta Ferrarini, Achille Giacometti, and Toby S. Hudson. Communication: From rods to helices: Evidence

of a screw-like nematic phase. *The Journal of Chemical Physics*, 140(8):081101, 2014. doi: http://dx.doi.org/10.1063/1.4866808. URL http://scitation.aip.org/content/aip/journal/jcp/140/8/10.1063/1.4866808.

[72] Hima Bindu Kolli, Elisa Frezza, Giorgio Cinacchi, Alberta Ferrarini, Achille Giacometti, Toby S. Hudson, Cristiano De Michele, and Francesco Sciortino. Self-assembly of hard helices: a rich and unconventional polymorphism. *Soft Matter*, 10: 8171–8187, 2014. doi: 10.1039/C4SM01305K. URL http://dx.doi.org/10.1039/C4SM01305K.

[73] F. Manna, V. Lorman, R. Podgornik, and B. Žekš. Screwlike order, macroscopic chirality, and elastic distortions in high-density dna mesophases. *Phys. Rev. E*, 75: 030901, Mar 2007. doi: 10.1103/PhysRevE.75.030901. URL http://link.aps.org/doi/10.1103/PhysRevE.75.030901.

[74] E.B. Priestley, P.J. Woitowiczs, and P. Sheng. *Introduction to Liquid Crystals*. Plenum Press, New York, 1974.

[75] U. Kreibig and C. Z. Wetter. Light diffraction of in vitro crystals of six tobacco mosaic viruses. *Naturforsch.*, 35C:750–762, 1980.

[76] Fraden, S., Hurd, A. J., Meyer, R. B., Cahoon, M., and Caspar, D. L.D. Magnetic-field-induced alignment and instabilities in ordered colloids of tobacco mosaic virus. *J. Phys. Colloques*, 46:C3–85–C3–113, 1985. doi: 10.1051/jphyscol:1985309. URL http://dx.doi.org/10.1051/jphyscol:1985309.

[77] Yoshiko Maeda and Sei Hachisu. Schiller layers in beta-ferric oxyhydroxide sol as an order—disorder phase separating system. *Colloids and Surfaces*, 6(1):1 – 16, 1983. ISSN 0166-6622. doi: http://dx.doi.org/10.1016/0166-6622(83)80001-8. URL http://www.sciencedirect.com/science/article/pii/0166662283800018.

[78] D. Frenkel, H. N. W. Lekkerkerker, and A. Stroobants. Thermodynamic stability of a smectic phase in a system of hard rods. *Nature*, 332:822–823, 1988. doi: 10.1038/332822a0. URL http://dx.doi.org/10.1038/332822a0.

[79] James M. Polson and Daan Frenkel. First-order nematic-smectic phase transition for hard spherocylinders in the limit of infinite aspect ratio. *Phys. Rev. E*, 56:R6260–R6263, Dec 1997. doi: 10.1103/PhysRevE.56.R6260. URL http://link.aps.org/doi/10.1103/PhysRevE.56.R6260.

[80] Hisanari Onouchi, Kento Okoshi, Takashi Kajitani, Shin-ichiro Sakurai, Kanji Nagai, Jiro Kumaki, Kiyotaka Onitsuka, and Eiji Yashima. Two- and three-dimensional smectic ordering of single-handed helical polymers. *Journal of the*

American Chemical Society, 130(1):229–236, 2008. doi: 10.1021/ja074627u. URL http://dx.doi.org/10.1021/ja074627u. PMID: 18076167.

[81] G. R. Luckhurst and G. Saielli. Computer simulation studies of anisotropic systems. xxxii. field-induction of a smectic a phase in a gay–berne mesogen. *The Journal of Chemical Physics*, 112(9):4342–4350, 2000. doi: http://dx.doi.org/10.1063/1.480981. URL http://scitation.aip.org/content/aip/journal/jcp/112/9/10.1063/1.480981.

[82] M. A. Bates and G. R. Luckhurst. Computer simulation studies of anisotropic systems. xxx. the phase behavior and structure of a gay–berne mesogen. *The Journal of Chemical Physics*, 110(14):7087–7108, 1999. doi: http://dx.doi.org/10.1063/1.478563. URL http://scitation.aip.org/content/aip/journal/jcp/110/14/10.1063/1.478563.

[83] R. Memmer. Liquid crystal phases of achiral banana-shaped molecules: a computer simulation study. *Liquid Crystals*, 29(4):483–496, 2002. doi: 10.1080/02678290110104586. URL http://dx.doi.org/10.1080/02678290110104586.

[84] Mario Cifelli, Giorgio Cinacchi, and Luca De Gaetani. Smectic order parameters from diffusion data. *The Journal of Chemical Physics*, 125(16):164912, 2006. doi: http://dx.doi.org/10.1063/1.2359428. URL http://scitation.aip.org/content/aip/journal/jcp/125/16/10.1063/1.2359428.

[85] Giorgio Cinacchi and Luca De Gaetani. Phase behavior of wormlike rods. *Phys. Rev. E*, 77:051705, May 2008. doi: 10.1103/PhysRevE.77.051705. URL http://link.aps.org/doi/10.1103/PhysRevE.77.051705.

[86] Paul J. Steinhardt, David R. Nelson, and Marco Ronchetti. Bond-orientational order in liquids and glasses. *Phys. Rev. B*, 28:784–805, Jul 1983. doi: 10.1103/PhysRevB.28.784. URL http://link.aps.org/doi/10.1103/PhysRevB.28.784.

[87] Giorgio Cinacchi and Alessandro Tani. Computer simulations of pure and mixed systems of disklike particles interacting with the s-function corner potential. *The Journal of Chemical Physics*, 117(24):11388–11395, 2002. doi: http://dx.doi.org/10.1063/1.1522372. URL http://scitation.aip.org/content/aip/journal/jcp/117/24/10.1063/1.1522372.

[88] Eric Grelet. Hard rod behavior in dense mesophases of semiflexible and rigid charged viruses. *Phys. Rev. X*, 4:021053, Jun 2014. doi: 10.1103/PhysRevX.4.021053. URL http://link.aps.org/doi/10.1103/PhysRevX.4.021053.

[89] C. G. Gray and K. E. Gubbins. *Theory of Molecular Fluids Fundamentals*. Oxford University Press, Newyork, 1984.

[90] G. Stell, G. N. Patey, and J. S. Høye. *Dielectric Constants of Fluid Models: Statistical Mechanical Theory and its Quantitative Implementation*, pages 183–328. John Wiley and Sons, Inc., 2007. ISBN 9780470142684. doi: 10.1002/9780470142684.ch3. URL http://dx.doi.org/10.1002/9780470142684.ch3.

[91] J. J. Weis and D. Levesque. Ferroelectric phases of dipolar hard spheres. *Phys. Rev. E*, 48:3728–3740, Nov 1993. doi: 10.1103/PhysRevE.48.3728. URL http://link.aps.org/doi/10.1103/PhysRevE.48.3728.